Title
Characterizing Near Nadir Ka-band Backscatter for Mapping Water Surfaces With InSAR

Author
Fayne, Jessica Victoria

Publication Date
2022

Peer reviewed|Thesis/dissertation

UNIVERSITY OF CALIFORNIA

Los Angeles

Characterizing Near Nadir Ka-band Backscatter for Mapping Water Surfaces With InSAR

A dissertation submitted in partial satisfaction of the requirements for the degree of Doctor of Philosophy in Geography

by

Jessica Victoria Fayne

2022

ABSTRACT OF THE DISSERTATION

Characterizing Near Nadir Ka-band Backscatter

for Mapping Water Surfaces With InSAR

by

Jessica Victoria Fayne

Doctor of Philosophy in Geography

University of California, Los Angeles, 2022

Professor Laurence C. Smith, Co-Chair

Professor Dennis P. Lettenmaier, Co-Chair

To gain an empirical understanding of the utility of near-nadir Ka-band for mapping surface changes, particularly with respect to water and wet surfaces, this dissertation demonstrates the utility for mapping water surface elevation (WSE) and inundation as observed by the airborne complement of the upcoming Surface Water and Ocean Topography (SWOT), AirSWOT. To produce high-resolution WSE and extents, SWOT and AirSWOT rely on strong backscatter signal returns using the Ka-band radar frequency. However, despite having many theoretical assessments of Ka-band scattering for water surfaces, observation-based knowledge of high-resolution Ka-band

scattering for small inland water bodies is limited, consequently limiting the understanding of signal errors and resultant elevation errors.

AirSWOT has provided the first Ka-band InSAR observations over diverse land cover and under changing hydrologic conditions by flying through Alaska and Canada during July and August 2017, allowing an unprecedented assessment of Ka-band scattering dynamics. These flights revealed bright radar returns, akin to a theoretical open water return, over vegetation and moist, bare soils, complicating open water classification, a necessary task for the SWOT mission. AirSWOT WSE errors relative to in-situ GPS showed an average bias of -58 cm. After correcting for biases, centimeter-level seasonal hydrologic changes are identified across the study region for the period July-August 2017. Following bias correction, residual errors may be explained by the prevalence of mixed water-vegetation pixels, which may occur in 5% of observations on average, and by wind speeds below 3 m/s (6.7 mph), which reduce water surface roughness.

This dissertation uses airborne AirSWOT, LiDAR, model, and in-situ data to (1) demonstrate the utility of the 2017 Ka-band AirSWOT observations, showing that the error-prone dataset can nonetheless observe cm-scale hydrologic spatial and temporal gradients across the ABoVE domain; (2) identify differences and similarities in backscattering values between water and land cover types to assess the likelihood of misclassification, additionally enabling the characterization of vegetation densities alongside the heights estimated from InSAR; and (3) assess atmospheric influences from the wind on Ka-band scattering changes due to water surface roughening, creating a path for assessments at the water-air interface for small water bodies.

The dissertation of Jessica Victoria Fayne is approved.

Yongwei Sheng

Steven A. Margulis

Curtis Chen

Laurence C. Smith, Committee Co-Chair

Dennis P. Lettenmaier, Committee Co-Chair

University of California, Los Angeles

2022

This dissertation is dedicated to my family and friends,

and the ancestors and descendants of my family and friends.

This dissertation is dedicated to those who gave me opportunities,

and to those who taught me how to live through struggle.

Table of Contents

Acknowledgments

I am extremely grateful for the support and guidance of my advisor and dissertation chair, Laurence Smith, without whom, I would not have been able to work on SWOT research. I am additionally grateful for my committee members, Dennis Lettenmaier (co-chair), Curtis Chen, Yongwei Sheng, and Steven Margulis. All with vastly different areas of expertise, my committee believed in me, held me to high standards, and asked thought-provoking questions, bringing me great comfort in the foundation that I have established during my Ph.D. program.

I would like to acknowledge the faculty and staff at the UCLA Department of Geography who have helped guide and support my progress. I am grateful for the efforts of Kasi McMurray, Jenne Misraje, Nayla Huq, Brian Won, and Matt Zebrowski, without whom, the department would not be the same. I am also thankful to NASA, an organization that formed the foundation of my research career through funding and collaborative research opportunities. Researchers at NASA Jet Propulsion Laboratory were instrumental in my education in radar science and hydrology, and I am thankful to my official and unofficial advisors who supported me during my research at JPL.

While not involved in my research during my Ph.D. I also want to thank my pre-Ph.D. advisor, Venkat Lakshmi, who has always believed in me.

I would like to thank all of my colleagues and friends at UCLA, JPL, and Brown University who encouraged me and gave me advice. I am happy to have been a part of so many lab groups and have been supported by so many people with diverse perspectives. From Prof. Smith's group, the Northern Change Research Lab, Lincoln Pitcher, and Matthew Cooper worked with me at UCLA; Johnny Ryan, Sarah Cooley, Ethan Kyzivat, Katia Lezine, Chang Huang, Sarah Esenther, Bo Wang, Nimisha Wagle, and Sebastian Munoz worked from Brown University. During a difficult period of transition in the lab from UCLA to Brown University beginning in my first year,

my lab mates worked hard to support one another and provide guidance and encouragement. I am proud of the undergraduate student in our lab, Carolyn Lober, who inspired me to keep my R code neat, use ggplot, and stay organized.

My lab groups at JPL were incredible as well. Arriving as a JPL Visiting Student Researcher, weeks after moving to California and starting a graduate program, I was warmly welcomed by Curtis Chen, Albert Chen, Xiaoqing Wu, Michael Denbina, and Brent Williams as a member of the AirSWOT Processing Working Group. The members of the AirSWOT group taught me radar fundamentals, loaned textbooks, and provided me with any information I could think to ask for. With the support and encouragement of Cedric David, I also joined the JPL Terrestrial Hydrology (Water and Ecosystems) Group. Marc Simard welcomed me into his global remote sensing group at JPL. As a junior researcher in all three JPL groups, I was inspired to learn and encouraged to participate, giving me the freedom and flexibility to be creative while improving my ability to conduct scientific research.

There are too many students in UCLA Geography and Civil Engineering departments who kept me sane and brought me joy during good and bad times, to list. An incomplete list includes Sarfaraz Alam, Zhaoxin Ban, Kate Cavanaugh, Monica Dimson, Cheryl Doughty, Elizabeth Fard, Michael Fischella, Jessie George, Kayden Haleakala, Ji Woo Han, Huilin Huang, Daniel Jensen, Yufei Liu, Jacob Schaperow, Lu Su, Emilie Tarouilly, Shreya Trivedi, Solomon Vimal, and many others who made my time at UCLA memorable and enjoyable.

Without the support of my family, I could not have achieved any of this work. I thank my husband Jan A. Kumor, as well as my parents, my brother, and my sister for their love, support, and encouragement.

The AirSWOT instrument and flight campaigns were funded through NASA grants, and 2017 ABoVE AirSWOT data mentioned in this study were processed and produced by researchers at NASA Jet Propulsion Laboratory. A portion of this dissertation was performed at the Jet Propulsion Laboratory, California Institute of Technology, under contract with NASA. I received direct funding to carry out my Ph.D. research from 1) UCLA Cota-Robles Fellowship, designed to cover my 1st and 4th year; 2) NASA Future Investigators in Earth and Space Science and Technology (FINESST) Grant 80NSSC19K137, covering years 3-5; and 3) supplemental funding through UCLA Department of Geography grants and teaching assistantships.

This work was additionally funded by NASA Terrestrial Hydrology (SWOT Science Team) Grant NNX16AH83G, and NASA Terrestrial Ecology (ABoVE) Grant NNX17AC60A.

Chapter 2 is a version of [J. V. Fayne, Smith L.C., Pitcher L.H, Kyzivat E.K., Cooley S.W., Cooper M.G., Denbina M., Chen A.C., Chen C.W., Pavelsky T.M. "Airborne observations of Arctic-Boreal water surface elevations from AirSWOT Ka-Band InSAR and LVIS LiDAR," Environ. Res. Lett., vol. 15, no. 10, p. 105005, Oct. 2020, doi: 10.1088/1748-9326/abadcc. *Published*]

Chapter 3 is a version of [J. V. Fayne, Smith L.C., Liao T-H., Pitcher L.H, Denbina M., Chen A.C., Simard M., Chen C.W., Williams B.A. "Characterizing Near-Nadir Ka-Band SAR Backscatter from Wet Surfaces and Diverse Land Covers," Mar. 2022, doi: 10.36227/techrxiv.19380098.v1. *Preprint*]

Chapter 4 is a version of [J.V. Fayne, Smith L.C., “How does wind influence near-nadir Ka-Band radar backscatter and interferometric coherence returns from small inland water bodies?” June 2022.]

Biographical Sketch

Jessica was born and raised in Centreville, Virginia, a suburb of Washington D.C. Despite early difficulties in the classroom, Jessica learned that she excelled at learning on her own, truly beginning to understand and appreciate her passion for independent research while juggling courses in architecture and political science at Hampton University.

After studying post-soviet democratization at Hampton University (B.S., Political Science) and American University (Cross-Cultural-Communications, International Relations, Masters Certification), Jessica remembered her love for maps and realized that there was a shortage of maps and spatial information available in her field of research. Upon enrolling at George Mason University for Geographic and Cartographic Sciences (M.S.), Jessica got involved in regional and national mapping organizations such as ASPRS, URISA, and USGIF, and subsequently fell in love with Remote Sensing.

Remote Sensing offers the unique and quantitative ability to understand space, environments, and changing conditions, and her passion has always been understanding people and their environments.

At the end of her first year at George Mason University, she began an internship at NASA Goddard Space Flight Center, researching floods in Southeast Asia. This internship turned into a series of remote sensing-hydrology internships and consulting positions. Upon graduating, Jessica began a Research Associate Position at the University of South Carolina, where she worked for two years to produce high-resolution maps of available water resources while supporting multiple external research projects.

Finally, Jessica was ready to begin her Ph.D. program, starting a new adventure in California at UCLA.

Chapter 1

1. Introduction

1.1 Overview

Knowledge of surface water level and inundation extent is critically important to understanding regional water cycle dynamism and water resources. The forthcoming Surface Water and Ocean Topography (SWOT) mission will be the first satellite mission to make simultaneous observations of water level and extent for small and moderate-sized $(250m)^2$ + water bodies. Prior to this mission, a suite of diverse remote sensing instruments acquired global inundation extents separately from elevations. Inundation extents could be observed using active and passive sensors, while water levels could be assessed using active sensors. The differences between these instruments often resulted in spatial and temporal mismatches between observations, and many small water bodies could only be observed with high-resolution optical sensors, without the possibility of a water surface elevation measurement.

While studies have shown that inundation extents can be identified using high resolution (0.5-15 m) optical imagery [Davranche et al., 2013; Cooley et al., 2017; Kyzivat et al., 2019], these data suffer from cloud cover, reducing the frequency of observations. With the increased availability of cloud-penetrating SAR satellite data beginning in the late 1990s, many studies have demonstrated the efficacy of observing inundation extents, primarily with C- and L-band SAR instruments, with average look angles of 50 degrees, and 10-30 m spatial resolution [Hess et al., 1995; Kasischke et al., 1997; Alsdorf et al., 2007; Cretaux et al., 2011; Amani et al., 2019; Liao et

al., 2020]. While the C- and L-band instruments are capable of producing interferometric synthetic aperture radar (InSAR) elevation data for land, the time between observations and the viewing geometry of these land imaging SARs prevent adequate InSAR retrievals of water surface elevations. Radar altimetry instruments have the opposite issue, as altimeters provide coarsely spaced (AltiKa: 12 km; JASON 25 km) point measurements along the 1-dimensional orbital path, with no 2-dimensional mapping capabilities.

SWOT is the first space-borne instrument designed to produce 3-dimensional measurements of surface elevations and inundation extents and is also the first operational Ka-band SAR imaging satellite. Although SWOT has been designed to make these 3-D measurements, sensitivities of the spatial resolution and high-frequency SAR instrument to diverse inland surface covers and dynamic hydrologic and meteorologic conditions are not well understood.

1.2 Motivation

The uniqueness of SWOT comes from the onboard Ka-band SAR interferometer, an active remote sensing instrument designed to measure elevations with a very small spatial resolution compared with traditional altimeters (~10-70 m versus ~10-25 km) and with small vertical errors (±1.7 cm/km river slope (river reaches greater than 10 km); water surface elevation errors are limited to 10 cm (lake areas greater than 1 km^2), 25 cm (lake areas 0.0625-1 km^2) [Altenau et al., 2017; Desai et al., 2018; Pitcher et al., 2018; Fayne et al., 2020]. In support of the calibration and validation efforts for SWOT, an airborne SWOT-like instrument (AirSWOT) was developed. Despite having different viewing geometries, antenna configurations, and processing parameters, the Ka-band sensor on AirSWOT, the Ka-band SWOT Phenomenology Airborne Radar

(KaSPAR) provides measurements that are designed to be similar to SWOT. With development beginning in 2010 and with the first engineering flights in 2013 [Moeller et al., 2010; Wu et al., 2011, Martin 2013], AirSWOT KaSPAR is an experimental sensor that continues to undergo upgrades and improvements into 2022. Early studies of AirSWOT data identified Ka-band backscattering sensitivities to damp soils [Baney et al., 2014], and water surface elevation errors greater than 1 m [Altenau et al., 2019; Tuozzolo et al., 2019; Pitcher et al., 2019;]. These studies focused on localized and diverse regions, making it difficult to identify the prevalence of these issues. In addition, improvements to the AirSWOT data processing for 2017 reduced the magnitude of elevation errors originally identified in earlier studies, making the data ideally more comparable with in-situ measurements and SWOT, but also reducing the comparability with earlier AirSWOT data acquisition.

To identify to what extent AirSWOT can be used as an effective calibration and validation instrument for SWOT, and to have a better understanding of Ka-band scattering sensitivities, it is important to examine a variety of AirSWOT observations and derived products. This proposal is motivated by the necessity for an enhanced understanding of Ka-band radar in support of the forthcoming Surface Water Ocean Topography (SWOT) mission afforded by the novel observations of Arctic and Boreal river-lake-wetlands from the 2017 AirSWOT ABoVE flights.

1.3 Approach

In 2017, AirSWOT acquired the largest known collection of Ka-band SAR data to date. In support of the Arctic Boreal Vulnerability Experiment (ABoVE) Airborne Campaign (AAC), AirSWOT flew the KaSPAR instrument through central Canada to Alaska and back, with specific

focus areas in the Yukon Flats, Alaska, and the Peace Athabasca Delta, Canada. The total collection of the amassed data spans 23 degrees latitude and an area of over 22,000 km^2. This dissertation assesses the 2017 Ka-band AirSWOT KaSPAR data to achieve three goals: 1) demonstrate the accuracy and utility of the derived elevation data for hydrological analysis, 2) identify Ka-band radar scattering sensitivities for 15 diverse land covers and moisture regimes, including open water dry land, and wet vegetation (limited to 3-27 degrees of incidence), and 3) categorize the impacts of regional wind speeds on Ka-band scattering (limited to 3-17 degrees of incidence).

1.4 Summary of Examinations

The contents of this dissertation encompass three journal articles: one published [Chapter 2- Fayne et al., 2020], two under review [Chapter 3- Fayne et al., in review], [Chapter 4- Fayne et al., in review].

The first journal article, presented in chapter 2, examines the quality of the 2017 ABoVE AirSWOT InSAR data by 1) assessing the frequency of available data over observed water bodies, 2) validating the retrieved and spatial-averaged water surface elevations from AirSWOT with in-situ GPS water levels, 3) comparing spatially-averaged and point-based observations of AirSWOT with LiDAR data from the Land Vegetation and Ice Sensor (LVIS), and finally 4) demonstrating how AirSWOT InSAR elevations can be used to assess broad-scale hydrologic variability when compared with pressure transducers situated throughout the Canada-Alaska flight paths.

The second paper, now in review and presented in chapter 3, identifies Ka-band scattering sensitivities with a specific focus on 15 land cover types. The primary motivation for this study

came from a lack of off-the-shelf Ka-band scattering models spanning a wide range of incidence angles (0-30 degrees), with locally varying sensitivities to changing land cover and moisture. The project first assessed dielectric contributions to Ka-band scattering by comparing the KaSPAR scattering coefficients with moisture and temperature. Next, the influence of vegetation structure on scattering was assessed by using high-resolution LiDAR data that was acquired within days of the AirSWOT flight.

The third and final chapter will is found in chapter 4. Following a study of vegetation and land contributions to Ka-band scattering and examining the scattering diversity of land surfaces, it was appropriate to consider the diversity of within-water scattering. This project was additionally motivated by the notion that water surface scattering varies under certain meteorological conditions, and those conditions have the potential to reduce the quality of retrieved water surface elevations and inundation extents. Specifically, AirSWOT was treated like a simplified scatterometer to identify the influence of wind speeds on the backscatter coefficient as an indicator of signal strength and total coherence as an indicator of InSAR elevation quality.

1.5 Outline

This dissertation is defined by a focus on understanding Ka-band scattering to suggest improvements to future Ka-band airborne and satellite sensors and to understand possible sources of error in retrieved elevation products on the upcoming SWOT mission. Increased understanding of Ka-band scattering and the impacts on the derived elevation is not only important to the SWOT mission, but also to provide avenues for study using Ka-band radar and InSAR data for purposes

outside the goals of AirSWOT and SWOT, such as for the study of wetlands, infiltration, vegetation structure, wind speed, and evaporation.

Chapter 2 presents the problem of low-accuracy elevation retrievals, while Chapters 3 and 4 examine possible sources of error in the form of calculating the prevalence of water misclassification (Chapter 3), and demonstrating how low wind speeds lead to low Ka-band backscatter and low total coherence, reducing the quality of derived elevation measurements.

Chapter 2

2. AirSWOT Water Surface Elevation Accuracy

Title: Airborne Observations of Arctic Boreal Water Surface Elevations from Ka-band InSAR and LVIS LiDAR

2. 1 Introduction

Arctic-Boreal regions contain the largest number of freshwater bodies in the world [Lehner and Doll 2004; Carroll et al., 2011; Pekel et al., 2016], most of which are inaccessible and poorly studied. Yet the future vulnerability of these freshwater systems to high-latitude warming remains unknown [Walvoord and Kurylyk 2016; Bring et al., 2016]. To enhance scientific understanding of broad-scale physical, ecological, and social changes in the Arctic, the NASA Arctic Boreal Vulnerability Experiment (ABoVE) deployed 10 airborne assets in 2017 to survey over 4 million km^2 of Alaska and western Canada spanning diverse climatic, topographic and hydrological regimes coordinated with near-coincident ground-based measurements [Miller et al., 2019]. These assets provide important scientific datasets that are essential for Arctic-Boreal surface water studies [Kyzivat et al., 2019; Pitcher et al., 2020]. To that end, this work integrates three ABoVE airborne instruments to map water surface elevations (WSEs) of Arctic-Boreal surface water bodies, with a particular emphasis on an airborne Ka-band interferometric synthetic aperture radar (InSAR) developed by Remote Sensing Solutions (RSS) and the NASA Jet Propulsion Laboratory

(JPL), named the Ka-band SWOT Phenomenology Airborne Radar (KaSPAR) [Moller et al., 2010; Wu et al., 2011] carried on the AirSWOT aircraft.

AirSWOT KaSPAR produces swath-based digital elevation models (DEMs) covering both land and water. These data are optimized for WSE assessment, and KaSPAR was engineered as a validation instrument for the forthcoming Surface Water and Ocean Topography (SWOT) satellite mission planned for launch in 2022 [Fu et al., 2012; Chen et al., 2018]. SWOT will be the first satellite mission to map high-resolution WSEs for inland water bodies as well as oceans, using Ka-band (35.7 GHz) InSAR. SWOT will enhance scientific understanding of surface water, river discharge fluxes and lake volume changes by mapping WSE globally for rivers as narrow as 100 m, and lakes as small as $(250m)^2$ (0.0625 km^2). Requirements for the mean absolute errors on SWOT are 10 cm when spatially averaged across water bodies having areas larger than 1 km^2, and 25 cm for $(250m)^2$ areas [Desai et al., 2018]. However, investigations and quality assessment of Ka-band InSAR WSE retrievals over real-world water bodies are needed before the launch of SWOT, especially over lakes that have received little previous study. The 2017 ABoVE AirSWOT flight campaigns thus provide a rich observational dataset for this purpose as well as advancing scientific understanding of Arctic-Boreal surface water across the ABoVE domain.

As flown for ABoVE in 2017, the AirSWOT instrument suite included the KaSPAR interferometer (InSAR), and a color infrared digital camera system (CIR) [Moller et al., 2010; Moller et al., 2011; JPL-AirSWOT Group 2019]. During mostly-clear-sky days in July and August, the AirSWOT radar acquired 128 flight transects averaging ~45 km long and 3.9 km wide, collecting a total mapped area of 22,775 km^2 from North Dakota to Alaska spanning 23 degrees of latitude [Fayne et al., 2019]. The CIR system imaged a 4 km wide swath simultaneously, producing a total imaged area of 23,380 km^2 over the two months [Kyzivat et al., 2019]. The

AirSWOT platform flew northbound from North Dakota to Alaska in July, then returned southbound over the same flight transects in August, thus acquiring a large, multi-temporal data collection [Miller et al., 2019; Moller et al., 2010].

For the remainder of this study, we will refer to the AirSWOT Ka-band KaSPAR interferometer data as 'radar data', the derived DEM as 'elevation' or 'WSE' if the water has been extracted.

Here we present a first assessment of the performance and utility of the 2017 AirSWOT radar data acquired for ABoVE. Our objectives are to assess the quality of AirSWOT WSE observations across a broad spatial domain and to determine if their quality is sufficient for ABoVE hydrologic science and SWOT validation goals. Specifically in this application, we focus on Arctic storage changes at seasonal time scales. Broadly, we answer two questions: *1) How well did the AirSWOT radar data map water surface elevations across the ABoVE domain? 2) Can AirSWOT WSEs measure surface water storage change at seasonal time scales?* To answer these questions, we compared AirSWOT WSE with coincident *in situ* elevation data collected by field-based GPS surveys [Pitcher et al., 2020], and overlapping flight acquisitions of the NASA Land Vegetation and Ice Sensor (LVIS) airborne LiDAR instrument [Blair et al., 1999] which flew many of the same flight lines for ABoVE in 2017.

We discuss the completeness of the AirSWOT elevation data for mapping water bodies, as well as the utility of AirSWOT WSEs for measuring absolute elevations and changes in water storage through a comparison with LVIS airborne WSEs, and *in situ* GPS and pressure transducers and conclude with a discussion of best practices for handling the dataset and potential lessons for future deployments.

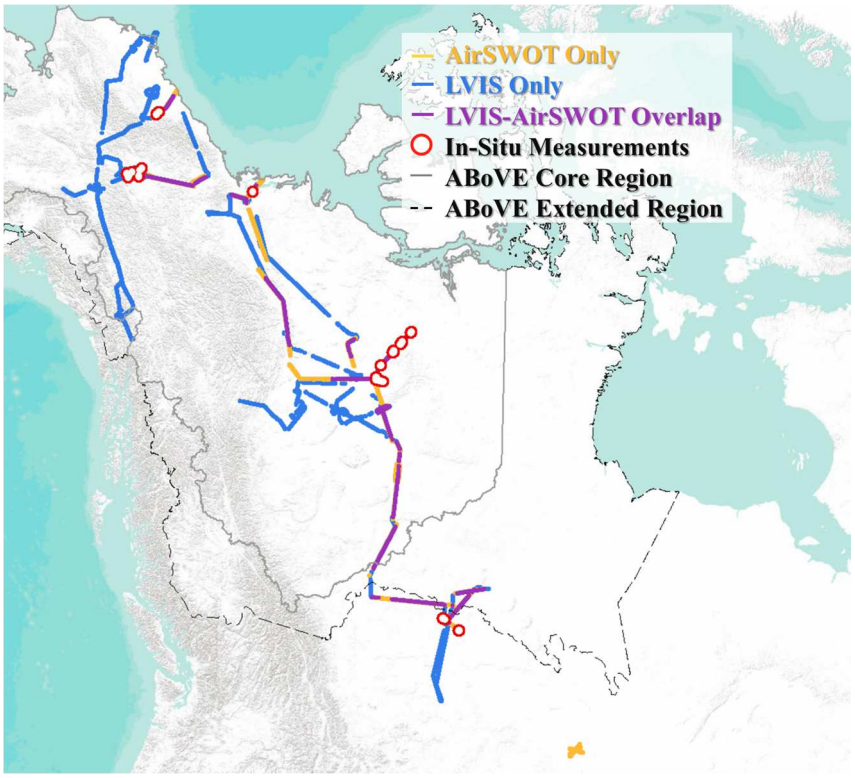

Figure 1. *Spatial coverage of the 2017 NASA Arctic-Boreal Vulnerability Experiment (ABoVE) AirSWOT radar and LVIS LiDAR airborne flight campaigns. AirSWOT flight tracks are shown in orange, LVIS LiDAR tracks in blue. Purple tracks represent overlapping coverage. Red circles denote locations of in-situ field GPS and coincident pressure transducer measurements of water surface elevation used for independent validation of both AirSWOT and LVIS WSE estimates.*

2.2 Data

2.2.1 AirSWOT Airborne Ka-band InSAR and Camera Data

The AirSWOT data presented here are the radar's 'outer swath' product, having an incidence angle range of 4-27° [Moller et al., 2010]. The 'inner swath' configuration (having incidence angles 1-5°, like SWOT) remains under development at NASA-JPL. AirSWOT radar data collected during the ABoVE 2017 flight campaign consist of elevation ("height" in meters relative to WGS84 ellipsoid), backscatter ("magnitude" in linear units), incidence angle (in radians), coherence (normalized correlation), sensitivity factor of estimated elevation to InSAR

phase ("Δh/Δphi" in meters/radian), and elevation uncertainty (1-sigma "error" in meters) over land and water surfaces [Fayne et al., 2019, https://doi.org/10.3334/ORNLDAAC/1646]. NASA-JPL developed software to produce these six radar products from raw radar data. Automated and manual quality assurance methods were used to identify regions with significant discrepancies (tens of meters) in elevation compared to a geoid-removed MERIT reference DEM [Yamazaki et al., 2017], and these regions are re-processed as needed to improve elevation accuracy (explained in the following sub-section). We reprojected the data to the Canada Albers Equal Area projection per ABoVE specifications. Next, we used the ABoVE-C high-resolution grid [Loboda et al., 2018] to clip flight lines to individual tile extents and combine the six radar products into multiband GeoTIFFs, for simplified spatial-temporal referencing [Fayne et al., 2019].

For the ABoVE 2017 campaign, the AirSWOT aircraft integrated a color-infrared (CIR) digital camera that collected data in green (520-600nm), red (630-690nm), and near-infrared (760-900nm) wavelengths at 1-meter spatial intervals simultaneously with radar acquisitions [Kyzivat et al., 2018, https://doi.org/10.3334/ORNLDAAC/1643]. Using these data, a mask of open water extent was produced [Kyzivat et al., 2019, https://doi.org/10.3334/ORNLDAAC/1707]. This product identifies areas of open water not impacted by aquatic or riparian vegetation, which is particularly important for this study because the inclusion of emergent vegetation would contribute to vertical elevation error in retrievals of WSE. SWOT water-detection algorithms are not appropriate for AirSWOT due to instrument geometry differences, necessitating the use of a reference water mask for AirSWOT radar. Lower incidence angles used in SWOT will allow direct water detection without the use of an onboard camera. An example of the water mask applied to the elevation data for the Peace-Athabasca Delta, Canada is presented in Figure 2.

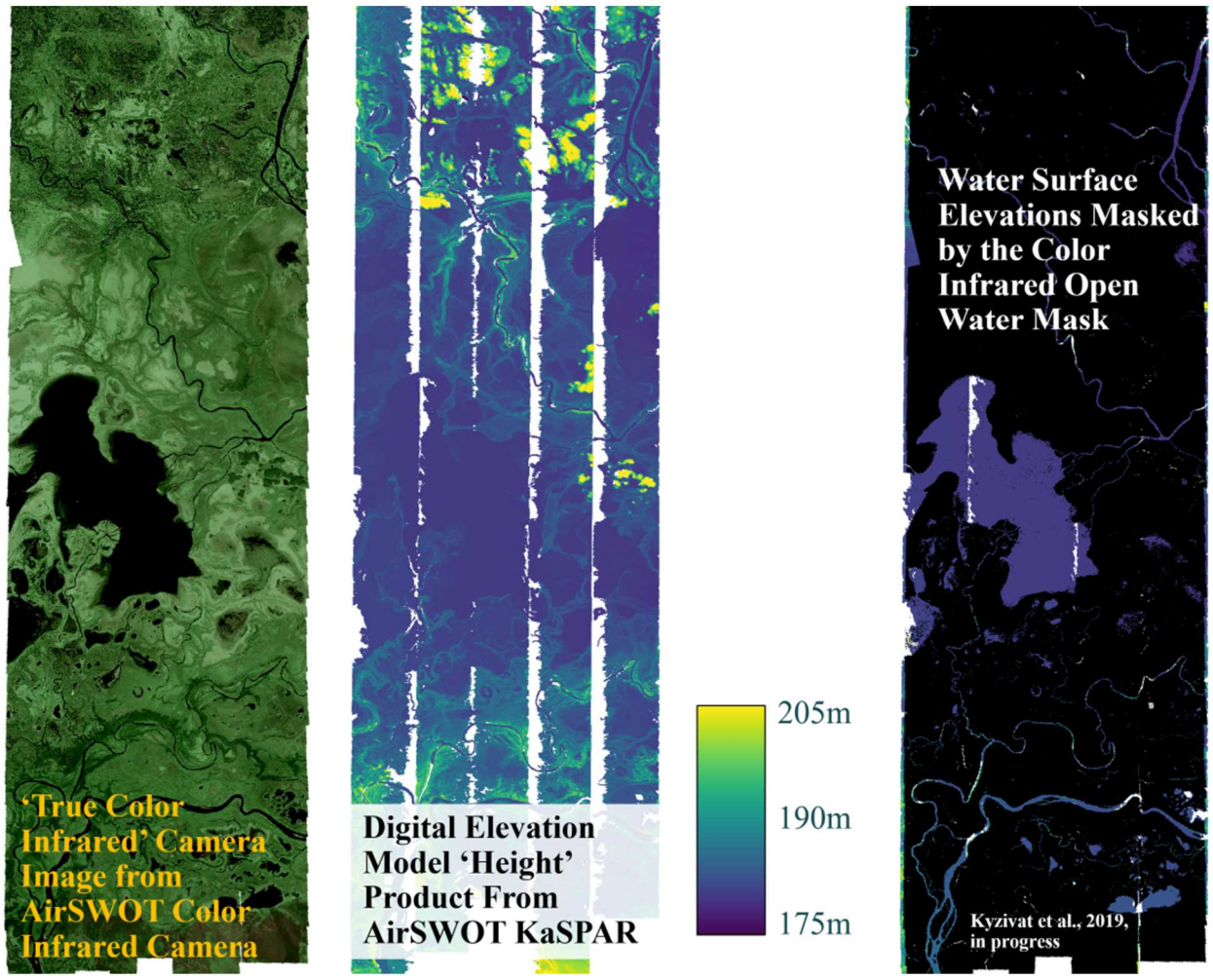

Figure 2.. *Peace-Athabasca Delta, August 13, 2017. Composited data from the CIR Camera, AirSWOT Height Product, and color infrared open water mask are shown here. The vertical striping in the AirSWOT DEM (center) shows the individual flight lines in color, with white showing gaps between flight lines. The image on the right shows the AirSWOT DEM with the open water mask applied on top, black areas are land, highlighting the AirSWOT water surface elevations in purple and blue.*

2.2.1.1 InSAR Data Processing to Produce Elevations (supplement)

The AirSWOT InSAR processor requires reference elevation and water surface extent maps to help solve for the geolocation and elevation during phase unwrapping, which are used to "flatten" the InSAR phase, removing the effects of propagation delay and DEM topography. After phase unwrapping, the geolocation and elevation of each pixel is refined using the

estimated InSAR phase. The digital elevation model used for the ABoVE processing comes from MERIT [Yamazaki et al., 2017], which represents the elevations as orthometric heights with respect to the EGM96 geoid. Because the InSAR processor uses elevations with respect to the WGS84 ellipsoid, and not orthometric elevations, the MERIT DEM's vertical datum was converted to WGS84 before processing. The reference water mask used to estimate the spatial extent of water bodies is from the Global Surface Water Occurrence dataset [Pekel et al., 2016]. The occurrence water data uses 30 meter historical Landsat data to estimate how frequently an area is inundated with water, from 0 - 100% occurrence. For processing with AirSWOT, the occurrence data is binarized at the 70 percent level, in order to include water bodies that are present at least 70 percent of the time.

From the initial output of the InSAR processor, flight transects are analyzed at the regional scale as bundles of neighboring and overlapping flights. During this post-processing stage, we check for phase unwrapping and phase calibration errors which contribute to tilts in the surface, elevation errors tens of meters from true elevation, and geolocation errors. Because each flight transect has at least two overlapping acquisitions from July and August, and the elevation of land is not expected to change significantly, the water mask [Pekel et al., 2016] is used to remove the water bodies and compare the elevation difference of the land areas covered by both flight lines. The difference maps are used to refine the phase calibration of each flight line by solving for the InSAR phase biases that reduce the elevation difference between the overlapping land areas. The elevation differences are also visually assessed for relative tilts between the lines, and where possible are corrected to remove anomalous elevation trends. Surface elevations will not be perfectly matched due to instrument noise and constraints imposed by the relationship

between InSAR phase and elevation, allowing the possibility of WSE changes between dates.

For more details on radar processing and correction techniques, see Denbina et al., [2019].

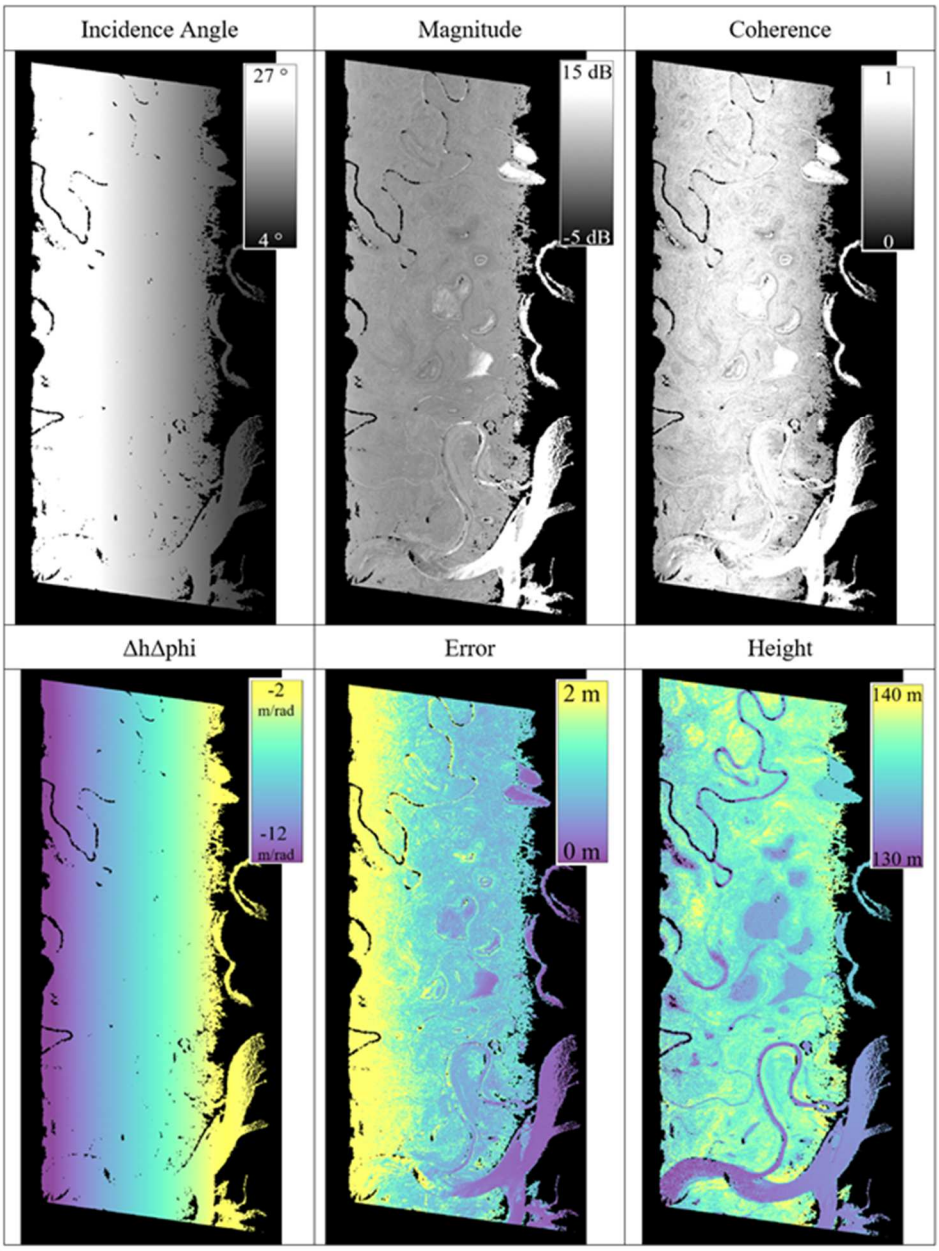

Figure 3. *2017 ABoVE AirSWOT products that have been publicly released from JPL include height (elevation), magnitude (backscatter), coherence, incidence angle, Δh/Δphi (sensitivity factor of estimated elevation to InSAR phase), and error (elevation random uncertainty). Note that*

in the near range of the flight (in this instance, on the right), there are water bodies surrounded by missing-data fill values.

2.2.2 LVIS Airborne LiDAR Data

Since 1997, the Land Vegetation and Ice Sensor (LVIS) has been providing high-quality full-waveform elevation returns from the vegetation canopy to the ground with sub-decimeter accuracy [Blair et al., 1999]. Although no known studies have assessed LVIS's performance over open water, previous studies have identified elevation accuracies of less than 10 cm [Hyde et al., 2005; Hofton et al., 2008], making it a promising validation instrument for AirSWOT WSE assessments. During the ABoVE campaign, LVIS collected 1.8 km swath-width data having 10 m point spacing. By design, the 2017 ABoVE LVIS flight campaigns overlap with 35.3% of the 2017 AirSWOT flights [Figure 1], providing a sizeable reference elevation dataset at a scale that would be impossible to obtain with *in situ* measurements. The LVIS LiDAR data were acquired between June 29 and July 16, within days of the July 8-22 AirSWOT flights. The snapshot of WSEs from LVIS in July permits temporal change analysis to be conducted with AirSWOT data from July and August using appropriate LVIS reference elevations.

2.2.3 In-Situ Water Level Sensors

Sixty-three lake surveys and additional river profiles were collected by GPS-mounted floating Water Surface Profilers (WaSPs) spanning 17° latitude [Pitcher et al., 2020]. Solinst® Levelogger pressure transducers were also installed to record WSE at 15-minute intervals for 18 lakes used in this study [Figure 1]. Using these *in situ* data, a previous study [Cooley et al., 2018] demonstrated a seasonal hydrological drawdown (WSE decline) between July 6 and August 19, with water levels decreasing 8-60 cm in the

Canadian Shield, and 15-60 cm in the Yukon Flats Basin. These measurements enable timing synchrony with AirSWOT overflights either through coincident GPS surveys or acquisition of continuous pressure transducer time series throughout the summer. GPS receivers were provided by UNAVCO, and the GPS Precise Point Positioning (PPP) solutions were processed at the Centre National d'Etudes Spatiales (CNES) using GINS software [Marty et al., 2011]. This collection of *in situ* WSE measurements from GPS surveys and pressure transducer time series is used here to compare differences between LVIS and AirSWOT WSEs.

2.3 Methods

We conduct four tests to determine how well 2017 ABoVE AirSWOT WSEs can be used to assess sub-seasonal variations in Arctic-Boreal surface water and to identify optimal data processing techniques to guide future AirSWOT and SWOT hydrologic science objectives. In order, we 1) assess the frequency of missing water data in the AirSWOT elevations; 2) compare AirSWOT WSE retrievals with *in situ* GPS measurements; 3) compare AirSWOT WSE retrievals with near-coincident LVIS LiDAR and determine best practices for filtering AirSWOT based on incidence angle, magnitude, coherence and elevation uncertainty; and 4) estimate sub-seasonal storage change by comparing temporally coincident AirSWOT-LVIS elevation differences, with temporally asynchronous differences between July and August.

2.3.1 Test 1 Assessment of missing data within water bodies

Strong Ka-band radar backscatter returns over water are required to produce accurate WSE retrievals and to validate SWOT. Therefore, the AirSWOT KaSPAR data products contain missing data values for pixels with insufficiently high backscatter or low coherence. Variations in aircraft

attitude produce a uniquely jagged edge in the near range, closest to the aircraft. There are also patches of missing data within the swath, particularly over water bodies, as seen in Figure 3. These patches are caused by specular reflection of the radar waves in the far range (i.e. incidence angles $\geq 17°$), which results in very low backscatter. Excessive areas of missing data have the potential to impact the accuracy of spatially averaged WSEs. To assess the fraction of water-only data presence at each incidence angle, data presence statistics are extracted for water bodies within the CIR open water mask.

2.3.2 Test 2 Comparison with in situ GPS measurements

To quantify potential biases and outliers in AirSWOT derived WSEs, measurements from WaSP GPS systems [8] are directly compared with spatially-averaged AirSWOT data. AirSWOT WSE data for individual pixels are noisy [Altenau et al., 2017; Pitcher et al., 2018; Tuozzolo et al., 2019; Denbina et al., 2019], so it is not recommended to compare GPS measurements directly with the elevation value of the single nearest AirSWOT WSE pixel. To enable a fair comparison with in situ GPS data, we take the average elevation of all AirSWOT water masked pixels within a $(250\ \text{m})^2$ area (SWOT minimum averaging window) around each GPS point.

2.3.3 Test 3 Comparison with ABoVE LVIS airborne LiDAR WSEs

As LVIS elevations are categorized as percentages of the returned energy waveform, we first compare *in situ* GPS measurements with LVIS waveforms for each GPS observed water body to determine the appropriate relative height (RH) elevation product to be used for LVIS WSE retrieval. Next, we rasterize and compare LVIS WSE with AirSWOT WSE on a pixel-to-pixel basis, and compare again after spatially averaging lakes. To produce the pixel-to-pixel comparison,

the open water mask was used to extract all of the LVIS pixels within the mask. The selected LVIS pixels are then used to extract the nearest neighbor AirSWOT elevations, providing a pixel-to-pixel comparison of LVIS and AirSWOT WSE over open water bodies including lakes and rivers. AirSWOT acquisitions more than 14 days from the July LVIS acquisition are not included in the elevation validation. The pixel comparison is a useful tool to compare between datasets, particularly over rivers where spatial averaging over long slopes will not yield an appropriate average elevation. It also provides a detailed view of how radar parameters such as incidence angle, magnitude, coherence and elevation uncertainty contribute to increasing errors in the AirSWOT WSE, providing an opportunity to assess best practices in pre-filtering AirSWOT WSE before spatial averaging.

To arrive at a representative elevation measurement for lakes, spatial averaging is recommended. Similar to previous studies where large elevation outliers are manually removed [Altenau et al., 2019] or where elevations are manually constrained to 3 meters around the mean elevation for the region [Denbina et al., 2019], this study uses a reference DEM to remove elevation outliers. The MERIT DEM is used to reduce noise and remove outliers in AirSWOT elevations where the AirSWOT elevations deviate more than 5 meters from the MERIT DEM, following MERIT's 5 meter elevation uncertainty. Finally, LVIS and AirSWOT data are again extracted from each water body and AirSWOT pixels are filtered using the radar parameters to produce spatially averaged mean lake elevation for lakes larger than $(250\text{m})^2$.

2.3.4 Test 4 AirSWOT Sub-Seasonal Variability

LVIS data can be used to normalize the differences between AirSWOT observations, enabling a broad-scale assessment of change in water level over time. AirSWOT-AirSWOT WSE

comparisons can be made, although noise and errors in the current measurements may amplify the uncertainty in the sub-seasonal water level assessment. July LVIS measurements are used as a temporal reference for AirSWOT to assess sub-seasonal storage changes between July and August. The mean difference between LVIS and AirSWOT WSEs is expected to be small on coincident days, but that difference may change along with seasonal water level changes. For example, if the mean WSE difference between July AirSWOT and July LVIS is -0.5m in a given region, and the mean WSE difference between August AirSWOT and July LVIS is -0.9 m, this would suggest that water levels in that region declined by 0.4 m on average. When applied to lakes clustered across the landscape, this analysis allows us to estimate the seasonal WSE trend. Pressure transducers distributed from Yukon Flats, Alaska, to the Canadian Shield in the Northwest Territories highlight the variation in hydrological change across the northern ABoVE domain and are used to validate the sub-seasonal storage change observed from the AirSWOT-LVIS comparison.

2.4 Results

2.4.1 Missing data within water bodies

Figure 4 summarizes the mean and median percent data presence across incidence angles for all data within water bodies. For water located at incidence angles <5°, less than 60% of expected pixels are available, which is reasonable given they lie outside of the nominal extent of the outer swath. Within the nominal AirSWOT outer-swath extent, an average of 70% of data is present over known CIR-mapped water bodies, with data losses associated with forward specular scattering in the far range. Usable radar returns are more consistently available (~85% presence)

between 5-17°. While the nominal radar swath-width is ~3.2 km, the total swath-width from nadir may be little more than 4 km. Missing data can additionally be attributed to aircraft movement, producing a noticeably jagged edge at 3-5° incidence angles.

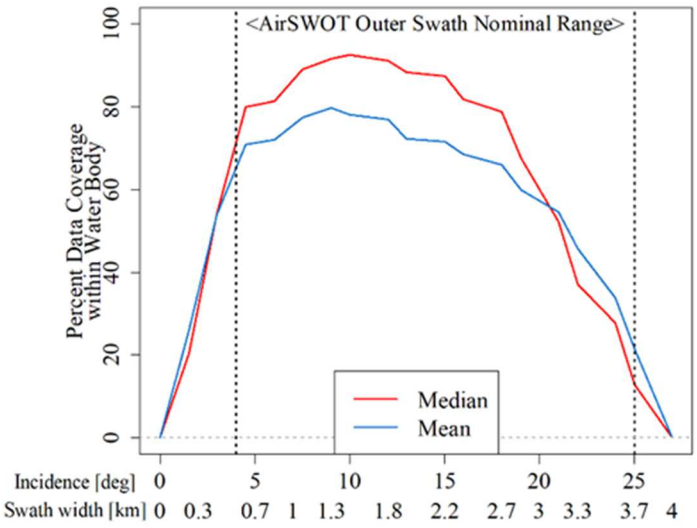

Figure 4. *Approximately 70% of the AirSWOT radar data are recovered within the nominal swath range, with rapid data loss <4° and >17°. WSE Data is present mostly at > 4 degrees of incidence.*

2.4.2 Comparison with in situ GPS

Of the 63 *in situ* WaSP GPS observations available, only 26 had pairs with AirSWOT matching the minimum water body size and AirSWOT data coverage. GPS observations [Pitcher et al., 2020] are strongly correlated with AirSWOT WSEs averaged across $(250\ m)^2$ areas around each GPS survey point [Figure 5a]. However, a bias of approximately -58 cm (std.dev=27 cm) is found between the two datasets, with AirSWOT WSEs lower than *in situ* WSEs. Overall, the full-resolution AirSWOT WSEs have a 1-2 meter elevation range within the $(250\ m)^2$ subset of the individual water bodies. This further demonstrates the inherent noisiness of these WSE retrievals and the necessity for spatial averaging within water bodies to yield useful estimates of WSE. The statistics for all WaSP GPS - AirSWOT lake pairs are found at the end of this chapter [Table 1].

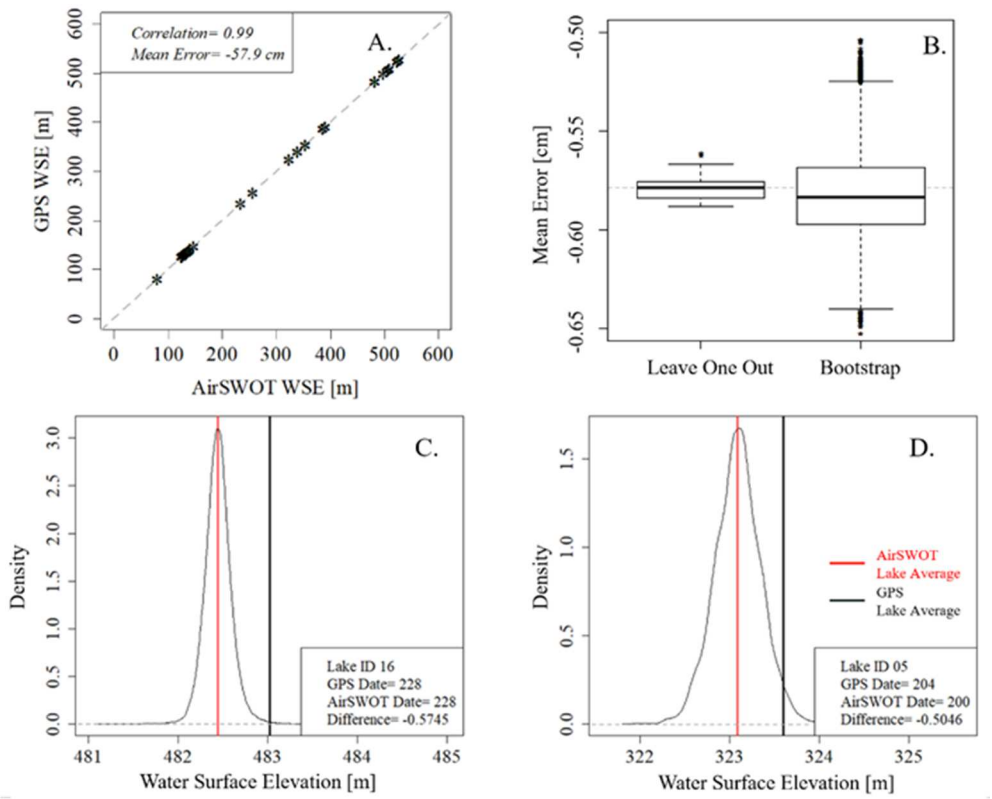

Figure 5. *In **A**, GPS elevations are sampled from 26 lakes across the ABoVE Domain and are correlated with AirSWOT WSE measurements (r^2=0.999). While correlated, AirSWOT WSEs display a mean bias of -58 cm relative to GPS WSEs. Uncertainty analysis using leave-one-out and bootstrapping (20,000 iterations leaving out 1/4th of the data, with replacement) in **B** demonstrate the sensitivity of the bias estimate to the samples of the GPS data used. For leave-one-out and bootstrapping tests, the means are -57.9 cm and -58.2 cm. The 25th and 75th percentiles for leave-one-out are -58.3 cm and -57.6 cm, while bootstrapping are -59.8 cm and -56.8 cm. Density distributions of pixels with (250 m)^2 open water areas for three representative lakes with in situ WaSP surveys are shown (in **C and D**) highlighting the noisiness in the data, having a range of up to two meters from the mean. The GPS measurement is represented by a black vertical line while the mean AirSWOT measurement is shown in red.*

2.4.3 Comparison of AirSWOT WSE with LVIS WSE

Via comparison with *in situ* WaSP GPS, the LVIS RH65 elevation data were determined to be the closest approximation of the GPS WSE (Figure 6). Using the LVIS RH65 product, the average of the pixel-to-pixel differences between LVIS RH65 WSEs and AirSWOT WSEs yields a mean error bias, with AirSWOT WSEs 63 cm lower than LVIS. The AirSWOT-LVIS mean

error plotted against incidence angles show no trend. As reported in previous studies [Moller et al., 2010, Wu et al., 2011], we find a clear correlation between incidence angle and absolute error (Fig. 7).

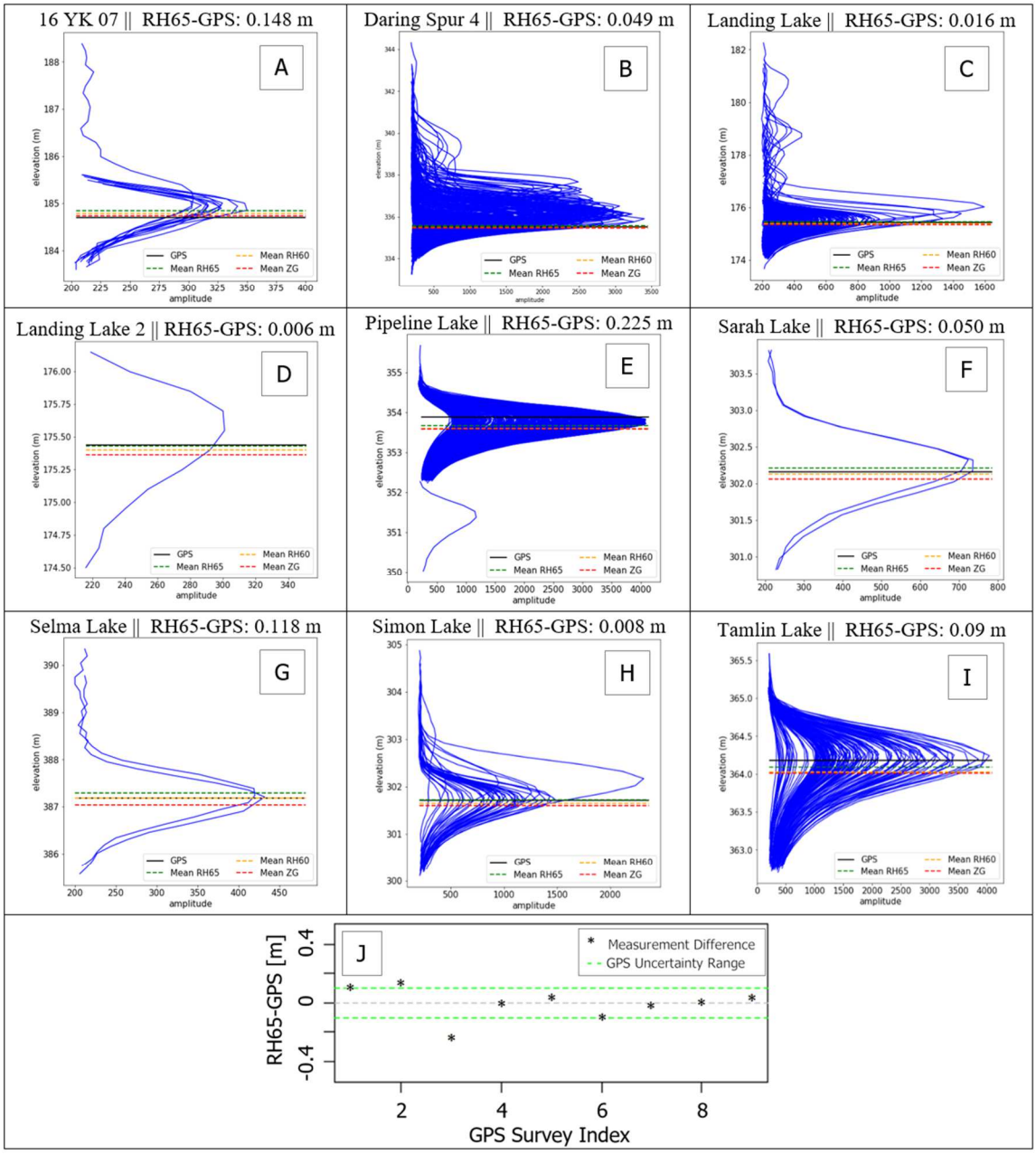

Figure 6 ***(A-I)****. For nine selected lakes with collocated GPS and LVIS measurements, all LVIS waveforms within the lakes are shown, with vertical axis limited to an interval near the amplitude peak. The large amplitude peak corresponds to strong energy returns from reaching the impenetrable surface. The GPS elevation is shown as a solid black line. The 60-65% energy return*

(referred to as RH60 and RH65) and mean estimated ground elevations from LVIS are shown as the orange, green, and red dashed lines, respectively. ***J.)*** *When compared across all 9 GPS stations, the RH65, 65% energy return level, is often within the GPS measurement uncertainty range for open water, providing the conclusion that the LVIS RH65 data can be used as a proxy for in situ GPS measurements. In two out of the nine regions examined, a single stray waveform skewed the mean.*

Filtering recommendations can be made by identifying which incidence angles reduce the standard deviation and mean absolute errors. Viewing the relationships between mean absolute error and incidence angle, coherence, backscatter, and elevation uncertainty in the radar products suggests how to achieve WSE with higher accuracy and precision, reducing the noisiness seen in Figure 5.

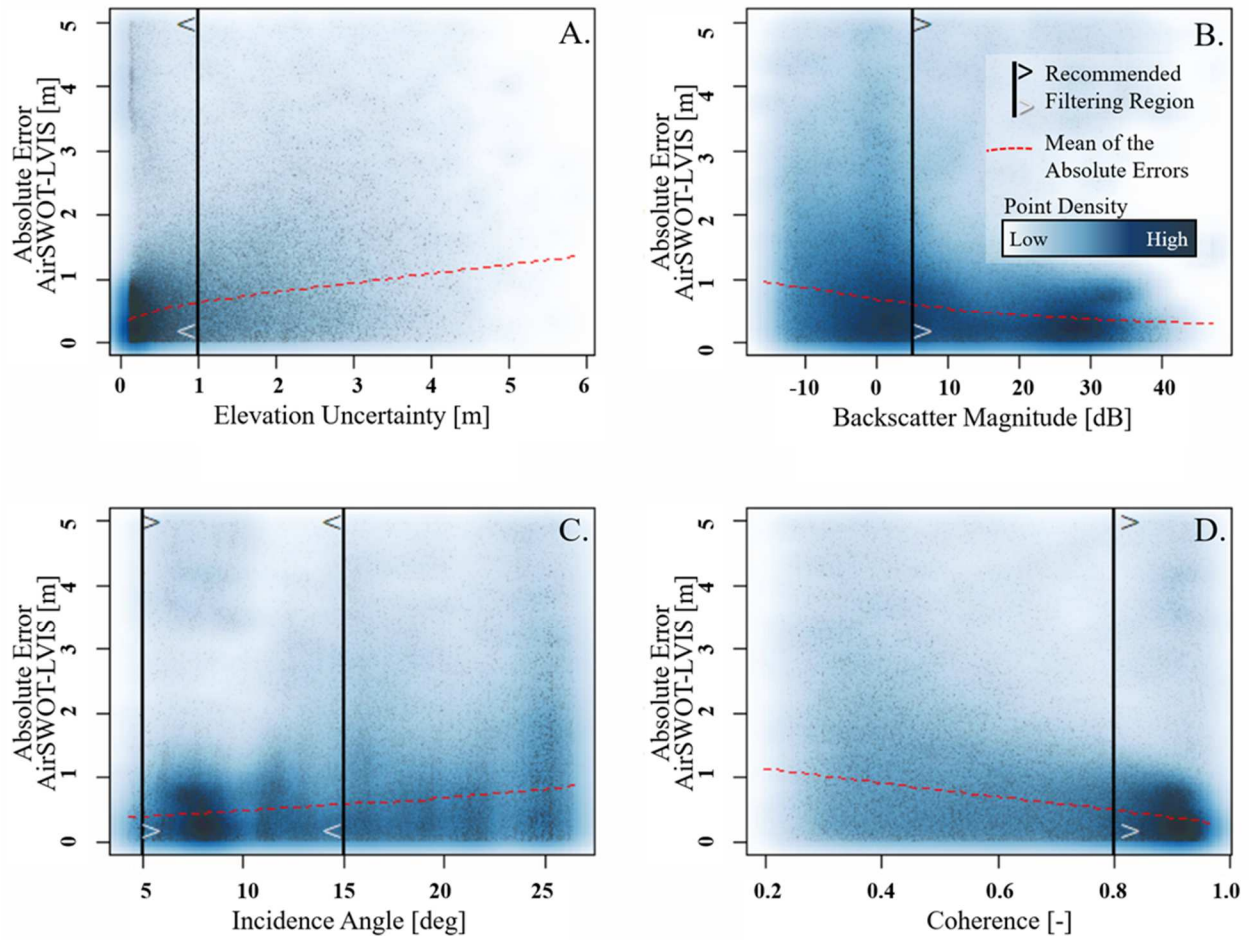

Figure 7. *Relationships between the mean absolute error derived from the difference between AirSWOT WSE and LVIS WSE and the AirSWOT radar products pixel-to-pixel comparison provide four distinct filtering boundaries on the AirSWOT radar products:* ***A.*** *Elevation Uncertainty* ***B***. *Magnitude* ***C.*** *Incidence, and* ***D.*** *Coherence. The filtering boundary of desired data is shown as a black line with directional arrows. A red local regression line shows how the absolute error decreases or increases with changing radar parameters. The scatterplot is represented as a smoothed point cloud demonstrating the density of points; points are tightly clustered where the point cloud is dark blue, and sparse where the cloud is light or white.*

Figure 7 demonstrates absolute error relationships with the AirSWOT radar products, with positive correlations with elevation uncertainty and incidence angle, and negative correlations with magnitude and coherence. It is recommended that AirSWOT ABoVE 2017 data users isolate data where the elevation uncertainty is less than 1 meter, magnitude is greater than 5 dB, the incidence angle is between 5 and 15 degrees, and the coherence is greater than 0.8. These filtering recommendations provide insight into the spread of error values and into how precision and accuracy can be improved. Filtering the data reduces the bias in the pixel-based analysis from -63 cm to -54 cm. Bias correcting the data by adding 54 cm produces a mean absolute error (MAE) of 35 cm.

The reported bias is slightly different for spatially averaged lakes. Users are advised to spatially average AirSWOT WSE data to reduce noise, arriving at a single mean WSE value. Applying the filtering recommendations and removing pixels for which the absolute difference from the reference MERIT DEM is greater than 5 m, we extract AirSWOT WSEs from lakes greater than $(250\text{m})^2$ and average the lake elevations, producing 1,043 LVIS-AirSWOT lake coverage pairs across the entire domain. While the 1,043 AirSWOT - LVIS lake pairs are correlated, scattered outliers greater than 20 meters skew the mean error between the two datasets to -88 cm (Fig. 8). As the pairs are within 1 m about 80% of the time, the 805 lake pairs having a

mean WSE error of -45 cm (blue in Figure 5a, b), can be used in further temporal analysis. Adding 45 cm for bias correction produces a MAE of 27 cm.

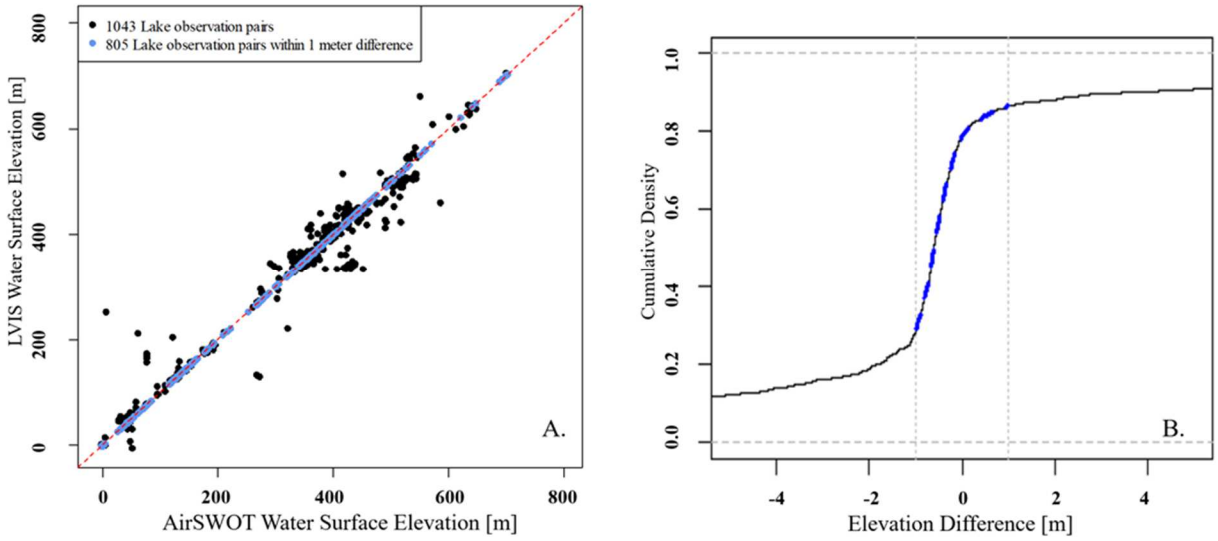

Figure 8. *Black dots in **A** and line in **B** show AirSWOT vs. LVIS WSE after adding the MERIT reference elevation filter, using all 1043 available AirSWOT-LVIS lake observation pairs. Blue dots **A** and line in **B** show AirSWOT WSE vs. LVIS WSE after reference elevation filtering and limiting the absolute difference between AirSWOT and LVIS to 1 meter using 805 available AirSWOT-LVIS lake pairs.*

2.4.3.1 Solid earth tides as a source of elevation bias

Possible bias sources include residual artifacts in the radar processing, signal delay, or solid earth tides. While all three datasets use the same reference vertical datum, as elevation above the WGS84 ellipsoid, differences in elevations for AirSWOT, LVIS, and Water Surface Profiler (WaSP) GPS may be attributed how solid earth tides are treated in the measurement and derivation of those elevations. Solid earth tides may vary by approximately 35 cm [Hendershott 2005]. AirSWOT elevations are produced with solid earth tide correction, which may be different from the treatment of other reference datasets used in this study. Solid earth tides vary over space and

time, having the potential to create biases which are also spatially and temporally varying. This is particularly relevant with the 2017 ABoVE AirSWOT campaign, as the data collection spans 23 degrees of latitude over the course of two months. Here, we consider that large biases on the order of 40-50 cm are unlikely due to true measurement error, but can be attributed to differences in how elevations are referenced relative to solid earth tides.

2.4.4 Sub-seasonal Variability in WSE

Finally, we assess WSE changes mapped by AirSWOT and LVIS WSE over time [Figure 9]. To summarize regional and sub-seasonal variability, AirSWOT-LVIS lake differences are aggregated into 29 sub-regional clusters based on the grouping of the AirSWOT flight lines (Figure 3 shows the flight lines for the Peace-Athabasca region, for example). Similarly, AirSWOT-AirSWOT WSE pairs can be used for this analysis, although errors inherent in the lakes used in the pairing cannot be normalized, amplifying the uncertainty in the sub-seasonal water level assessment. A previous study of summer 2017 lake variation demonstrated shrinking lake areas between July and August [Cooley et al., 2019], corresponding to a seasonal drawdown of lake water storage. Eighteen pressure transducers (PTs) placed in lakes ranging from the Yukon Flats, Alaska, to the Canadian Shield demonstrate the sub-seasonal hydrological drawdown between July 6 and August 19, 2017 (day-of-year 187-231). Despite the spread in aggregated WSE elevation differences in lakes present in the time-series analysis represented in Fig. 9, there is a trend in the elevation difference between AirSWOT and LVIS, aligning with the change in water surface elevation from PTs. During this time WSEs from PTs decreased by 7-35cm, while AirSWOT shows a mean WSE decrease across the region of 17 cm.

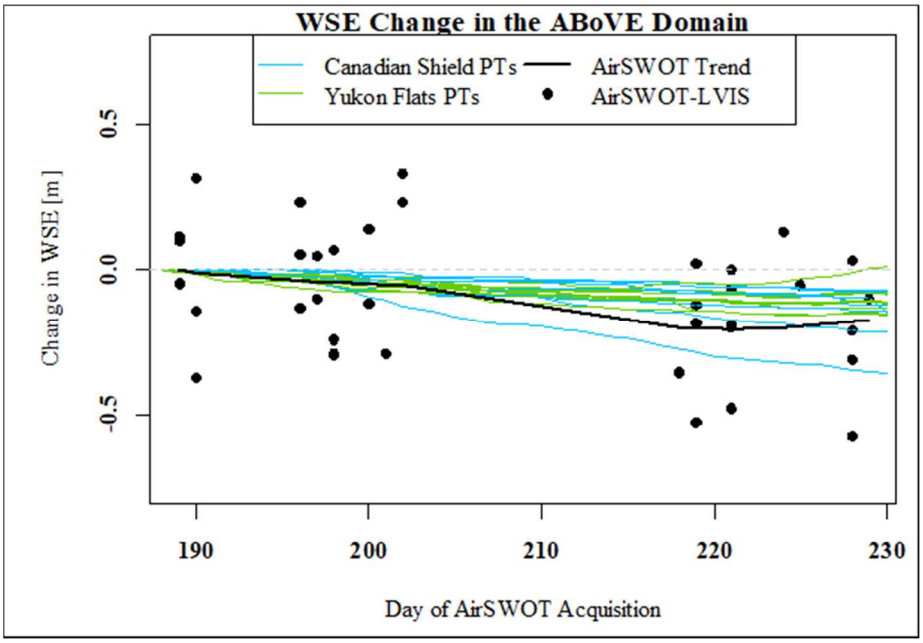

Figure 9. *After bias correction (see Figures 7 and 8), spatially-averaged AirSWOT WSEs reveal a broad-scale drop in lake levels averaging ~17 cm across the ABoVE domain over the period July 8-August 17, 2017. This finding is consistent with in situ time series of WSE acquired by 18 pressure transducers (colored lines: July 6- August 19, 2017). The 805 LVIS-AirSWOT lake pairs (from Figure 8) have been aggregated into 29 regions (black dots). Reference datum (0 m) is relative to LVIS WSEs acquired in early summer.*

2.5 Conclusion

This study demonstrates the spatial and temporal capabilities of AirSWOT to map Arctic-Boreal lake WSEs and their sub-seasonal changes over time, as well as strengths and limitations of AirSWOT data collection and analysis across a >22,000 km^2 region of the North American Arctic-Boreal region. AirSWOT radar retrievals of WSE across the ABoVE domain [Fayne et al., 2019] were evaluated using precise *in situ* GPS measurements acquired by WaSP [Pitcher et al., 2010], *in situ* pressure transducers [Cooley et al., 2019], and LVIS airborne LiDAR data [Blair et

al., 2018]. For AirSWOT WSE retrievals to be beneficial to both hydrologic science and SWOT validation goals, its spatially-averaged values must meet or exceed SWOT elevation mean absolute error requirements of 25 cm for water bodies $(250\ m)^2$ and 10 cm for $(1\ km)^2$ water bodies [Desai et al., 2018]. AirSWOT radar should also secure useable returns over open water bodies. In support of ABoVE hydrology goals, AirSWOT WSEs should be able to capture Arctic-Boreal water storage changes. The immense ABoVE dataset presented here is thus a significant opportunity for both Arctic-Boreal hydrologic science and pre-launch SWOT mission planning.

A missing data analysis [Figure 4] confirms that forward, specular scattering increases with higher incidence angles in flat water bodies [Grant et al., 1957], reducing the amount of backscatter returned to the AirSWOT radar sensor at incidence angles greater than 17°. However, missing data do not necessarily preclude retrieval of useful WSE measurements, as remaining data are still useful for estimating the WSE. Seemingly low data presence does not necessarily signify that entire water bodies are missing, but rather that fractional returns from water result in reduced data availability for spatial averaging and thus potential for greater error in WSE. To mitigate this problem in future AirSWOT campaigns, we agree [Pitcher et al., 2020] that increasing the overlap of flight lines would ensure areas experiencing specular scattering have multiple observations, more specifically focusing on incidence angles greater than 17°.

Spatial averaging and various filtering techniques applied AirSWOT WSEs reduce noise and constrain random error in the WSE, producing mean error biases ranging from -45 cm to -88 cm for all observed water bodies. Possible bias sources include residual artifacts in the radar processing, signal delay, or solid earth tides. Random WSE errors in the AirSWOT elevation product are reduced by applying the recommended filters of incidence angle (5-15 degrees), coherence (>0.8), magnitude (>5 dB), and elevation uncertainty (<1 meter) available in the

accompanying products. Previous studies used similar filtering techniques, as well as visual identification to select and manually remove regions of anomalous elevation values [Altenau et al., 2017], while others automatically remove outliers based on an expected elevation range [Tuozzolo et al., 2018; Denbina et al., 2019].

Seasonal water storage change can be assessed by applying the filtering recommendations to AirSWOT flight lines and aggregating the AirSWOT-LVIS differences into 29 sub-regions across the ABoVE domain. Here, we identify an overall hydrologic drawdown of -17 cm across the ABoVE domain between July 8 and August 17, 2017, consistent with a -22 cm drawdown recorded with *in situ* pressure transducers installed in lakes across the ABoVE domain for AirSWOT WSE validation [Cooley et al., 2019]. Using aggregated regions enables a seasonal water storage assessment, reducing the impacts of noise and errors found at the individual lake level. Because of residual errors in the WSE following filtering and spatial averaging, ABoVE AirSWOT data users are advised to examine multiple lakes or rivers (n>50) in a given study area to identify relative changes in WSE rather than absolute elevations.

While our results suggest a large spread in mean error values across the ABoVE domain, previous studies of AirSWOT WSE focused on particular regions such as the Tanana River [26, 30], Yukon Flats [Pitcher et al., 2018], Willamette River [Tuozzolo et al., 2019], and the Mississippi River Delta [Denbina et al., 2019]. As these examinations included the first AirSWOT datasets ever produced, JPL engineers were able to focus on these smaller regions to correct and reprocess data as necessary, before the datasets were released to scientists. Unlike earlier studies, this study encompasses an immense region, covering 23 degrees of latitude and with 128 flight lines covering a 22,775 km^2 area. Due to the size of the ABoVE collection, JPL engineers used

more automation in preparing the data, significantly limiting manual corrections and multiple re-processing attempts before releasing the data. Being an experimental instrument, there have been multiple modifications and repairs made to the AirSWOT radar since 2014, resulting in slightly different product quality between studies and differences in reported error statistics across studies are expected. Future research directions for AirSWOT error analysis could include quantifying non-instrument sources of error, such as how water movement, wind, rain, and vegetation intrusion impact the AirSWOT radar signal, potentially contributing to errors observed across studies despite instrument changes.

Finally, we can answer the questions: *How well did the AirSWOT radar map water surface elevations across the ABoVE domain? Can AirSWOT WSEs be used to measure storage change at seasonal time scales?* We conclude 1) there is a correctable mean bias of -45 cm in the 2017 ABoVE AirSWOT collection relative to LVIS WSEs that is identified after filtering the AirSWOT elevation, 2) bias correcting the WSE data produces a mean absolute error of 27 cm, similar to the SWOT 'total height error' requirement of 25 cm for water bodies between $(250\ m)^2$ and 1 km^2, and 3) AirSWOT can detect decimeter scale water level changes over large regions. Through spatial averaging, vigorous filtering and bias correction of AirSWOT WSE retrievals, small vertical changes in water surface elevation are detectable at the landscape scale, demonstrating the capacity of the AirSWOT data for broad-scale Arctic-Boreal hydrologic mapping and SWOT validation purposes.

Table 1. A subset of the 63 water surface elevation (WSE) surveys collected from Water Surface Profiler (WaSP) floating GPS devices [Pitcher et al., 2020] are used to validate 2017 NASA Arctic Boreal Vulnerability Experiment (ABoVE) AirSWOT KaSPAR observed lakes.
Due to repeat coverage of the same lakes, the AirSWOT observed lake WSE may be compared with the same WaSP GPS measurement multiple times. AirSWOT KaSPAR may image the same lake multiple times in the same day, producing additional GPS-AirSWOT lake pairs for comparison.

Lake ID	Longitude	Latitude	GPS Date	AirSWOT Date	Days Apart	GPS WSE [m]	AirSWOT WSE [m]	Diff [m]	AirSWOT Pixels, N
2	-133.5288	68.7526	198	197	-1	79.6726	79.2422	-0.430382	2331
4	-148.8473	69.037	204	200	-4	387.2296	386.583	-0.646344	2576
4	-148.8473	69.037	204	202	-2	387.2296	386.687	-0.542281	263
5	-148.8585	69.1669	204	200	-4	323.5982	323.346	-0.252361	13
5	-148.8585	69.1669	204	200	-4	323.5982	323.094	-0.504591	3544
6	-148.8177	69.0061	204	200	-4	353.9454	353.515	-0.430449	309
6	-148.8177	69.0061	204	202	-2	353.9454	353.449	-0.495972	1670
9	-106.1058	52.2066	229	228	-1	527.5217	527.195	-0.326847	1080
9	-106.1058	52.2066	229	229	0	527.5217	527.024	-0.497583	2885
11	-107.2051	52.7135	187	189	2	482.9965	482.77	-0.226575	58195
11	-107.2051	52.7135	187	189	2	482.9965	482.792	-0.204806	8749
12	-107.2168	52.6684	189	189	0	483.095	482.77	-0.325075	58195
12	-107.2168	52.6684	189	189	0	483.095	482.792	-0.303306	8749
13	-106.092	52.2026	229	228	-1	523.7553	523.441	-0.314253	108
13	-106.092	52.2026	229	229	0	523.7553	523.255	-0.500518	93
16	-107.2058	52.7135	228	228	0	483.0227	482.417	-0.605587	73382
16	-107.2058	52.7135	228	228	0	483.0227	482.448	-0.574546	135524
16	-107.2058	52.7135	228	229	1	483.0227	482.369	-0.653316	157023
16	-107.2058	52.7135	228	229	1	483.0227	482.314	-0.708316	167697
18	-107.2117	52.6758	228	228	0	483.0603	482.417	-0.643187	73382
18	-107.2117	52.6758	228	228	0	483.0603	482.448	-0.612146	135524
18	-107.2117	52.6758	228	229	1	483.0603	482.369	-0.690916	157023
18	-107.2117	52.6758	228	229	1	483.0603	482.314	-0.745916	167697
22	-107.0826	52.6606	185	189	4	498.8452	498.588	-0.257691	111
26	-107.0572	52.6526	185	189	4	509.0371	508.864	-0.173152	34
28	-107.0605	52.6528	185	189	4	506.4899	506.3	-0.190385	116
37	-111.6683	64.8351	190	196	6	391.123	390.608	-0.51539	10866
41	-113.2135	63.8692	190	196	6	340.4361	340.038	-0.398372	426861
41	-113.2135	63.8692	190	196	6	340.4361	340.103	-0.333469	735
45	-114.1571	63.2189	191	196	5	256.5165	255.92	-0.596722	1215
48	-145.7919	66.7859	196	201	5	133.7659	133.021	-0.744547	64928
51	-145.5504	66.4561	196	198	2	137.2486	136.626	-0.622159	16825
51	-145.5504	66.4561	196	198	2	137.2486	136.693	-0.555745	48237
52	-146.3889	66.2458	196	201	5	127.4344	126.726	-0.708488	23418
52	-146.3889	66.2458	196	203	7	127.4344	126.734	-0.700041	11791
54	-146.3533	66.3836	196	201	5	126.8725	126.27	-0.602516	33
55	-146.4181	66.1739	196	198	2	134.3166	133.496	-0.820913	63302
55	-146.4181	66.1739	196	201	5	134.3166	133.553	-0.763855	91887
56	-146.6518	66.1831	197	201	4	126.1839	124.829	-1.35458	1772
56	-146.6518	66.1831	197	201	4	126.1839	124.869	-1.31492	40936
57	-145.8415	66.6778	200	201	1	129.4319	128.393	-1.03916	5785
58	-145.434	66.4324	196	198	2	139.0149	138.304	-0.711206	60837

59	-146.1487	66.1762	196	198	2	147.8695	147.147	-0.722204	27314
60	-146.2748	66.0755	197	198	1	234.5194	233.411	-1.10875	13877

Table 1

Chapter 3:

3. AirSWOT Ka-band Land Surface Interactions

Title: Characterizing Near-Nadir Ka-Band SAR Backscatter from Wet Surfaces and Diverse Land Covers

3. 1 Introduction

The inundation extent and water surface elevation of inland lakes, rivers, and wetlands are critical remote sensing measurements for monitoring the terrestrial hydrological cycle [Smith, 1997; Alsdorf et al. 2003; 2007; Schumann et al. 2009; Crétaux et al. 2011; Cooley et al. 2019; 2021; Frasson et al. 2019]. Remote sensing of inundation extent is complicated by riparian vegetation along shorelines and aquatic vegetation in shallow or flooded areas, especially with optical sensors [Kasischke et al. 1997; Hess et al. 2003; Kyzivat et al. 2019]. Both optical and microwave methods underestimate inundation extent where vegetation density outweighs observable water fraction, [Hess et al. 1995; Hess et al. 2003], or if conservative classification methods prioritize reducing misclassification over total extent [Kyzivat et al. 2019].

While long-wavelength, high incidence angle radars (especially L band) are traditionally favored for hydrological applications due to their superior vegetation penetration and in some cases, ground penetration, [Wdowinski et al., 2008; Hong et al., 2010; Kim et al., 2014; Bakian-Dogaheh et al. 2022], new low incidence angle short-wavelength radar systems can also measure water extent and water surface elevation effectively [Fjortoft et al. 2010; Wu 2011]. Because Ka-

band SAR can be highly sensitive to both liquid surface water (Ka band is additionally sensitive to frozen surface water, but these relationships are not discussed in this study) and vegetation, it is useful for terrestrial hydrology and ecological studies. Ka-band radars are sensitive to fine-scale scattering features (i.e. on the order of their wavelength, ~8 mm) suggesting better capability for detecting small standing and capillary waves on open water surfaces, for example, or the presence of non-woody emergent and/or floating aquatic plants. The short Ka-band wavelengths, therefore, have the potential to reveal different physical properties of wet and/or vegetated surfaces than conventional longer-wavelength C-, L-, and P- band radars. Nonetheless, to what extent such technologies can discriminate between diverse surface covers and differing moisture contents remains poorly understood [Fjortoft et al. 2010; Frappart et al. 2015; Fatras et al. 2016].

The forthcoming Surface Water Ocean Topography (SWOT) satellite mission (https://swot.jpl.nasa.gov/), developed by NASA and CNES with contributions from CSA and UKSA, will be the first Ka-band swath altimeter launched in space [Durand et al. 2010; Peral and Esteban-Fernandez 2018]. For land surface hydrology, the goal of the SWOT mission is to enable global, sub-monthly mapping of freshwater storage and river discharge for lakes as small as (250 m)^2 and rivers as narrow as 100 m [Durand et al. 2010]. To achieve this, open water surfaces must be readily identifiable in SWOT Ka-band imagery. Based on theoretical modeling and observations, accurate open water identification is anticipated due to strong backscatter returns from open water surfaces at near-nadir incidence angles (0.6-4.1 degrees) [Moller et al., 2010; Fjortoft 2010; Wu et al. 2011; Fjortoft 2014; Lobry et al. 2019]. However, preliminary observations of near-nadir (0-30°) Ka-band backscatter from AirSWOT, an airborne swath altimeter, suggest significant real-world complexity including relatively low backscatter returns from portions of some open water surfaces, and higher returns from some classes of land surfaces

[Fayne & Smith 2021]. Early AirSWOT assessments also report strong radar returns, similar to expected open water returns, from wetland vegetation and moist bare soils [Smith et al. 2014; Baney et al., 2014; Fayne & Smith 2021]. Such reports have raised concern within the SWOT science community about possible misclassifications of surface water [Smith et al. 2014; Smith et al. 2018], and have prompted a desire for improved understanding and modeling of Ka-band backscatter returns over inland water bodies and diverse land covers.

Software for analyzing radar backscatter (e.g. PolSARProSim, SNAP) are often developed for longer wavelengths (>5 cm), but to the authors' knowledge, no publicly available software can readily be used to simulate Ka-band scattering for hydrology applications including surface water and various land covers. Theoretical frameworks such as the Kirchhoff Approximation (KA), including the Geometric Optics (GO) and Physical Optics (PO) models [Hagfors 1966; Barrick 1968; Longhurst et al. 1973; Hajnsek & Papathanassiou 2005] are rigorous but computationally intensive for complex terrain. This is especially true when the terrain has diverse surface cover including bare soil, vegetation, and water, with a wide range of incidence angles. Using a small number of soil-only observations, one study simulated Ka-band backscatter from soils using a GO model for small incidence angles <7° [Fatras et al. 2016]. Empirical and semi-empirical models often require dual- or quad-polarized observations (HH, VV, VH, and HV) and assume that surface roughness variations are small relative to the wavelength [Oh et al., 1992, DuBois et al. 1995].

Because of the computational cost of the KA models, and the geometric restrictions of the empirical models (i.e. AirSWOT only uses VV, and the wavelength is much smaller than ground roughness features such as vegetation and water-wave-height variability), these modeling frameworks are not used in this study. Instead, we develop a simple empirical scattering model based on the statistical relationships between remotely sensed datasets. We assume that a simple

model should include surface dielectric properties, which we capture using moisture and temperature, and surface geometry, which we capture using surface roughness and structural complexity. For this analysis, roughness refers to intermediate-scale textural-geometric facets, which are larger than the wavelength, such as leaves and branches, in comparison with the 8 mm wavelength examined here. We do not apply any model to physically convert moisture and temperature to dielectric values, nor do we calculate a physical model of roughness. The dielectric component of radar backscatter modeling often focuses on moisture and ignores temperature (with some exceptions related to snow, ice, or permafrost [Ulaby & Stiles, 1981; Zhang et al. 2003; Mironov & Lukin 2009, Baghdadi et al. 2018]) because scattering is assumed to be much more sensitive to moisture than temperature [Jackson 1987]. For surface hydrology applications, other authors have not yet assessed the sensitivity of Ka-band scattering to surface temperature.

Traditional SAR and InSAR systems for land surface observations are typically C, L, or P-band (0.05 – 1 meter wavelengths), which are less sensitive to fine-scale surface features such as tree leaves and short, non-woody plants. Because the primary objective of these systems is to investigate land properties [Short et al. 2014; Mohammadimanesh et al. 2018; Brisco et al. 2019; Liao et al., 2020], they typically use larger incidence angles, averaging around 30° (±5°) and up to 50° [Kim and Liao 2021], that exhibit higher backscatter over land than over open water surfaces. In contrast, AirSWOT and SWOT use smaller incidence angles, producing higher backscatter returns over water than the surrounding land [Fjortoft et al. 2010; Wu et al. 2011;

Fayne et al. 2020; Desrochers et al., 2021]. AirSWOT acquires data in two swaths: an inner swath having an incidence angle range similar to SWOT (0.6–4.1°), and an outer swath which covers part of the inner range and extends to higher incidence angles (≲3–27°) [Moller et al. 2010; Wu et al. 2011]. Both swaths use vertical polarization for transmit and receive. The data in this study and those reported in previous studies [Altenau et al. 2017; Pitcher et al. 2019, Altenau et al. 2019; Tuozzolo et al. 2019; Denbina et al. 2019] are from the outer swath, and thus the range of incidence angles is large enough that the water backscattering varies significantly from one edge of the swath to the other, within the observed range of incidence angles. In this paper, "near–nadir" refers to the fairly broad incidence angle range 0–30° unless otherwise specified. For brevity, the phrase "near–nadir Ka–band backscatter" is shortened to simply 'backscatter' throughout the paper; and the term "Ka–band" is used to refer to the 35.75 GHz frequency (8 mm wavelength) of AirSWOT and SWOT. For detailed specifications of the AirSWOT and SWOT instruments see [Fjortoft et al. 2010; Moller et al. 2010; Wu et al. 2011; Fjortoft et al., 2014; Altenau et al. 2017; Pitcher et al. 2019, Altenau et al. 2019; Tuozzolo et al. 2019; Denbina et al. 2019].

Additionally, it is critical to identify regions with mixed pixels containing backscatter contributions from both land and water, as these may lead to classification errors and phase shifts resulting in elevation retrieval errors [Denbina et al. 2019; Fayne et al. 2020]. Surface water extent and resultant phase errors have implications for developing and validating future Ka-band instruments and future applications and validation of AirSWOT and SWOT. To assess these phenomenological sources of error, we must identify backscatter sensitivities to varying surface types and evaluate under what conditions water surfaces may be confused with other land types, which additionally has implications for mixed pixels at more coarse spatial scales than observed with AirSWOT.

This study advances physical understanding and modeling of Ka-band backscattering response across a diverse range of surface moisture conditions and land cover types by analyzing an extensive archive of AirSWOT Ka-band SAR data acquired across Alaska and western Canada for the NASA Arctic-Boreal Vulnerability Experiment (ABoVE) [Fayne et al. 2019]. First, we determine the separability of near-nadir Ka-band SAR backscatter for wet surfaces and diverse land covers to assess retrievals of water surface area. Next, we conduct an empirical investigation of the influence of surface moisture, temperature, and roughness on Ka-band surface scattering. These relationships are then used to develop a model to simulate near-nadir Ka-band surface scattering, called Ka-band Phenomenology Scattering (KaPS) model. For incidence angles 4-6°, we determine 1) open and vegetated water are clearly and robustly separable from surrounding dry land; 2) soil moisture variations are positively and strongly correlated with backscatter, while temperature variations have a minor influence on backscatter; and 3) surface geometry, as characterized with LVIS LiDAR complexity, is negatively correlated with backscatter as backscatter decreases with increasing vegetation density. KaPS can also simulate spatial and

temporal variations in Ka-band backscatter caused by changing surface moisture and roughness for broader incidence angles (1-27°). We conclude with a broader discussion of the study's implications for hydrological Ka-band remote sensing and backscatter modeling.

3.2 Data

3.2.1 The 2017 ABoVE AirSWOT Radar Data Collection

The AirSWOT Ka-band SWOT Phenomenology Airborne Radar (KaSPAR) is a multi-antenna, Ka-band wide-swath altimeter that uses InSAR processing to produce high-resolution maps of water and land surface elevations. AirSWOT was developed as an airborne complement to SWOT to test and design radar and InSAR algorithms and to understand surface phenomenological interactions at Ka band [Moller et al. 2010; Wu et al. 2011]. This study uses AirSWOT's outer swath data products, spanning near-nadir incidence angles (~3-27°). The radar data products used in the analysis are incidence angle, noise subtracted and calibrated backscatter, signal-to-noise ratio (SNR), and ungridded geolocation (LLHE) processed at the NASA Jet Propulsion Laboratory (JPL) [Fayne et al. 2019]. The published data are multi-looked and geocoded to produce final map products having a nominal pixel spacing of 3.6 meters, with various flight acquisition dates between July 8 and August 17, 2017. For technical descriptions of these data products and the AirSWOT instrument configuration see [Moller et al. 2010; Fayne et al. 2019]. The collection spans a large latitude gradient and captures a seasonal hydrologic drawdown [Fayne et al. 2020], enabling study of temporal changes in Ka-band backscatter due to surface moisture variability. Except for the SNR and LLHE radar products, these products are freely available for download [https://daac.ornl.gov/cgi-bin/dsviewer.pl?ds_id=1646 Fayne et al. 2019; 2020].

3.2.2 The 2014 ABoVE Landsat Land Cover Reference

The 2014 Arctic Boreal Vulnerability Experiment ABoVE Landsat Land Cover (LSLC) [Wang et al. 2019] product is used as a land cover reference. The 30 m LSLC is derived from Landsat-7 Thematic Mapper imagery and contains the annual dominant plant functional type represented as fifteen land cover classes (evergreen forest, deciduous forest, mixed forest, woodland, low shrub, tall shrub, open shrub, herbaceous, tussock tundra, sparsely vegetated, fen, bog, shallows/littoral, barren and water). Using a reference land cover dataset such as the LSLC is beneficial because it is well-documented that surface variations and land cover variability influence Ka-band backscatter, although previous analyses have been limited to water surfaces and broad forest types [Grant & Yaplee 1957; Waite & MacDonald 1971; Rodriguez et al. 2017; Desrochers 2021]. The extensive coverage area and moderate resolution afforded by the Landsat-based classification make it a very useful reference dataset to analyze Ka-band scattering coefficients for a more diverse range of land cover types than has been previously published.

3.2.3 NOAA Soil Moisture Reference

The NOAA Soil Moisture Products System (SMOPS) blended radiometer products [NOAA STAR, 2019] are used to assess broad-scale variations in surface moisture with 25 km spatial resolution and a daily temporal resolution. Additionally, the MODIS Land Surface Temperature (LST) products from the Aqua and Terra platforms [Zhengming et al. 2015] are used to assess variations in surface temperature at 1 km spatial resolution. Including data from both satellite platforms, the LST data has four daily observations, two in the morning and two in the evening, enabling a closer surface temperature estimate to the time of the AirSWOT overflights than daily observation data.

3.2.4 LVIS LiDAR Vegetation Complexity Reference

Airborne LiDAR data collected from the Land Vegetation and Ice Sensor (LVIS) [Blair et al. 1999] are used to assess the influence of facet-scale features on Ka-band scattering. The LiDAR data are collected within days of the AirSWOT flights and provide full-waveform analysis of surface characteristics. These full-waveform pulses are capable of penetrating canopies, providing detailed information on canopy and forest structure in diverse environments with reflected power at continuous elevation points along the height of the feature [Hyde et al., 2005]. LiDAR complexity is the specific LVIS product used for this analysis, which is included in the LVIS L2 Geolocated Surface Elevation Product dataset (Blair, J. B. and M. Hofton. 2018 https://nsidc.org/data/ABLVIS2). Complexity is also known as foliage height diversity and is also related to the leaf area index (LAI), which provides a measure of vertical heterogeneity and density [Tang and Armston 2019]. Low complexity values usually indicate flat ground or water surfaces, while high complexity values usually indicate dense canopies. The nominal pulse footprint spacing is 10 m, but the data has been resampled to 20 m to provide smoother coverage and transitions over the irregularly missing data.

3.3 Methods

3.3.1 Separability of near-nadir Ka-band SAR backscatter for wet surfaces and diverse land covers

To calculate the extent to which open water, emergent aquatic vegetation, wet soils, and land vegetation are separable (i.e. distinguishable) in Ka-band backscatter imagery, we compare

the LSLC reference land cover dataset with AirSWOT images as follows. First, we reproject the AirSWOT images to the same coordinate reference system as the LSLC, and convert the AirSWOT pixels to vector points to extract the land cover directly corresponding to each radar pixel using a nearest neighbor extraction. Next, the separability metric [Cumming and Van Zyl 1989; Baghdadi et al. 2001], defined as the difference between the linear backscatter means (μ) and standard deviations (σ) for each pair of land cover classes (class i and class j), is used to calculate separability of land cover classes from each other in the AirSWOT data. Land cover class pairs with separability values greater than 2 are considered separable, or unlikely to be confused when classified. For each pair of land cover classes i and j and each 3° incidence angle bin k the separability metric S is calculated as:

$$S_{i,j,k} = \frac{|\mu_{i,k} - \mu_{j,k}|}{\sigma_{i,k} + \sigma_{j,k}}$$

Eq. 1

Because this study is interested in identifying the occurrence of non-water observations being misclassified as water, the separability metric can be modified to refer to individual observations within the class. Here, we compare the group of observations from one class (j), with the means and standard deviations from the reference class (i) (excluding the standard deviation from class j, converted to 0 in the second equation).

$$S_{i,j,k} = \frac{|\mu_{i,k} - Obs_{j,k}|}{\sigma_{i,k} + 0}$$

Eq. 2

As a result of this calculation, Si,j,k will have the same number of values as the input observations from the class (j), giving each observation its own separability value. For each class (j) the fraction of the separability values greater than the reference separability threshold, 2, out of the total number of observations is assessed as the separability ratio.

3.3.2 Influence of surface moisture and temperature on Ka-band surface scattering

To assess the influences of moisture and temperature on Ka-band backscatter, the NOAA SMOPS soil moisture and MODIS surface temperature data are spatially and temporally downscaled to 1 km posting (moisture) and an hourly time step (temperature), to more closely approximate the spatial and temporal extent of AirSWOT acquisitions. The downscaling methods are summarized here and are explained in more detail in the supplement.

Prior to downscaling, each pixel of the 25 km soil moisture data is five times the swath width of the AirSWOT flight lines, allowing only broad-scale comparisons of regional moisture variations. Over the vast AirSWOT study domain during a time of seasonal hydrologic change in the region [Fayne et al., 2020], substantial changes in soil moisture are observed even in coarse resolution SMOPS data. The surface moisture data have a daily temporal resolution, sufficient for monitoring changing surface moisture for this purpose. However, SMOPS omits inland water bodies, complicating our assessment of AirSWOT radar backscatter over open water. To mitigate this, water bodies from the 30 m LSLC dataset are merged with the 25 km SMOPS dataset to produce a 1 km, higher resolution product. The soil moisture downscaling produces products that visually show both the original 25 km large pixel shapes and LSLC water bodies. We term this

final 1 km daily resolution downscaled product ‘surface moisture’ rather than ‘soil moisture’ because open water bodies are included. The spatial downscaling methodology is explained in more detail in the supplement (Figure S1).

The land surface temperature data has opposite scaling requirements compared with the surface moisture data; since temperature has diurnal variability, it is more important to have high temporal resolution temperature data at the MODIS 1 km spatial resolution. The MODIS observations occur in the morning and evening, with slightly shifting observation times around their nominal equatorial crossing times. Observations at the pixel scale occur zero to four times per day depending on cloud cover. Several days may pass without a temperature observation. Therefore, to estimate land surface temperatures over the AirSWOT study domain, we temporally downscale the 1 km MODIS Land Surface Temperature Product. A high temporal resolution temperature product is created by analyzing the temporal variability of the temperature observations at the pixel level and estimating temperature based on an expected diurnal pattern, providing a set of 1 km temperature maps at 1-hour intervals. For more information on the temporal downscaling along with an example time series for a single pixel, see the supplement (Figure S2).

Having increased the spatial and temporal resolution of the moisture and temperature data for comparison with AirSWOT radar backscatter data, we examine sets of surface moisture, temperature, and Ka-band backscatter values at the pixel level. Irrespective of land cover or roughness-driven variations, the purpose of this examination is to identify backscatter sensitivity to moisture and temperature. A representative surface describing how near-nadir backscatter varies with moisture and temperature is estimated by subsetting the pixel-level data to less than 6° incidence. This yields a single, ensemble average surface representing different possible

combinations of available moisture, temperature, and backscatter data, containing 1,000 different surfaces generated by randomly sampling 25% of the data, with replacement, creating an interpolated surface on each iteration.

3.3.3 Influence of surface structural complexity on Ka-band surface scattering

Radar backscatter varies with surface dielectric constant (assessed here in the form of moisture and temperature) and geometry-roughness [Hallikainen et al. 1985; Hoen and Zebker 2000]. Because the incidence angles assessed in this study are less than 30°, scattering is dominated by reflections from appropriately oriented facets on the surface [Elachi and Van Zyl 2006]. In this case, leaves provide diverse orientations and the structure of the vegetated canopy provides a mixture of facets and gaps. Because LVIS LiDAR is full-waveform, it is able to capture signal returns of different strata within the vegetative canopy, providing information on vegetation density diversity and therefore canopy structure. The LVIS LiDAR complexity metric measures the vertical heterogeneity of surface features and is related to the leaf area index [Tang and Armston 2019]. These metrics are related to two-way transmissivity, as less LVIS LiDAR energy is returned from dense, highly complex canopies than from sparse canopies and bare ground with low complexity. While the complexity metric does not directly provide any information regarding the orientation of the surface facets, leaves with horizontal rather than vertical orientations are more exposed to LiDAR pulses, which may have greater contributions to the assessment of counts per elevation bin. Thus, the relationship between LiDAR complexity and Ka-band scattering is hypothesized to be indicative of the two-way transmissivity of Ka-band, assuming a uniform distribution of leaf and branch orientations.

3.3.4 Ka-band Phenomenology Scattering (KaPS) Model: A simple empirical statistical model to simulate near-nadir Ka-band surface scattering

To simulate how Ka-band scattering may vary over space and time, we develop a simple statistical scattering model based on near-nadir surface moisture, temperature, and LiDAR complexity to estimate backscatter (Figure 10). To develop the model, the relationships between scattering (y) and each of these three parameters (xi = moisture, temperature, or complexity) are investigated independently for binned backscatter values. It is important to note that the incidence angle range for this examination is limited to 4-6°. This investigation is conducted by subsetting the data into the 15 land cover types (LC) and correlating each of the three parameters with backscatter. The three parameters are examined separately to identify the strength of the relationship for each parameter alone; land covers are examined separately because various land covers are expected to have different scattering mechanisms due to differences explained by the three parameters. While there is a close relationship between moisture and temperature variations over land—particularly at high temperatures with enough energy to support rapid evaporation or in hot and dry climates with low antecedent moisture—this work seeks to identify individual contributions to backscatter at diurnal temporal scales over a temperate summer (averaging 10° C). Following investigation of the three scattering parameters, non-linear equations describing these relationships are used as the framework for the model. Three formulas (for each x_i = moisture, temperature, or roughness) are generated for each land cover type, estimated first using a loess local regression to reduce the influence of outliers prior to estimating the non-linear relationships.

For each land cover, observed backscatter values from pixels with incidence angle between 4 and 6° are binned into ~0.5 dB groups to extract the mean and standard deviation for each parameter, creating a look-up table of expected values for each backscatter bin. Next, scatterplots of these expected values are produced for each parameter, yielding non-linear regression equations for each land cover. While backscatter may be estimated using each of the equations separately, it is expected that the variable importance of each parameter will not be the same for each land cover type and therefore none of the three parameters should be used alone to estimate backscatter. A single equation for each land cover is produced with weighted contributions from each class. Weights are assessed to maximize the coefficient of determination (R2) when the weighted averaged estimates are compared with the binned observations. The direct output of the combined regression formulas is applicable to the reference incidence angle range 4-6°, but estimates of higher incidence backscattering can be produced by using the 4-6° reference value (as if the pixel were identified within the reference incidence range, even if that is not the case). The quantile scattering curves are used to estimate scattering at higher incidence angles. The starting reference backscatter value, identified by the regression formula, is used to select which of the quantile categorized scattering curves would best depict the higher incidence scattering. Finally, 2D density plots (backscatter vs. parameter, unbinned) are used to estimate the probability that the estimated value will occur. A secondary map depicting backscatter confidence may be produced alongside the backscatter map. Together, the pair comprise the Ka-band Phenomenology Scattering (KaPS) model.

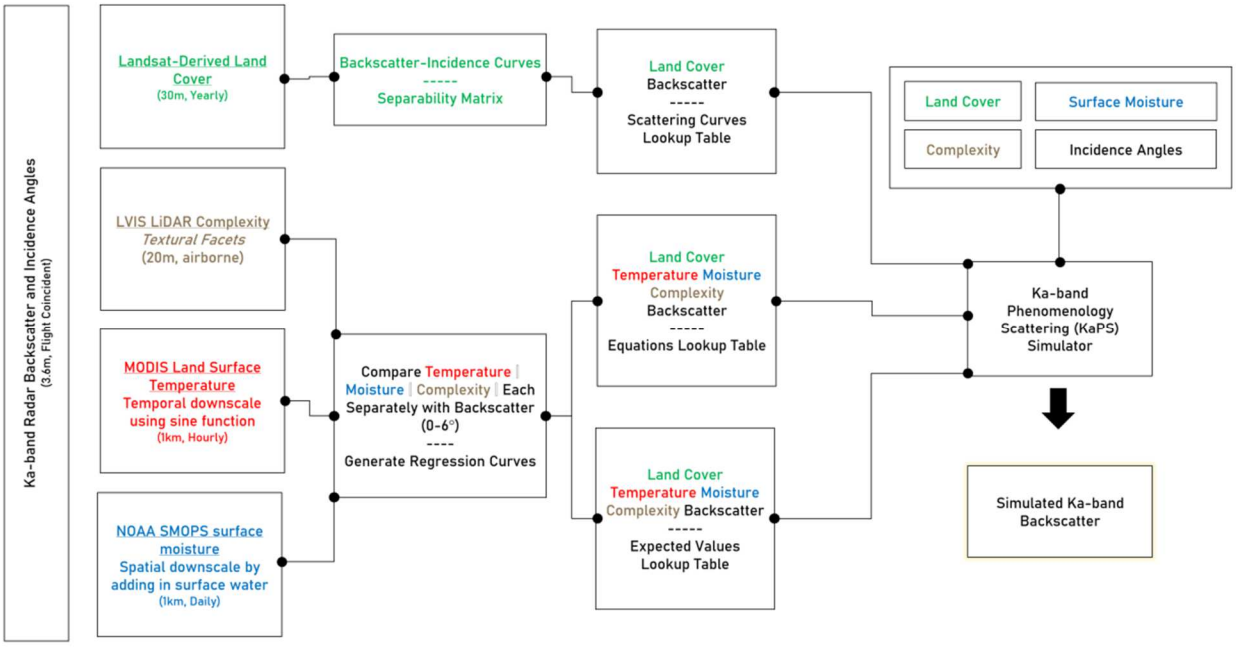

Figure 10. *Schematic diagram showing the stages of designing the Ka-band Phenomenology Scattering (KaPS) model (first four columns) and producing a simulation. Reference land cover (green), moisture (blue), temperature (red), and complexity (brown) data are preprocessed and compared with Ka-band radar backscatter to produce empirical scattering curves and look-up tables of parameter-backscatter relationships and expected values. The derived empirical scattering curves and look-up tables form the foundation of the KaPS Ka-band backscatter simulator.*

3.4 Results

3.4.1 Separability of near-nadir Ka-band SAR backscatter for wet surfaces and diverse land covers

Typically, open water and dry vegetation are easily and frequently distinguishable. Backscatter values extracted from the LSLC demonstrate the variation in scattering for different land cover types for incidence angles 2° to 27° (Figure 11). For dry land classes, average backscatter for incidence angles less than 5° is often very low (~0 dB), with a small standard

deviation across the 2° to 27° incidence range, compared to wetter surfaces. The open water class shows consistently high scattering at small incidence angles (~15 dB at 3°), and sharply decreasing backscatter with increasing incidence angles, as expected from the relatively specular scattering. The shallow-littoral zone of water bodies contains both water and emergent or floating vegetation, producing bright scattering as indicative of the smooth scattering source of the underlying water surface and perhaps some double-bounce scattering—observed as bright rings around some small lakes with reedy vegetation—between the vegetation and the water surface [van Zyl, 1989], with an average of about 7 dB at 3°. The barren land cover shows a brighter backscatter than vegetated dry land, averaging ~3 dB at 3°. Bright scattering from barren land surfaces is indicative of the variability in the land cover itself. While barren surfaces are not generally considered to be specular, they may be very flat, smooth, and angular, producing a near-specular scattering source, and they may also be wet, having similar scattering as the littoral zone vegetation or the open water in some cases.

For all observed dry-land cover classes, there are few bright pixels at small incidence angles (<5°). The low occurrence of bright scatterers for vegetated land cover classes demonstrates that it is uncommon for these classes to be very bright in these Ka-band near-nadir observations, limiting their impact. Additionally, anomalously high backscatter returns from the vegetated classes are likely to be caused by differences in resolution and misclassification, as a few bright scatterers classified as vegetation in the LSLC were observed to be small water bodies in the AirSWOT camera data. Additionally, pixels from other surface classes such as water or littoral zones may be included in the extraction of a different land cover class such as low shrub due to uncertainties in the land cover classification.

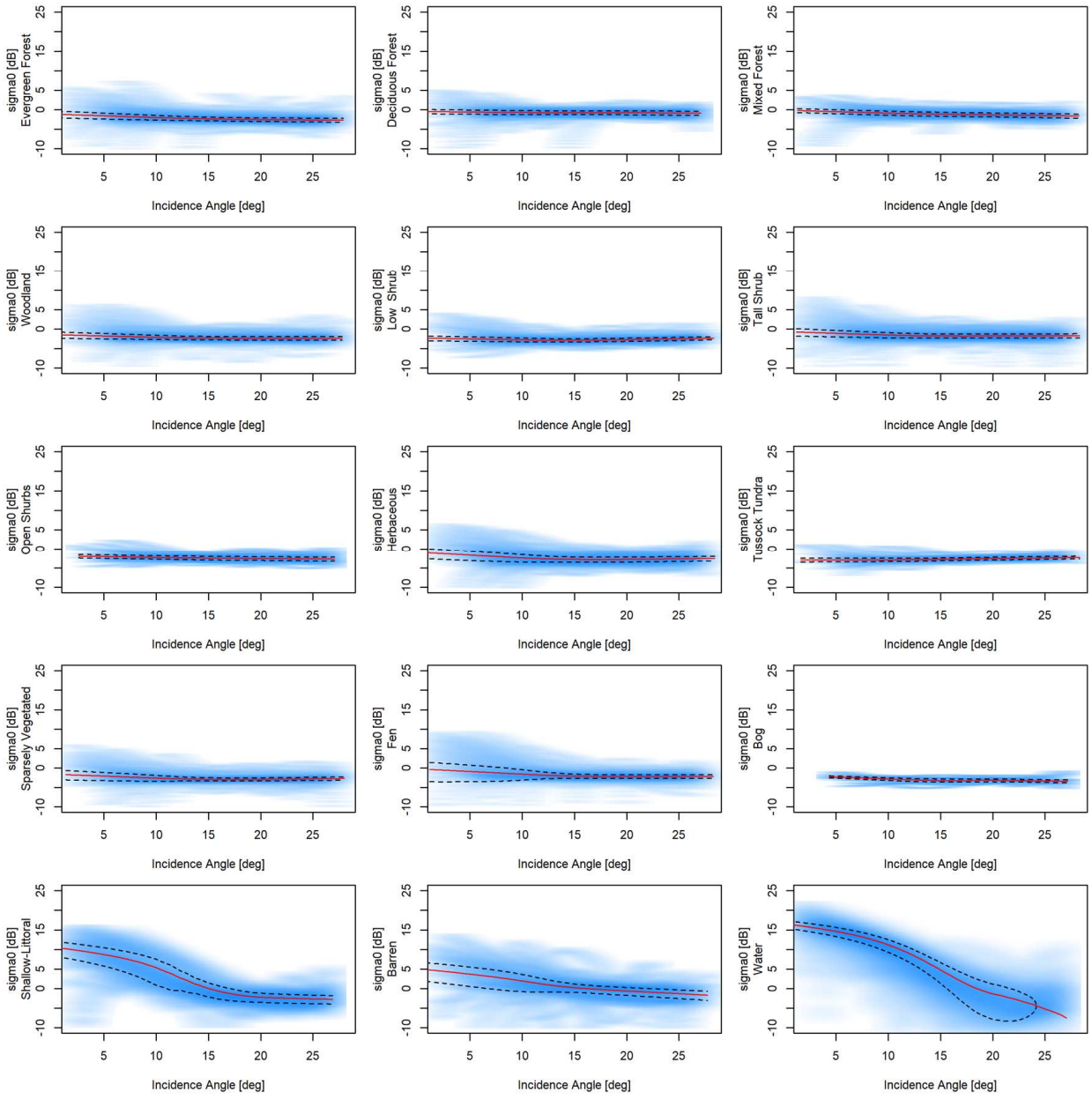

Figure 11. *Extracted Ka-band backscatter from 2017 AirSWOT 2017 flights acquired over the ABoVE domain. The red line shows average backscatter, while the black dotted lines present the 32nd and 68th percentiles around the average. The blue shading shows the 2D density of the observations, excluding outliers. The majority of land covers have low backscatter across all incidence angles, while wetter surfaces such as water and littoral zones have higher backscatter at lower incidence angles. The barren class shows a higher standard deviation, particularly at the near range, demonstrating more variability.*

We can visually observe that, especially at incidence angles around 5°, water differs from all of the vegetated land covers (Figure 11). However, the differences between water, littoral zone, and barren soils are smaller, though they are still distinguishable. By applying the separability metric [Cumming and Van Zyl 1989], we quantify to what extent the scattering is similar or separable for each land cover class and incidence angle (Figure 12).

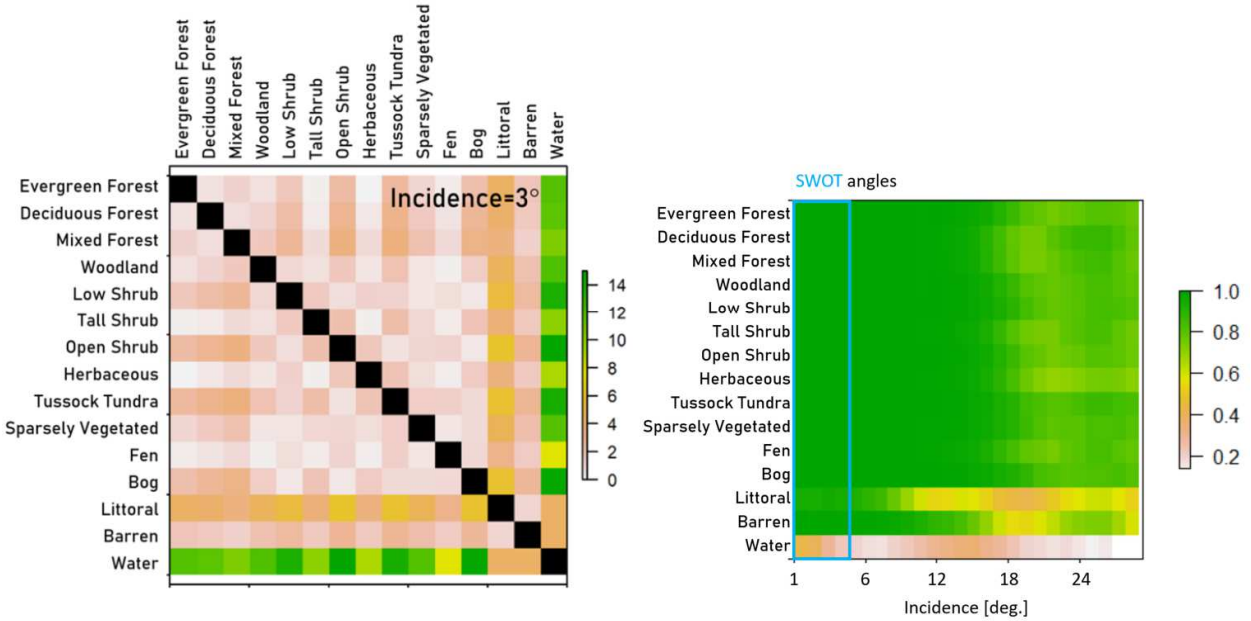

***Figure 12 Left**. The separability metric (Eq. 1) is calculated for each land cover class combination for the 0-3 degrees of incidence bin to determine the separability between each pair of land cover classes. Pairs of classes with values greater than 2 are considered separable. **Figure 12 Right**. The modified separability metric (Eq. 2) is applied to each land cover class in contrast to the open water class, along all incidence angles, to identify how separability changes as a function of incidence angle. Open water is shown to not be separable from itself as expected, and many land cover classes are shown to be consistently separable from water. For near-nadir SWOT-like incidence angles, and angles up to 15°, open water is considered to be highly separable and distinct from other classes.*

The separability matrices shown in Figure 12 demonstrate that open water is highly separable from most land cover classes from low SWOT-like incidence angles up to mid-range AirSWOT incidence angles

(~3≤12°). As separability values greater than 2 are considered highly separable or distinct classes [Baghdadi et al. 2001], the open water separability values of 5–15 compared with all other classes demonstrate that water is distinct. Excluding the littoral zone and barren classes, the separability of other land classes is even higher (8–15), demonstrating that open water has up to five times greater separability compared with vegetated land cover classes and is twice as separable as littoral and barren classes. Since the separability metric measures the distances between classes through the mean and standard deviation values, it is important to note that separability refers to only one standard deviation of observations and therefore represents the majority of cases but not all cases.

The majority of the time, open water, littoral zone, and barren surface classes are separable from each other, which is the ideal scenario for SWOT and for future applications of Ka-band data. However, under certain conditions, the differences between these three classes narrow, particularly when non-water classes exhibit higher than expected backscatter. These results are corroborated by similar studies looking at more coarse-resolution GPM data [Rodriguez et al. 2017; Lobry et al. 2019]. These findings suggest that it is additionally important to assess the influence of changing surface conditions, which may cause changes in backscatter.

3.4.2 Influence of surface moisture and temperature on Ka-band surface scattering

To assess the relationship between backscatter, surface temperature, and moisture, the surface temperature and moisture products were temporally and spatially downscaled to resolutions comparable with AirSWOT observations. The results of the downscaling for the temperature (as a time series), and moisture (as a map), are shown in Figure S1 and Figure S2, respectively, in the supplement.

To investigate how surface moisture and temperature contribute to changing near-nadir backscatter, these variables are plotted in 3-D space, irrespective of land cover type and limited to 0-6° incidence angles (Figure S3, see also Fayne and Smith, 2021). The resulting best-fit 3-D surface represents an ensemble average of all of the possible combinations of backscatter, moisture, and temperature and reduces the uncertainty provided by limited observations or anomalous data values. Surface moisture has a steep positive trend with backscatter, with end segments having shallower trend slopes at 0-20% and 50-100% moisture. As anticipated, temperature has a small, imprecise, and highly variable contribution to near-nadir Ka-band backscatter compared with surface moisture. Because of the weaker relationship between backscatter and temperature (Figure S3), temperature is not analyzed further; however, the stronger relationship between surface moisture and backscatter is examined in more detail.

The strong correlation between surface moisture and backscatter is shown in Figure 4. Using 0.5 dB backscatter bins, the mean and standard deviation moisture values are assessed for each bin and for each land cover. Bins are limited to incidence angles 4-6° to limit the incidence angle-related change in backscatter. Most land cover values have low moisture, as expected, with the exception of the three classes of interest: littoral zone, barren soils, and water. A polynomial regression curve (red curve) is drawn through the mean values for each of the land cover classes, producing backscatter-moisture relationships that are unique to each land cover.

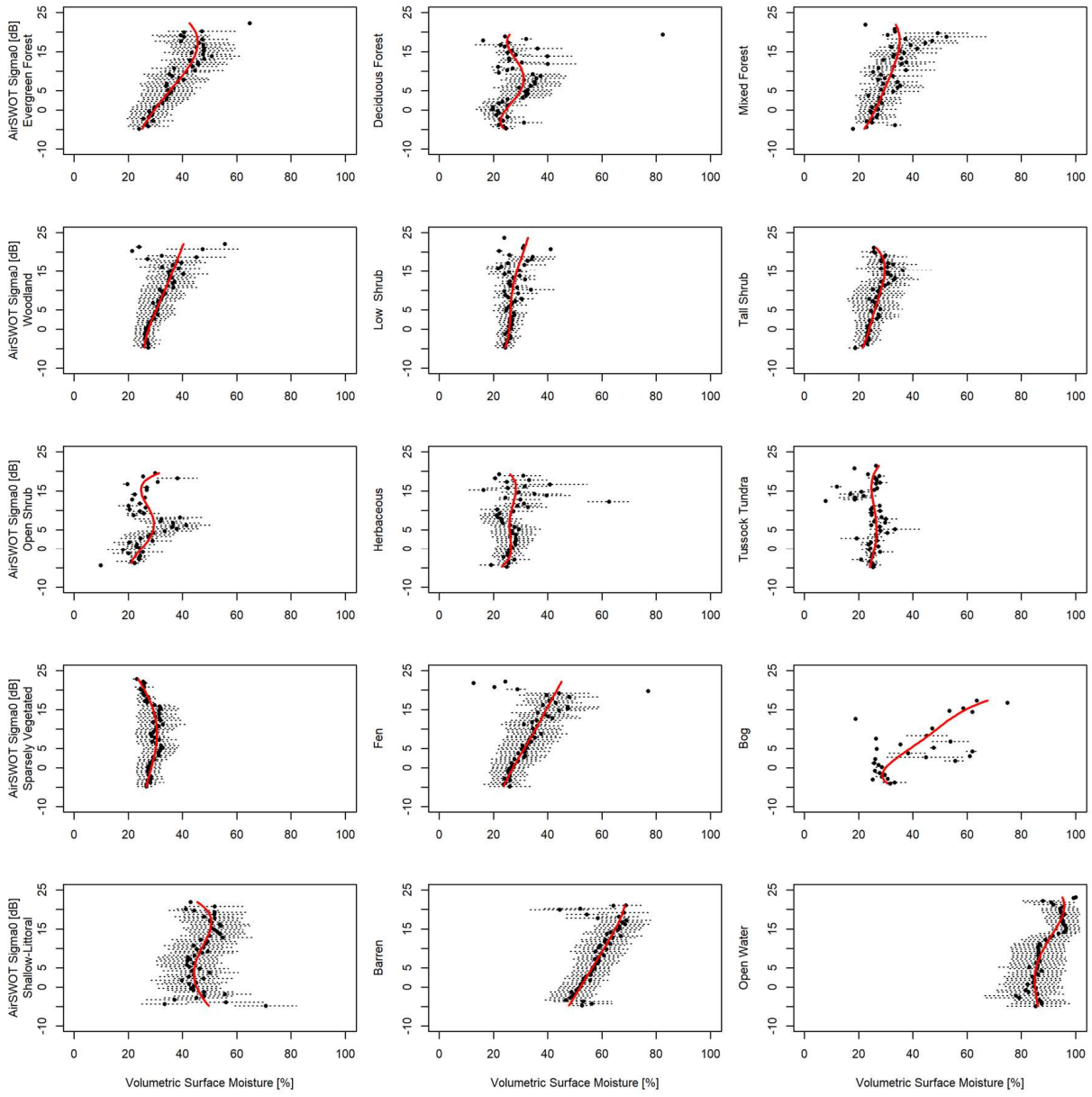

Figure 13. *Mean (black dots) and half-standard-deviation (horizontal lines) surface moisture values assessed for each 0.5 dB bin for each specific land cover, limited to 4-6° of incidence. Littoral zone, barren soils, and water have the highest surface moisture of the 15 classes. For each land class, a best-fit regression (red curve) yields an empirical backscatter-moisture relationship unique to each land cover.*

The variation between the moisture values of the land cover classes presented in Figure 13 can be explained as follows. The shallow water-littoral zone contains a mixture of vegetation and water; however, the surface moisture data is limited by the spatial resolution of the data and the artificial addition of moisture for wet areas such as open water bodies, which was not possible with the littoral zone. Thus, the mixture of water and vegetation would provide an expected observed surface moisture value ranging between 30-50%. The barren surface classification sometimes consists of exposed soils of rivers and lake beds on the edge of water bodies. Across the ABoVE domain, where the land cover data was produced, there is also an abundance of exposed rock and bedrock, particularly closer to the Canadian Shield in the east. However, the areas that we examined rarely include these rocky surfaces, and therefore dry, barren surfaces are less frequent in this analysis compared to near-water soils or exposed lakebeds, leading to a wetter moisture range of 40-65%. Finally, open water has a range of 80-100% moisture, explainable by the differences in spatial resolutions between the LSLC, surface moisture, and radar data products. The large standard deviations of moisture within each bin and high slopes of the fit lines suggest that the accuracy of the estimate from moisture alone is limited.

While the regression curves are designed to show the expected backscatter value given a specific surface moisture value based on the trend, any specific combination of moisture and backscatter may or may not be statistically likely to occur. For example, we previously noted that some mixed water pixels would have a lower moisture value and less backscatter. It is additionally good to know what the expected backscatter would be when pixels are mixed, however, across the observations, mixed water pixels are not particularly likely. Figure 14 shows the un-binned observations as a 2-D density plot highlighting the backscatter-moisture pairs that are particularly likely.

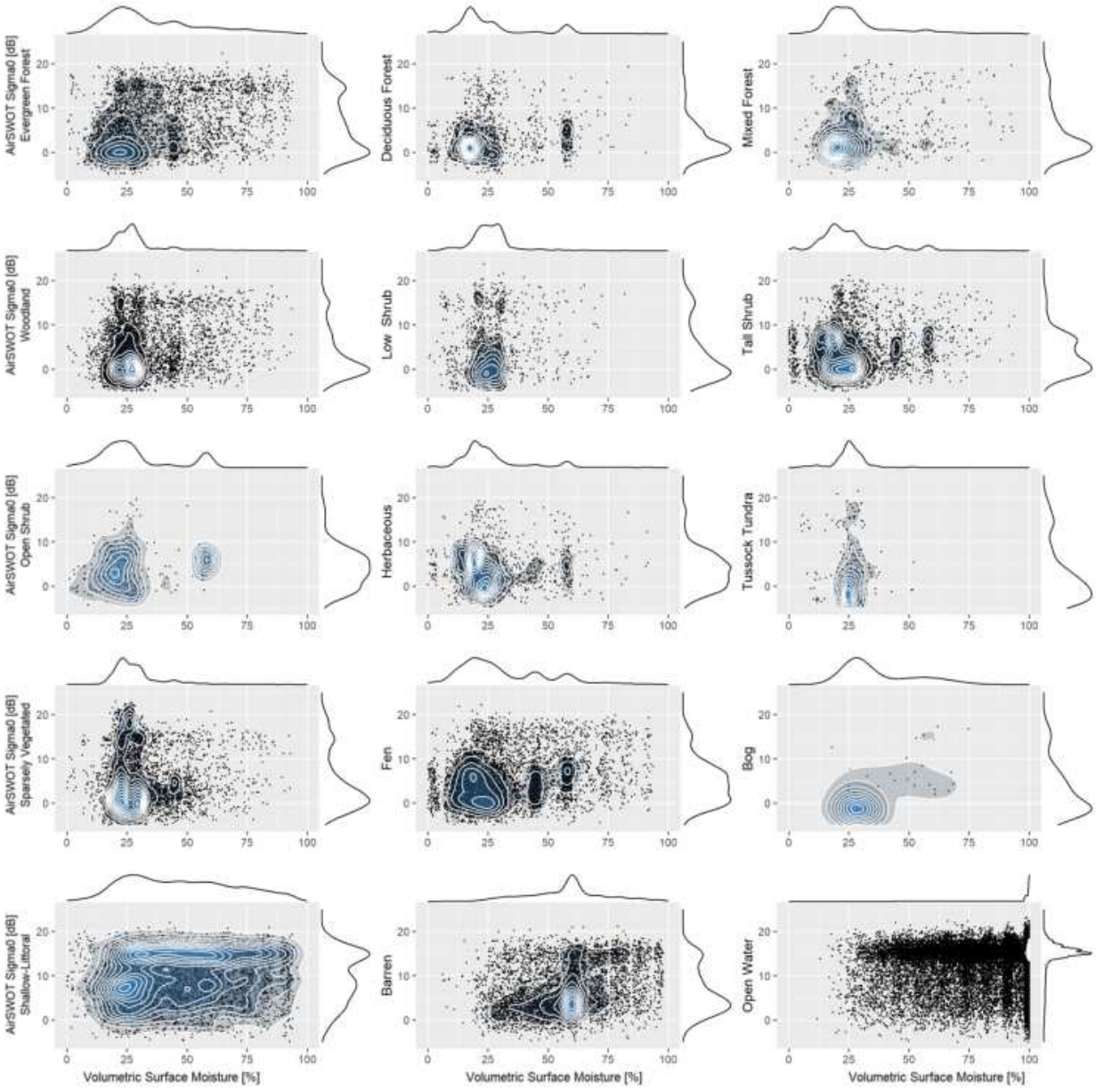

Figure 14. *A scatterplot of the backscatter- moisture observations are shown for each land cover type, different from the binned plots above, for incidence angles 4-6°. Blue contours show dense clusters of points, supported by probability density lines on the x and y axes, revealing probable scattering values. These figures demonstrate the likelihood that a given backscatter value or moisture value would be observed, given the seasonal observation range of July-August 2017.*

As previously mentioned, the open water class may become mixed water along edges of channels and lakes, lowering the scattering value, although this is not particularly likely for areas that are classified as open water. However, the littoral zone, which is a transition between open lake water and land, represents a very large range of expected moisture values, which also explains why the alignment of the mean values from this class represented in Figure 13 is vertical. The littoral zone cover class shows that backscatter can be high even when the ground is not particularly wet, supporting the idea of mixed pixels and an imprecise moisture reference, and additionally raises the idea of backscatter variability based on surface texture and geometry at different vertical scales. Unlike dense forest types, the littoral zone contains thin, non-woody vegetation that would allow Ka-band penetration or transmission, producing backscatter from different heights, varying vertically up to three meters. Moisture variability cannot fully describe the variability of the Ka-band backscatter, possibly due to the surface complexities over varying vegetation types. To begin to answer these questions, we next look at surface structural complexity through the lens of coincident LiDAR measurements.

3.4.3 Influence of surface structural complexity on Ka-band surface scattering

Full-waveform LiDAR data from the Land Vegetation and Ice Sensor (LVIS) provide information on surface and vegetation structure. Low complexity values (close to 0) are usually flat ground or water surfaces, while higher complexity values (close to 1) are usually dense canopies. In practice, for this region, complexity values rarely exceed 0.6, with the exception of infrequent measurement errors, easily recognizable as a stripe through the center of the flight

segment. These errors appear to be more apparent over water bodies, and so for the purposes of this analysis, all complexity values greater than 0.6 are omitted.

Using the same method of comparison as with the moisture data, backscatter values are binned into 0.5 dB groups (y axis) and the average and half-standard deviation of the LVIS complexity values are plotted on the x axis. All land cover classes have at least some observations of low complexity, due to land cover variability, misclassification, and diverse densities of land covers. Only forest and shrub vegetation types have higher complexity values. Forest and shrub vegetation classes show higher backscatter in low complexity areas and relatively lower backscatter when complexity increases. Because complexity is a measure of vertical structure and density, the decreased backscatter signal is indicative of the decreasing radar and LiDAR transmittance through thicker canopies, producing "L" and "C" –shaped backscatter-complexity relationships. However, it is important to note that the shapes are not uniform across the different land cover types. This is important because it indicates that the Ka-band backscatter is sensitive not just to surface complexities, but also to foliage type, as the Evergreen Forest and Deciduous Forest classes have very different scattering curves, as an example.

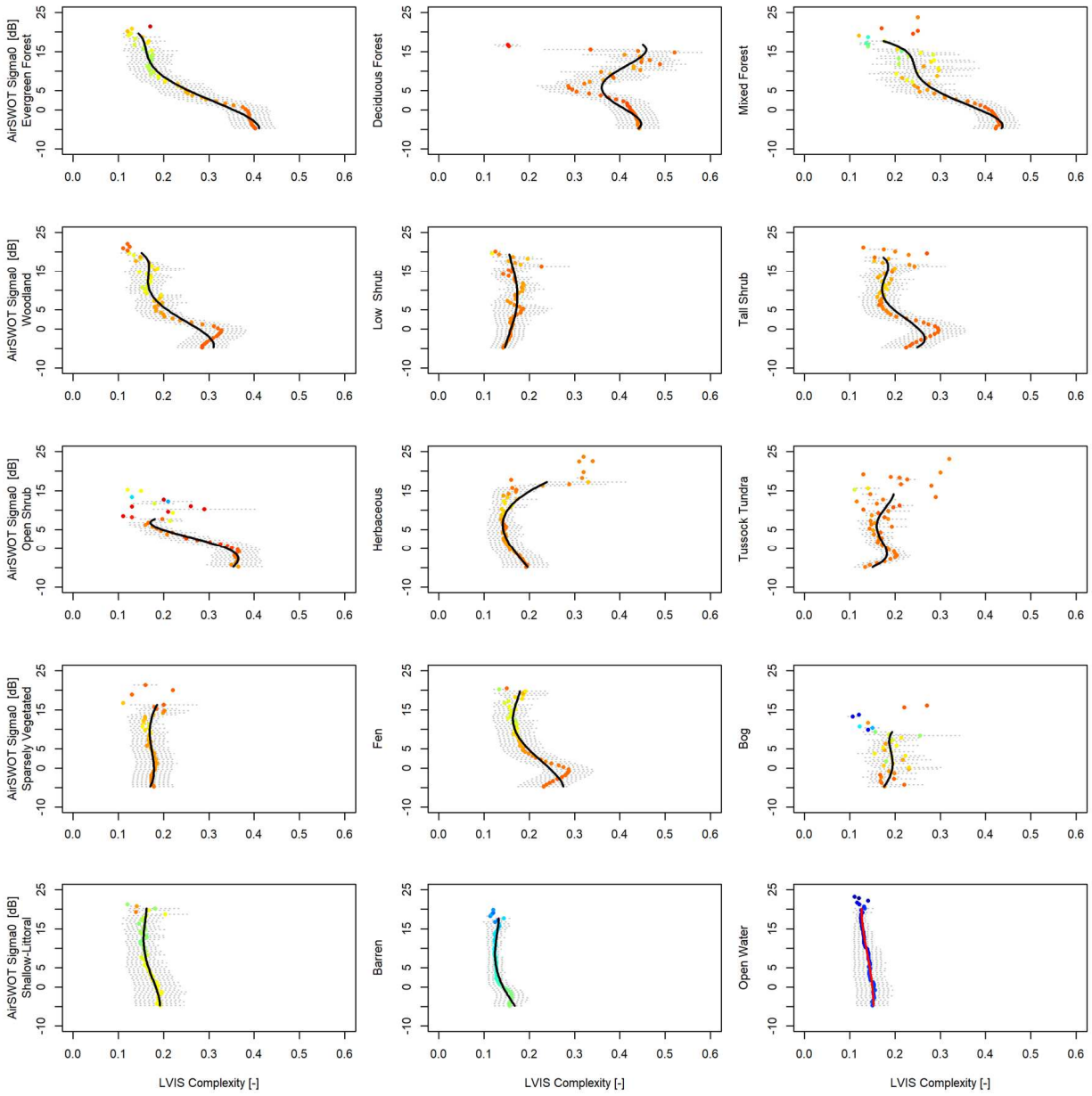

Figure 15. *Mean (dots) and half-standard-deviation (horizontal lines) LVIS LiDAR complexity values assessed for each 0.5 dB bin for each specific land cover, limited to 4-6° of incidence. Colored dots represent moisture where blue dots are very wet and red dots are very dry. Forest and shrub vegetation classes show a decreasing trend of backscatter with increasing complexity, whereas other land cover classes, such as water are limited in their complexity variability. For each land class, a best-fit regression (black curve) yields an empirical backscatter-complexity relationship for that class.*

Though the data in Figure 15 represents the scattering relationship between LiDAR complexity and Ka-band backscatter using backscatter bins, very low backscatter values in the case of water, and very high backscatter values in the case of dry land, are not particularly common. The purpose of Figure 15 (and Figure 13) is to demonstrate the contributions of backscatter variability if a given backscatter value is observed. Figure 16 demonstrates the probability that a land cover type will have a high or low complexity value.

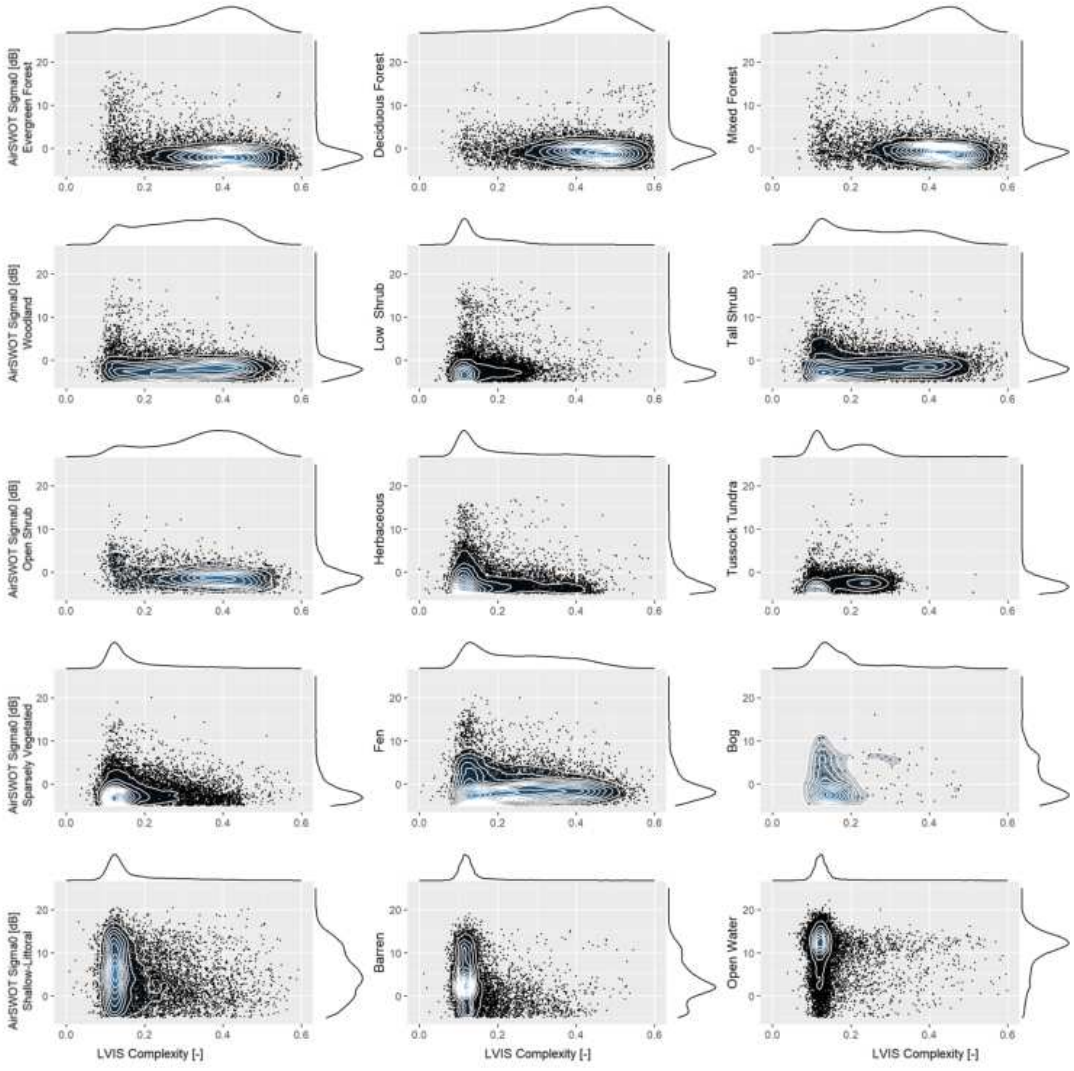

Figure 16. *A scatterplot of the backscatter- LVIS LiDAR complexity observations are shown for each land cover type, different from the binned plots above, for incidence angles 4-6°. Blue contours show dense clusters of points, supported by probability density lines on the x and y axes,*

revealing probable scattering values. These figures demonstrate the likelihood that a given backscatter value or complexity value would be observed, given the observations from July 2017.

Using the frequency distributions and backscatter-complexity relationships (Figures 15 and 16), we estimate likely backscatter values over dry land. When we combine our complexity-based estimates with our moisture-based estimates, we can start to account for dominant factors in scattering variability across the landscape. By building a simple model, we can produce simulations of backscatter that are sensitive to changes in moisture and surface complexities, as described next.

3.4.4. Ka-band Phenomenology Scattering (KaPS) model: A simple empirical statistical model to simulate near-nadir Ka-band surface scattering

We introduce a simple empirical statistical model for near-nadir Ka-band surface scattering, called Ka-band Phenomenology Scattering (KaPS), to demonstrate likely variations in surface scattering due to diverse and changing moisture conditions and land covers. The KaPS model combines the two output backscatter estimates from the complexity-backscatter and moisture-backscatter equations. When both data sources—moisture and complexity—are available, the data can be input directly into the model. When data is unavailable, a look-up table, supported by frequency distributions (Figures 14 and 16) can be used to estimate likely values based on land cover type. KaPS initially produces a backscatter estimate for a given pixel based on the moisture and complexity values. The backscatter values from each equation are combined using an iterative weighting technique to maximize the R^2 when compared against the true, binned AirSWOT data. These values are only applicable for the reference incidence range (4-6 degrees);

these values are acceptable for that specific range, and can be used as a reference for higher incidence angle pixels. Using quantile curves extracted from the backscatter incidence angle relationships, we can estimate for each land cover which of the quantile curves (4-6 degree portion) best fits the reference backscatter value identified by the two equations, producing a map of backscatter values extending to 27°. For the 4-6 degree incidence angle range, Figure 17 demonstrates the relationship between the estimated backscatter values produced from KaPS, and the original binned backscatter values from AirSWOT. The mean and median R^2 from the KaPS and AirSWOT comparison 'best case' across the 15 surfaces are 0.75 and 0.76, respectively, demonstrating that the majority of the backscatter variability is captured by moisture and LiDAR complexity, while the remainder of the variability is likely due to finer, wavelength-scale (~1 mm, a fraction of the 8mm wavelength) roughness features, which are not examined in this study.

Three look-up tables are used to simulate backscatter:

1) Formulas with weights for the LiDAR complexity and moisture components and the resultant 'best case' R2 value (see Table S2), and
2) Expected values and probabilities for moisture, LiDAR complexity, and backscatter as seen in Figures 13-16 (see Table S3).
3) Incidence Angle -- Backscatter Quantile Curves (Figure 11; see also Table S1).

To simulate the backscatter from a given surface, either surface complexity, surface moisture, or both are required as inputs alongside a map of incidence angles for the coverage area. Given input reference data and an incidence angle map (as in the example shown in Figure 9), the

workflow is as follows. If both complexity and moisture datasets are available, the near range (4-6°) reference backscatter values may be computed directly. If one or the other dataset is unavailable, the available data value for each pixel can be used as a starting point in the Expected Values lookup table (S3), pointing to the likely value for the other dataset. Given the observed value from one dataset, and an estimated value selected from the lookup table, the values can be input directly into their corresponding equations. Finally, if neither value is known, KaPS can be used to test the mapped backscatter response to changes in surface complexity and moisture.

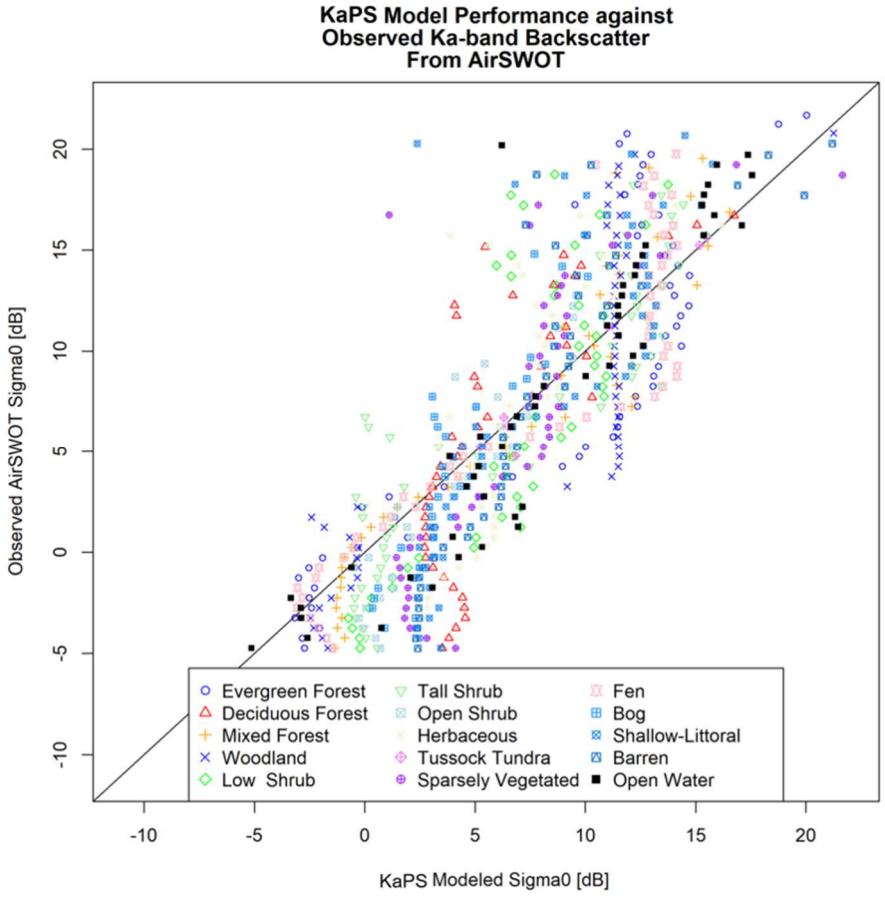

Figure 17. *Binned backscatter observations from AirSWOT versus simulated or 'expected' values from KaPS. Backscatter values are simulated for each land cover independently based on AirSWOT-derived empirical relationships between moisture, surface complexity, and backscatter. These estimated values represent a 'best case scenario' for how closely the data can be estimated.*

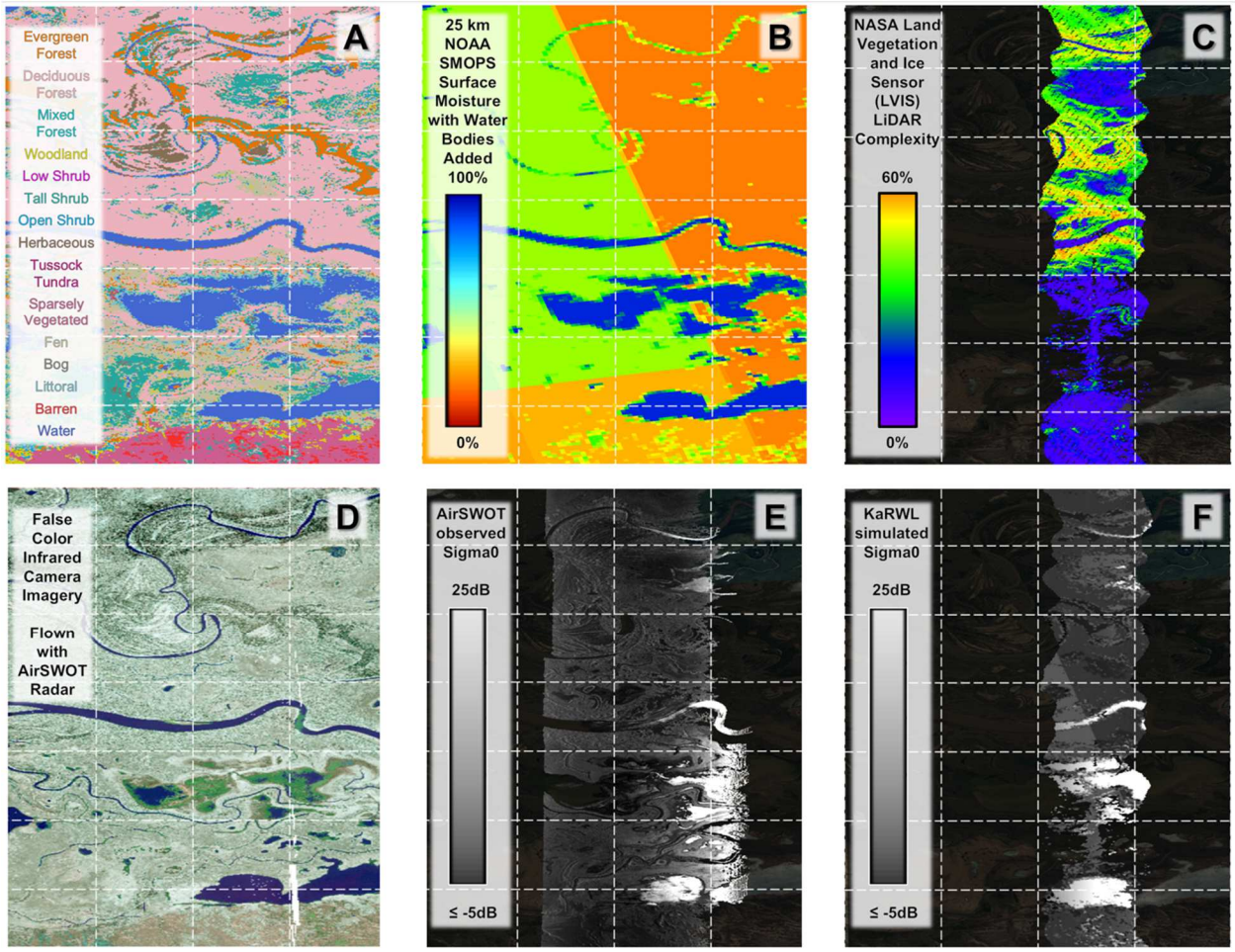

Figure 18. *Reference data and KaPS model simulation output for a transect through the Peace Athabasca Delta (PAD) region, located in Canada (approximately 58.369N, 111.347W) with (A) Landsat-derived land cover (Wang et al., 2019), (B) NOAA SMOPS surface moisture, modified for this study, (C) NASA LVIS LiDAR Complexity, (D) False Color Infrared Image, collected simultaneously from the same aircraft as the AirSWOT Radar observations,(E) AirSWOT Ka-band backscatter, and (F) KaPS model simulation developed in this study. Note that the simulated backscatter (F) shows a diagonal line of brighter scattering in the center of the flight line as a result of increased moisture; the near-saturated moisture for that area is shown as a large green tile in the reference NOAA SMOPS data. As the KaPS model relies on the input data extents, the output KaPS simulation takes on the same irregular zig-zag shape of the LVIS LiDAR complexity image and does not cover the full AirSWOT swath. If KaPS is applied to an area with a wider LiDAR extent (matching AirSWOT), the output would have more similar coverage to the original AirSWOT data.*

KaPS demonstrates possible radar backscattering values for wet and dry earth surfaces. KaPS simulations show good visual agreement with water bodies, wet vegetation, and soils as compared with AirSWOT observed Ka-band radar backscatter data (Figure 17 and 18). KaPS additionally highlights the sensitivity of radar backscatter to surface moisture, as the increased moisture jump from the low-resolution 25 km SMOPS tile, from ~30 to 60% moisture, results in a dramatic increase in radar backscatter (Figure 18). Soil moisture is generally accepted to be saturated at around 50-60%, which is also evidenced in the moisture-temperature-backscatter surface (Figure S3), where backscatter increases with increasing moisture until the surface is saturated. KaPS model output in Figure 18F demonstrates this sensitivity as brighter backscatter cutting diagonally across the center of the flight line, corresponding to higher moisture from the reference data. Following the available data from the reference products, because the LVIS data have an irregular shape and a narrower swath width (~1.8 km) compared to the AirSWOT data (~3.2 km), the output KaPS simulation is limited to the same swath width as the LVIS reference.

The KaPS model can be applied to any region having reference land cover and moisture datasets. As its purpose is to approximate near-nadir Ka-band backscatter, either modeled or remotely sensed data products may be used as inputs. Additionally, moisture, surface structural complexity, and land cover may be varied within the model itself, or by simply using different input data. The primary purpose is to be able to map water and land surface backscatter dynamics due to transient events (like moisture), with the expectation that relatively stable spatial differences due to heterogeneous surface complexity should be considered in order to assess the transient state of the surface. As observations of Ka-band backscatter are limited in temporal and spatial coverage, KaPS provides a method for creating simulated images of unobserved surfaces and

estimating backscatter changes for those surfaces by including dynamic parameters such as surface complexity and moisture. Further, KaPS has the potential to be used for inverse problems, as the Ka-Band Radar Water Likelihood (KaRWL) or 'KaRWL mode', where backscatter values can be used to assess vegetation characteristics and surface moisture variability, although more work is necessary to demonstrate and prove the validity of the inverse case.

3.5 Discussion and Conclusion

We determine near-nadir Ka-band scattering sensitivities for diverse Arctic-Boreal land and water surfaces by segmenting NASA ABoVE AirSWOT observations by land cover and comparing observed backscatter values to remotely sensed moisture, temperature, and roughness. Following this analysis, we are able to produce a statistical scattering model, Ka-band Phenomenology Scattering (KaPS), to simulate Ka-band surface scattering at near-nadir incidence angles for diverse land cover and moisture conditions.

This research quantifies observed Ka-band backscatter from wet soils considering both vegetation vertical complexity and moisture content. Moisture, a dominant component of the dielectric constant, is a well-known control on radar backscatter [Hallikainen et al. 1985], although this has not been studied as extensively for higher frequencies including Ka band. In addition, the specularity or roughness of various features has not been well studied for Ka-band backscatter from various terrestrial surface types, further limiting our knowledge about the occurrence of brightly scattering, non-water features. To gain insight on land surface variations through the perspective of the Ka-band frequency, airborne Ka-band observations are used to identify backscatter sensitivities to variations in land cover, moisture, temperature, and roughness.

Ka-band radar backscatter-incidence angle curves from AirSWOT outer-swath data (Figure 11) demonstrate clear separation between water surfaces and dry vegetation. Using the separability metric [Cumming & Van Zyl, 1989; Baghdadi et al., 2001], open water is determined to be 'highly separable' from other classes, with separability values up to five times greater than the minimum separability versus dry land classes. Importantly, surfaces that are spatially proximal to water, such as barren soils (often sandbars and river and lake edges in this study) and littoral zone vegetation, are clearly distinguishable from open water in most cases. Compared to these classes, water separability is up to two times greater than the minimum value necessary to consider groups distinct (Figure 12). However, it remains possible for barren soils and littoral zone vegetation to produce backscatter values similar to open water, making up the remainder of cases where water, barren soil, and littoral zone vegetation could not be separated with backscatter values alone. Using the modified separability metric observations of barren soil/sand bars, and littoral zone vegetation are found to be confused with open water about 5% of the time.

When the downscaled moisture and temperature are assessed alongside airborne Ka-band backscatter from AirSWOT, the sensitivity of backscatter to temperature is confirmed to be negligible or uncertain at best, given the scales of the available MODIS data and relatively small sub-seasonal temperature gradient. The transition between frozen and non-frozen ground would result in significant change in scattering due to the phase change of water [Jackson 1987], although no such transitions have been observed. Because all of the ABoVE AirSWOT observations used in this study are during the summer, there were no observations of a frozen ground surface, when the impacts of temperature would have been more significant for backscatter. The observed backscatter is strongly dependent on moisture as evidenced by the high moisture variability across the spatial domain and the seasonal water level dynamics. Without distinguishing between land

cover types, the highest backscatter values occur when moisture is greater than 50%. When the moisture-backscatter relationship is examined for each land cover, the positive relationship remains; although most land covers are not coincident with high moisture, backscatter nevertheless increases with increasing moisture. Considering moisture was only added to produce water bodies in the surface moisture data, moisture values 0-50 are primarily or entirely from the original SMOPS soil moisture product. Investigating the backscatter vs moisture confirms that this trend is still observable from some land cover class observations that are not in close proximity to open water. We demonstrate the utility of the LVIS LiDAR complexity, which is a measure of the vertical heterogeneity of a vegetative canopy, for separating dielectrically similar features such as saturated soils, emergent vegetation, and open water. The relationship pairing complexity with backscatter appears to vary significantly by land cover, providing more interesting lines of future inquiry. The shapes of the backscatter-complexity relationship are possibly due to differences between two-way transmissivity for different vegetation types and foliage orientations.

Because of the low complexity of water compared with vertical vegetation, and because water is always fully saturated, moisture and surface complexity data are not very helpful for studying backscatter from open water. Instead, water is fairly self-consistent as indicated by the separability metric, suggesting that the incidence angle curve is sufficient to explain most water dynamics, assuming the water observation is not a mixed pixel.

Combining observed LiDAR surface complexity with surface moisture and reference land cover datasets provides a framework for a simple empirical scattering model, the Ka-band Phenomenology Scattering (KaPS), capable of simulating Ka-band backscatter returns from water and land surfaces, with implications for being used for inverse problems, called the Ka-band Radar Wet-land Likelihood (KaRWL) model, to estimate moisture and surface complexity (vegetation

types) from Ka-band backscatter. The majority of observed variations in the AirSWOT backscatter data can be reproduced using the KaPS model, as evidenced by the mean and median R^2 values of 0.75 and 0.76 in a 'best case' or a 'matching observations' scenario (Figure 17). Figure 17 also shows that the worse performing land covers have mean absolute errors no greater than ~3 dB, which is similar to the GO model used by Fatras et al. [2016] for soil-only land covers at incidence angles less than 7°. This work additionally stands out as achieving this error range while including very diverse surface types, from open water, to exposed soils, and dense foliage. The purpose of the model is to map how backscatter changes as a result of changing surface conditions, meaning the model is not expected to resemble the observations exactly, but should reflect the input reference data, as seen in Figure 189F. The model is highly sensitive to the input data, as desired, showing a tonally rough surface matching the complexities of the input data.

There are several limitations of this analysis, including: 1) Because the Ka-band AirSWOT data examined in this study primarily observed Arctic-Boreal wetland regions, the distribution of scattering coefficients, particularly those found in Figure 2,may be skewed to reflect wetter regions. To counter this effect and to understand how the scattering values may depart from those observed, we describe how scattering varies over similar yet drier, surfaces, and develop a simple model to simulate Ka-band radar backscatter to estimate the appearance of wetter and drier areas. 2) The expected moisture values underpinning the KaPS model are much coarser than ideal for this study. While this issue was addressed by adding in surface water features to give a larger range of moisture variability and higher resolution wet-dry transitions, variations across non-water surfaces remain limited to the scale of the original 25 km SMOPS resolution, so the dynamic range of moisture for non-land features is likely to be under-sampled as a result. 3) The MODIS surface temperature data suffered from issues of low internal consistency and sometimes unrealistic and

extreme temperature values, making the diurnal amplitudes difficult to estimate correctly. As a result, the influence of temperature variability on backscatter had higher uncertainty than is ideal for assessing significant trends. Despite inconsistencies in the temperature data, it is generally not expected that the observed temperature range would contribute significantly.

This research reveals that, under moderately wet, summertime conditions, 1) the mean backscatter from open water, emergent aquatic vegetation, wet soils, and land vegetation classes vary by at least one standard deviation, making them all highly separable, with likely confusion with water occurring about 5% of the time, and 2) a simple model for near-nadir Ka-band scattering can be used to simulate changes to natural surface complexity and dielectric constant (as complexity and surface moisture) under non-frozen conditions. Barren soils and aquatic vegetative features may have similar or identical backscatter values as open water, depending on the roughness and moisture of each surface. Since moisture is a primary component of the dielectric constant and therefore backscatter, it is not surprising to find that exposed soils may begin to resemble open water when the surface is nearly or completely saturated. We confirm this expectation for near-nadir Ka-band radar by examining the effects of moisture and roughness variability, and developing Ka-band Phenomenology Scattering (KaPS), a simple empirical statistical model to simulate near-nadir Ka-band surface scattering. The performance of KaPS is similar to that of a previous GO modeling study [Fatras et al., 2016], while including more diverse surface covers and higher incidence angles, up to 27°. Future applications for KaPS and KaRWL include further investigations of skin-surface moisture and complex surface impacts on Ka-band backscatter returns for terrestrial ecology and hydrology studies, and increased confidence in AirSWOT and SWOT surface classification accuracies and water surface elevation retrievals.

3.6 Supplement

3.6.1 Figure S1: SMOPS Soil Moisture Downscaling

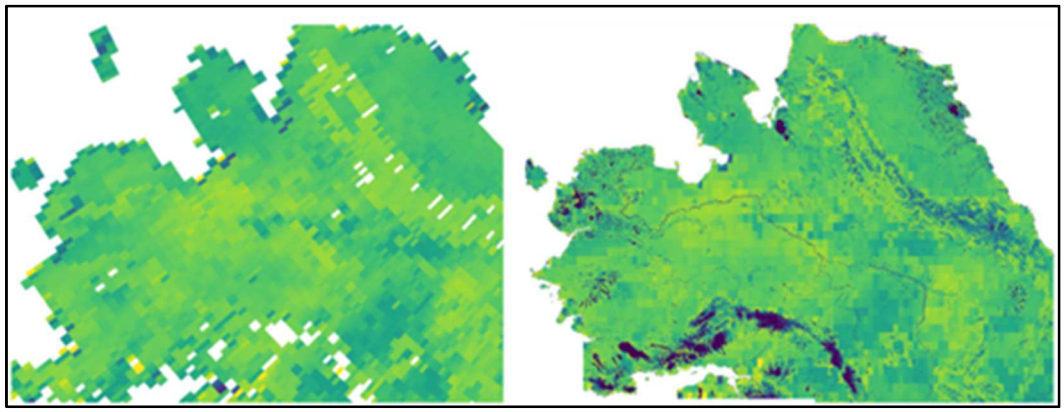

Daily NOAA SMOPS soil moisture data are spatially downscaled by adding reference water features from the Landsat-derived Annual Dominant Land Cover product (LSLC). ***On the left,*** is a map of the NOAA SMOPS 25 km soil moisture product covering parts of Alaska and Canada; ***on the right*** is the 1km downscaled data including water bodies produced in this study. The SMOPS data are nearest-neighbor-resampled to 30 meters to match the LSLC, and the resampled SMOPS pixels corresponding to LSLC open water class are re-assigned values of 100% moisture. Finally, the 30-meter resampled and waterbody-added moisture data is aggregated to 1 km to increase computation speed for analysis. An additional 90-meter product was developed for finer-detailed analysis and testing as the AirSWOT swath width is approximately 4 km. This process produces products that visually show both the original 25 km large pixel shapes and finer LSLC water bodies. *Note: Because the LSLC does not have a separate class for 'snow', snow-capped mountain ranges are labeled water as seen in the Alaska Range in the south and the Brooks Range in the north. None of the AirSWOT lines in this analysis include snow cover.*

3.6.2 Figure S2: MODIS Land Surface Temperature Downscaling

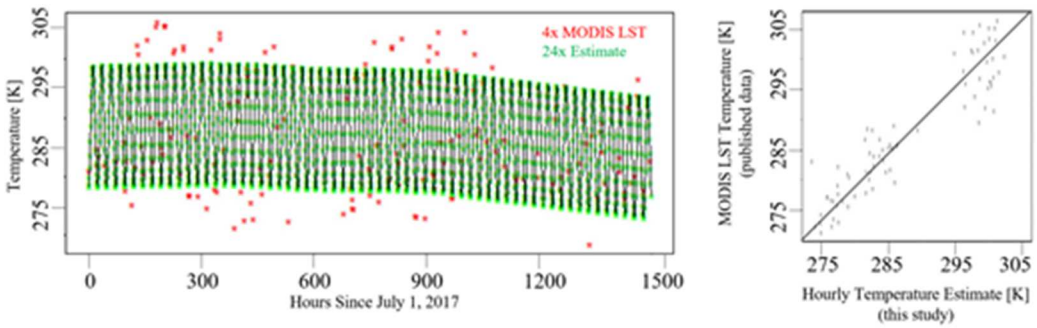

Daily MODIS Aqua and Terra Land Surface Temperature (MOD/MYD-11A1) data are temporally downscaled by fitting a sine curve to each 1km pixel to model the diurnal variation and fill in missing observations due to cloud cover for July and August 2017. The seasonal trend is first removed to isolate diurnal variability, then a sine curve is fit to the trend removed points by using a non-linear regression estimator, finally, the seasonal trend is added to the fitted sine curve. This figure shows how temperature is estimated for a single pixel over time. On the left, data from a single pixel location taken from day and night observations from MODIS Aqua and Terra are shown as red points; there may be up to four observations per day from these instruments, but data may be missing for several consecutive observations. Green points represent hourly estimated temperature. On the right, the hourly estimated temperature is compared with the MODIS temperature for overlapping hours. The scatterplot of points generally follows the 1:1 line, with an average variation of around 3° C, showing that the temperature estimate can be used when observations are not present, and is also better than selecting the temperature value nearest in time, as the nearest temperature value may be off by as much as 30° C.

3.6.3 Figure S3: Ensemble Average Surface Moisture, Temperature, and Ka-band Backscatter

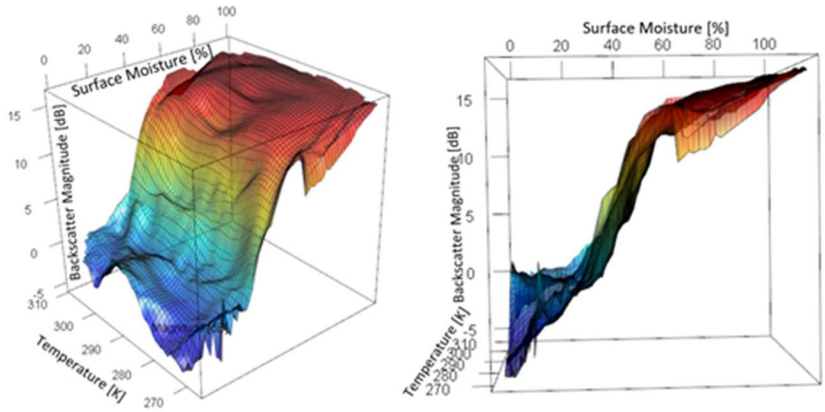

An ensemble average of surfaces representing moisture, temperature, and backscatter at incidence angles less than 6°. Instead of using all of the points as inputs to the surface, a random subset of

25% of the points are selected with replacement 1,000 times to create 1,000 surfaces and then averaged to produce a single surface representing different possible combinations of available data. This method of selection reduces the probability of sampling bias. The range of likely temperature values has a small, imprecise, and highly variable contribution to near-nadir Ka-band backscatter compared with the steep gradient and strong correlation seen with surface moisture.

3.6.4 Table S1: Incidence Angle Backscatter Curve Look-up Table

A subset of an example incidence angle backscatter curve look up table that is used to estimate the backscatter for the open water land cover class. The data is subset by incidence angle (the actual range is ~0- 27°). These values, and the values for other land covers, correspond to the percentile lines shown in Figure 2a in the main text. The Ka-band Phenomenology Scattering (KaPS) simulator uses percentile curves to simulate backscatter values beyond the 4-6 range that is estimated from the regression formulas shown in ***TS2***.

Backscatter Incidence Angle Curve (incidence angle limited subset) for the Water Land Cover Class			
Incidence Angle [θ, *degrees*]	Lower Bound [σ_0 dB] (32nd Percentile)	Mean [σ_0 dB]	Upper Bound [σ_0 dB] (68th Percentile)
0.334247	12.93341	15.08547	16.51797
2.539372	12.05942	14.42304	15.94506
3.526987	11.60328	14.08157	15.64961
4.25216	11.23964	13.81227	15.41691
4.86377	10.91243	13.57254	15.21016
5.386985	10.61647	13.35811	15.02564
5.928993	10.29311	13.12672	14.8271
6.301115	10.06054	12.96234	14.68647
6.734053	9.778361	12.76539	14.51852
7.112991	9.520427	12.58797	14.3678
7.483919	9.257312	12.40974	14.21702
7.875642	8.967125	12.21666	14.05447
8.219593	8.701021	12.04305	13.90913
8.565874	8.421079	11.86257	13.7582
8.918208	8.121226	11.66382	13.58859
9.222013	7.850358	11.47967	13.42875
9.526209	7.567808	11.28395	13.25677
9.795744	7.307969	11.10159	13.09507
10.087	7.016959	10.89574	12.91141
10.33765	6.757565	10.71194	12.74686
10.61132	6.463914	10.50509	12.5616
10.86778	6.177281	10.3064	12.38423
11.1143	5.889039	10.11207	12.2121
11.37498	5.566982	9.9044	12.03068
11.6112	5.25516	9.715745	11.86935

3.6.5 Table S2: Formulas with Weights for 'Best Case' Regression Fit

X	Land Cover	Weight	Equation
Moisture	Evergreen Forest	0.01	sigma= (4736.75) + (-688.88*x) + (39.25*x^2) + (-1.17*x^3) + (0.01*x^4) + (0*x^5)
Moisture	Deciduous Forest	0.62	sigma= (-4588.46) + (1010.97*x) + (-86.15*x^2) + (3.57*x^3) + (-0.07*x^4) + (0*x^5)
Moisture	Mixed Forest	0.54	sigma= (1188.48) + (-179.33*x) + (10.42*x^2) + (-0.29*x^3) + (0*x^4) + (0*x^5)
Moisture	Woodland	0.01	sigma= (13610.84) + (-2107.86*x) + (128.64*x^2) + (-3.87*x^3) + (0.06*x^4) + (0*x^5)
Moisture	Low Shrub	0.47	sigma= (14062.98) + (-1779.11*x) + (82.91*x^2) + (-1.66*x^3) + (0.01*x^4) + (0*x^5)
Moisture	Tall Shrub	0.96	sigma= (131052.81) + (-23515.83*x) + (1678.59*x^2) + (-59.6*x^3) + (1.05*x^4) + (-0.01*x^5)
Moisture	Open Shrub	0.41	sigma= (-209.48) + (40.67*x) + (-2.75*x^2) + (0.08*x^3) + (0*x^4) + (0*x^5)
Moisture	Herbaceous	0.53	sigma= (48615.05) + (-8092.93*x) + (535.71*x^2) + (-17.63*x^3) + (0.29*x^4) + (0*x^5)
Moisture	Tussock Tundra	0.99	sigma= (843690.05) + (-145111.72*x) + (9952.42*x^2) + (-340.14*x^3) + (5.79*x^4) + (-0.04*x^5)
Moisture	Sparsely Vegetated	0.6	sigma= (899228.13) + (-145952.06*x) + (9455.97*x^2) + (-305.7*x^3) + (4.93*x^4) + (-0.03*x^5)
Moisture	Fen	0.99	sigma= (-1183.52) + (176.25*x) + (-10.75*x^2) + (0.33*x^3) + (-0.01*x^4) + (0*x^5)
Moisture	Bog	0.54	sigma= (392.04) + (-35.3*x) + (1.22*x^2) + (-0.02*x^3) + (0*x^4) + (0*x^5)
Moisture	Shallow-Littoral	0.6	sigma= (-98568.79) + (10964.51*x) + (-483.82*x^2) + (10.59*x^3) + (-0.12*x^4) + (0*x^5)
Moisture	Barren	0.63	sigma= (358460.66) + (-3270.2*x) + (119.15*x^2) + (-2.17*x^3) + (0.02*x^4) + (0*x^5)
Moisture	Open Water	0.59	sigma= (-2152844.82) + (124903.5*x) + (-2896.25*x^2) + (33.55*x^3) + (-0.19*x^4) + (0*x^5)

X	Land Cover	Weight	Equation
Complexity	Evergreen Forest	0.99	sigma= (1205.19) + (-25586.88*x) + (215998.84*x^2) + (-892249.78*x^3) + (1794913.56*x^4) + (-1406302.05*x^5)
Complexity	Deciduous Forest	0.38	sigma= (-317.34) + (5972.14*x) + (-40106.12*x^2) + (127522.46*x^3) + (-195712.12*x^4) + (117088.18*x^5)
Complexity	Mixed Forest	0.46	sigma= (-309.96) + (6724.95*x) + (-52181.25*x^2) + (191965.38*x^3) + (-339337.8*x^4) + (231413.3*x^5)
Complexity	Woodland	0.99	sigma= (5458.21) + (-126345.13*x) + (1154119.93*x^2) + (-5182984.04*x^3) + (11434359.91*x^4) + (-9919201.86*x^5)
Complexity	Low Shrub	0.53	sigma= (141097.64) + (-4115223.06*x) + (47716493.42*x^2) + (-274992716.31*x^3) + (787802635.19*x^4) + (-897608964.69*x^5)
Complexity	Tall Shrub	0.04	sigma= (10676.15) + (-250470.39*x) + (2320409.34*x^2) + (-10600896.23*x^3) + (23891455.51*x^4) + (-21267620.32*x^5)
Complexity	Open Shrub	0.59	sigma= (714.79) + (-17202.22*x) + (164318.54*x^2) + (-765179.5*x^3) + (1727710.89*x^4) + (-1513302.79*x^5)
Complexity	Herbaceous	0.47	sigma= (-7404.47) + (186044.92*x) + (-1831765.26*x^2) + (8829553.73*x^3) + (-20820687.64*x^4) + (19221575.28*x^5)
Complexity	Tussock Tundra	0.01	sigma= (4173.81) + (-127184.21*x) + (1514596.22*x^2) + (-8809718.65*x^3) + (25042646.48*x^4) + (-27835274.63*x^5)
Complexity	Sparsely Vegetated	0.4	sigma= (10227.1) + (-483626.02*x) + (7921774.4*x^2) + (-59892344.07*x^3) + (214884616.95*x^4) + (-296986717.31*x^5)
Complexity	Fen	0.01	sigma= (8532.98) + (-212470.17*x) + (2096129.34*x^2) + (-10213961.78*x^3) + (24557554.82*x^4) + (-23306388.47*x^5)
Complexity	Bog	0.46	sigma= (-18991.35) + (616549.27*x) + (-7940828.6*x^2) + (50737680.85*x^3) + (-160834884.79*x^4) + (202342333.3*x^5)
Complexity	Shallow-Littoral	0.4	sigma= (72618.82) + (-2195097.73*x) + (26363580.55*x^2) + (-157154110.21*x^3) + (464756908.14*x^4) + (-545305819.32*x^5)
Complexity	Barren	0.37	sigma= (-6047.77) + (173577.02*x) + (-1952119.11*x^2) + (10739797.52*x^3) + (-28852309.18*x^4) + (30274912.87*x^5)
Complexity	Open Water	0.41	sigma= (4940271.26) + (-177334772.58*x) + (2543242436.96*x^2) + (-18217388409.99*x^3) + (65170712478.93*x^4) + (-93153334641.13*x^5)

Formulas with weights for the complexity and moisture components. When the estimated backscatter values calculated for the moisture-only and complexity-only equations are combined using a weighted average, the 'best case' r^2 value has a wide range, with median value of 0.76.

Land Cover	R2 when Combined	MAE
Evergreen Forest	0.750604177	3.156089575
Deciduous Forest	0.557277536	3.408872956
Mixed Forest	0.883529894	1.864137552
Woodland	0.696861916	3.291518004
Low Shrub	0.626726162	3.705522587
Tall Shrub	0.803786872	2.475156636
Open Shrub	0.867769865	1.92853407
Herbaceous	0.578934521	3.673890736
Tussock Tundra	0.97019094	0.373923456
Sparsely Vegetated	0.636074481	3.485586829
Fen	0.828069497	2.222778424
Bog	0.822221402	2.511620862
Shallow-Littoral	0.632287257	3.563835385
Barren	0.769633058	3.212069184
Open Water	0.842016964	2.058542528

3.6.6 Table S3: Example Lookup Table of Moisture Values Varying with Backscatter

This is an example look-up table representing the open water class where moisture varies alongside expected values for backscatter. For the open water class, there is variation in moisture due to mixed pixels from the relatively low spatial resolution of the reference surface moisture dataset. Pixels having lower moisture values have a lower water fraction and are correlated with lower backscatter, likely due to the mixture of land and vegetation (which have low backscatter compared to water at near range) and due to the water dampening effect of vegetation on water.

Mean [σ_0dB]	Mean [moisture,%]	Stdev [moisture,%]	N
-1.58456	77.46552	26.18773	58
-1.03527	80.67857	23.57616	84
-0.41428	79.44604	24.89024	139
0.206599	79.97576	24.9934	165
0.82869	77.73276	26.53263	232
1.43599	79.81301	25.76657	246
2.050704	84.4939	23.32551	328
2.667682	84.13759	22.6418	407
3.269233	83.60879	22.87557	455
3.888232	82.96468	24.69955	538
4.498026	85.09425	21.84071	626
5.106603	85.66619	22.25574	704
5.713768	87.48333	20.803	720
6.320185	85.88547	22.33674	812
6.946563	88.51372	19.89841	911
7.551043	88.06116	20.53167	981
8.163685	88.2756	19.91512	918
8.78386	87.38308	21.18018	1052
9.391719	87.659	20.79142	1000
10.007	89.28021	19.19452	1117
10.60923	89.83412	18.70408	1278
11.21332	90.33612	17.83365	1315
11.85064	90.38787	18.40762	1534
12.47023	91.24403	17.60969	1844
13.0978	94.3606	14.01129	3178
13.68909	94.91729	13.6202	5042
14.33307	97.10643	10.29683	8635
14.90723	97.8522	8.69686	10311
15.50393	97.98239	8.474852	10393
16.1045	97.97534	8.486458	9285
16.71226	97.60107	8.915389	7470
17.32706	97.43703	9.32157	5661
17.93788	97.47845	9.427794	4107
18.55645	97.41703	9.264411	2736
19.17067	98.03393	7.924339	1945
19.78232	98.27338	7.881548	1251
20.37361	98.74349	5.622926	768
20.9804	98.30789	7.268499	380
21.58409	98.03509	8.449083	171
22.22585	99.18667	2.555827	75

Chapter 4:

4. AirSWOT Ka-band Near-Surface Wind Interactions

Title: Influence of Wind on Near-Nadir Ka-band SAR Backscatter and Interferometric Coherence over Small Inland Water Bodies

4.1 Introduction

The water-air interface is an important component in tracking and modeling wind-driven surface water dynamics [Xiao et al., 2018; Wu et al., 2022]. Wind induces waves and seiches and increases evaporation rates over lakes, for example [Van Hylckama 1968; Ma et al., 2016]. However, inland surface wind speeds are highly variable over space and time due to topographic relief, and boundary layer frictional resistance from surface features such as trees and buildings which reduce wind velocity. Because of the spatially varying nature of wind speed over land, the availability of high-resolution datasets of airflow over inland water bodies, would increase the accuracy of models focused on atmospheric dynamics and the water cycle.

Radar remote sensing offers unique capabilities for tracking spatial and temporal variations in wind-induced surface water roughness, including estimation of wave heights and wind velocities over water. Such retrievals are traditionally obtained through scatterometry over oceans, [Jones et al., 1977; Rodriguez et al., 2018]. Classic scatterometry studies were conducted to establish geophysical model functions (GMFs) relating wind parameters to water surface scattering over ocean surfaces [Jones et al., 1977; Durden and Vesecky 1985; Giovanangeli et al., 1991; Yueh et

al., 2013; Rodriguez et al., 2018; Wineteer et al., 2020]. Due to oblique viewing geometries and poor calibration for SAR-wind GMFs, few have used SAR imagery to assess surface water scattering [Monaldo et al., 2013].

While SAR sensors offer high spatial resolution and focused imagery over inland water compared with scatterometers, to our knowledge, there has been no attempt to quantitatively assess wind-induced roughness of multiple small inland water bodies using SAR data. For this reason, the potential influence of wind on Ka-band returns for small inland water from the forthcoming Surface Water and Ocean Topography (SWOT) satellite, the world's first hydrology-focused InSAR mission, remains poorly understood.

Preliminary experiments demonstrated that AirSWOT (an experimental airborne Ka-band precursor to SWOT, see [Moller et al., 2010; Wu et al., 2011]), SAR backscatter returns over inland surface water bodies appear to be sensitive to emergent vegetation and wind [Fayne et al., *in review,* Altenau et al., 2017, Pitcher et al., 2019, Denbina et al., 2019]. For accurate SWOT and AirSWOT data retrievals of water surface elevation (WSE) and extent, inland water bodies must present strong signal returns (backscatter) and internally consistent transmit/receive signals (interferometric coherence). AirSWOT observations over Canada and Alaska have produced water surface elevations that do not quite meet the designed accuracy standard of 10 cm [Altenau 2017; Pitcher et al., 2019; Denbina et al., 2019; Touzzolo et al., 2019; Fayne et al., 2020] due in part to low backscatter ("dark water") and low coherence from water surfaces [Fayne et al., 2020]. Furthermore, pre-launch assessments of SWOT's potential vulnerability to dark-water returns over small inland water bodies use traditional scatterometry models developed for oceans using coarse resolution Ka-band radar data from precipitation satellite GPM (5 km) and altimetry satellite AltiKa (12 km) [Peral et al., 2015; Frappart et al., 2015; Nouguier et al., 2016; Rodriguez et al.,

2017; Rodriguez et al., 2018; Frappart et al., 2020], a scale far coarser than most inland water bodies. Using high-resolution optical remote sensing, for example, Cooley et al., [2019] report an average area of just 26 m^2 for ~85,000 lakes across Canada and Alaska.

The SWOT satellite will image water bodies with a minimum area of (250 $m)^2$, while AirSWOT is capable of imaging water bodies with a minimum area of 10 m^2 [Fjørtoft et al., 2014; Fayne et al., 2020]. Because of the influence of local topography and diverse water body shapes and sizes, we suspect that existing Ka-band scattering models designed for features greater than 10 km^2 may not be sufficient for modeling the impacts of surface wind friction velocities for millions of smaller water bodies which will be observed by SWOT. Understanding the relationship between wind speed, wind direction, and radar backscatter will increase our ability to estimate the quality of SWOT observations prior to the flyover, and improve planning capabilities for airborne AirSWOT data acquisitions. Studying how wind speeds influence radar backscatter and coherence can help to estimate and improve the performance of derived InSAR elevation estimates. While this work seeks to improve our understanding of the performance of Ka-band InSAR sensors for estimating water surface elevations, the simultaneous work of quantifying the relationship between Ka-band backscatter and wind characteristics for small waterbodies will enable future investigations of wind-water friction velocities for assessing hyper-local evaporation and water vapor transport.

This study assesses the influence of wind on Ka-band scattering for 11,072 water features across Alaska and western Canada, which were imaged across ~22,000 km^2 of AirSWOT flights for the NASA Arctic-Boreal Vulnerability Experiment (ABoVE) [Fayne et al., 2020]. The areas of these water features range from 350 m^2 to 156 km^2, including lakes too small to detect from AltiKa and GPM. Figure 19 highlights the flight path of the AirSWOT data collected during the

2017 summer field campaign. Using reference wind speed and direction data from modeled and in-situ data sources and Ka-band backscatter, coherence, and flight heading data from AirSWOT, we correlate wind and radar data to identify scattering sensitivities to wind speed and direction. For incidence angles 0-17°, we determine that 1) wind speeds 3 m/s or higher are required for strong backscatter and coherence, leading to higher accuracy elevation data and 2) the AirSWOT data used in this study does not capture enough varying conditions of wind direction to be comparable with Ka-band wind direction GMFs and theoretical models. We conclude with a discussion on further implications of Ka-band SAR data for wind speed assessments and InSAR water surface elevation retrievals for SWOT.

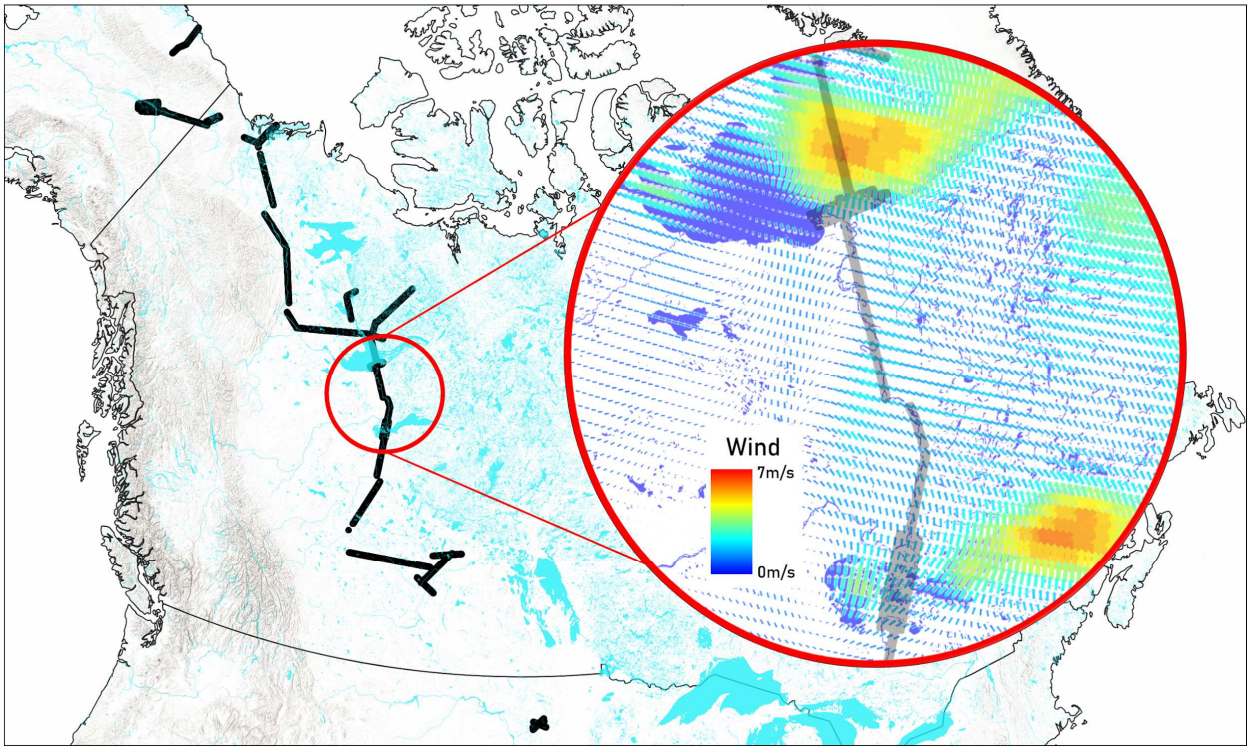

Figure 19. *The 2017 AirSWOT data collection (black lines) was acquired as a part of the Arctic Boreal Vulnerability Experiment (ABoVE) Airborne Campaign (AAC), beginning in North Dakota, USA, and flying north through Western Canada to Alaska, USA, before returning south along an overlapping flight path. The inset highlights a snapshot (July 1, 2017) of the spatial variability of*

wind speeds from ERA-5 Reanalysis over several lakes in southern Northwest Territories and northern Alberta.

4.2 Data

4.2.1 AirSWOT Ka-band Interferometric Synthetic Aperture Radar

The airborne SWOT (AirSWOT) platform supports a Ka-band interferometric wide-swath altimeter, called the Ka-band SWOT Phenomenology Radar (KaSPAR), which is used to produce high-resolution maps of water surface elevations [NASA JPL 2022]. AirSWOT was developed as a complement to SWOT to understand surface phenomenological interactions and to test and design radar and InSAR algorithms at Ka band [Moller et al. 2010; Wu et al. 2011]. While AirSWOT has collected small datasets over various parts of the United States [Altenau et al., 2017; Pitcher et al., 2019; Tuozzolo et al., 2020; Denbina et al., 2020], the largest published AirSWOT collection to date is from a July 8-August 17, 2017 airborne flight and field campaign conducted for the NASA Arctic Boreal Vulnerability Experiment (ABoVE) [Fayne et al., 2019, 2020; Miller et al., 2019]. The collection acquired ~22,000 km^2 km of flight lines spanning 23° in latitude, ranging from North Dakota through Canada to Alaska and back again. The collection covered over 40,000 inland water bodies [Kyzivat et al., 2019]. These lakes have varying sizes, orientations, shapes, and prevailing wind conditions. Though the available "outer swath" radar data used in this study has a nominal incidence angle range of ~3-27° (some observations cover 0.5-3°), higher incidences are removed from this study, limiting the analysis to 3-17°. After filtering, the number of water bodies remaining to be studied here is 11,072. The radar data products used in the analysis are incidence angle, noise subtracted and calibrated backscatter, total coherence, and un-gridded geolocation (LLHE) processed by the NASA Jet Propulsion Laboratory

(JPL) and presented in Fayne et al. [2019]. These data have a gridded pixel spacing of 3.6 meters, an average swath width of 4 km, and an average flight altitude of 9.5 km. The 2017 ABoVE AirSWOT products are freely available for download at https://daac.ornl.gov/cgi-bin/dsviewer.pl?ds_id=1646). For technical descriptions of the AirSWOT instrument configuration and these data products, see Moller et al. [2010] and Fayne et al. [2019].

4.2.2 Modeled and In-Situ Wind Parameters

Wind speed and direction data from three different datasets are used to compare with AirSWOT data. Reanalysis data from the European Center for Medium-Range Weather Forecasts (ECMWF) *ERA5 hourly data on single levels from 1979 to present* [Copernicus Climate Change Service, 2022, accessed March 2022; https://cds.climate.copernicus.eu/cdsapp#!/dataset/reanalysis-era5-single-levels?tab=overview] is the primary wind speed and direction reference dataset. The ERA-5 hourly data used in this study include 10 km resolution geolocated U- and V- component wind speeds at 10 m heights, which are converted to total wind speed (*Eq. 1*) and wind direction (*Eq. 2*) as follows:

$$\vec{V} = \sqrt{u^2 + v^2}$$

Eq. 1

$$\phi = \left(180 + \left(\frac{180}{\pi}\right) * atan2(v, u)\right) \%\% \, 360$$

Eq. 2

To include and prioritize in-situ wind speed and direction measurements where available, we use hourly and sub-daily in-situ meteorological stations around Wood Buffalo National Park [Wood Buffalo Environmental Association, 2022] and from approximately 40 more sparsely placed in situ stations throughout western Canada and Alaska from Copernicus *Global land surface atmospheric variables from 1755 to 2020 from comprehensive in-situ observations* [Copernicus Climate Change Service, 2022, accessed March 2022; https://cds.climate.copernicus.eu/cdsapp#!/dataset/insitu-observations-surface-land?tab=overview]. These in-situ measurements are spatially integrated together with the gridded ERA-5 data to form a single combined wind parameter dataset, as explained in the next section. Because these sites do not have consistent measurements for all time steps, the number of total in-situ stations integrated into the regularly gridded ERA-5 modeled data varies between 20-80 stations for each time step across the study domain.

4.3 Methods

4.3.1 Extract Ka-band radar backscatter and coherence over more than 11,000 inland water bodies

To compare AirSWOT backscatter and coherence from small inland water surfaces with wind speed and direction, we use a camera-based reference water mask acquired simultaneously with AirSWOT radar data [Kyzivat et al., 2020]. The water mask is derived from 1-meter optical imagery from a Cirrus Designs Digital Camera System (DCS) mounted on the AirSWOT Beechcraft Super King Air B200 aircraft, consisting of 40,000 open-water polygons with areas ranging from 40 m^2 to 156 km^2 [Kyzivat et al., 2019]. Individual coherence and backscatter pixel

values were extracted from within these independently identified water body polygons and filtered by incidence angle, enabling analysis of 11,072 remaining water features.

4.3.2 Interpolate local wind speed and direction

Gridded wind speed and wind direction data are produced by integrating three reference wind datasets. Because the AirSWOT swaths are 4 km wide, narrower than the 10 km ERA-5 data, we resample the ERA-5 data to a 5 km grid and add sparsely located and temporally varying in-situ stations to produce hourly wind speed and direction datasets. The 5 km hourly data are produced by converting the ERA-5 gridded raster data into geolocated-pixel-centroid points, which are combined with the geolocated in-situ points from the Wood Buffalo and Copernicus data. The combined points from the three datasets are spatially interpolated to a 5 km grid, leaving the majority of the resampled ERA-5 data values similar or identical to the original dataset except for near in-situ stations.

4.3.3 Compare AirSWOT Ka-band SAR backscatter and InSAR coherence with wind speed

Wind speed values are extracted for each of the point coordinates corresponding to the radar data extracted from within the predefined water features. We bin wind speeds into seven 1 m/s categories (from 0 to 7m/s) for comparison with AirSWOT Ka-band backscatter and coherence values, using box plots as in Rodriguez et al. (2018). The resultant box plots reveal how increasing wind speeds influence AirSWOT Ka-band backscatter and coherence over inland water bodies.

4.3.4 Compare AirSWOT Ka-band SAR backscatter and InSAR coherence with wind direction

Wind direction is similarly derived from the point corresponding to the nearest neighbor radar point within the water features. Additionally, we assess the heading of the AirSWOT aircraft to offset the flight heading from the wind direction. The flight heading is formatted as -180 to 180

degrees, which we shift by adding 180 to make the range 0 to 360 to match the wind direction data. Wind influences scattering in reference to the flight path as upwind (0 degrees), downwind (180/-180), and crosswind (-90/90). We calculate these azimuthal wind values relative to the flight heading using a simple offset described in *Eq. 3*:

$$\phi_{WindAzimuth} = 180 - (\varphi_{Flight} - \varphi_{Wind})$$

Eq. 3

Azimuthal wind directions are separated into 10-degree bins (from -180 to 180 degrees), and box plots are generated using the observed backscatter and coherence. These box plots enable comparison of observed AirSWOT backscatter-wind azimuth relationships to a theoretical sinusoidal relationship reported in a classic earlier modeling study (i.e., a three cosine model, Giovanangeli et al., 1991).

4.4 Results

4.4.1 Interpolate local wind speed and direction

We produce 5 km hourly raster files representing wind speed and direction covering Canada and Alaska. Their full extent spans 50 degrees to 70 degrees North latitude and 60 to 180 degrees West longitude. Figure 1 presents a close-up of these wind speed data. Because of the spatially and temporally varying availability of the in-situ stations (i.e., 20-80 stations have uneven observations across 20 degrees latitude, 120 degrees longitude, and 1500 hours), the in-situ data rarely cover AirSWOT observation regions, severely hampering their utility. Nonetheless, the in-

situ data are included, where possible, and the ERA-5 modeled data has even temporal and spatial coverage for this study.

4.4.2 Compare AirSWOT Ka-band SAR backscatter and InSAR coherence with wind speed

Strong relationships are found between wind speed and Ka-band backscatter and coherence, as seen in Figure 20. Radar backscatter increases with wind speed, with relatively low values (averaging around -3 to 5 dB) associated with wind speeds <3m/s. The first incidence angle bin (0.05-0.1 radians, 2.8-5.7°), which approximates SWOT incidence angles (~0.5-4.1°) suggests that hourly mean wind speeds of ~0 m/s yield a median backscatter of ~0 dB. At 7 m/s, the median backscatter increases to ~15 dB. This overall increase in backscatter for wind speeds >3 m/s manifests across all incidence angles, despite the expected incidence angle-dependent decrease in scattering (Figure 20). Even the fifth incidence angle bin, midway across the AirSWOT swath (0.25-0.3 radians, 14.3-17.2°), exhibits backscatter increases from ~ -10 dB to ~3 dB.

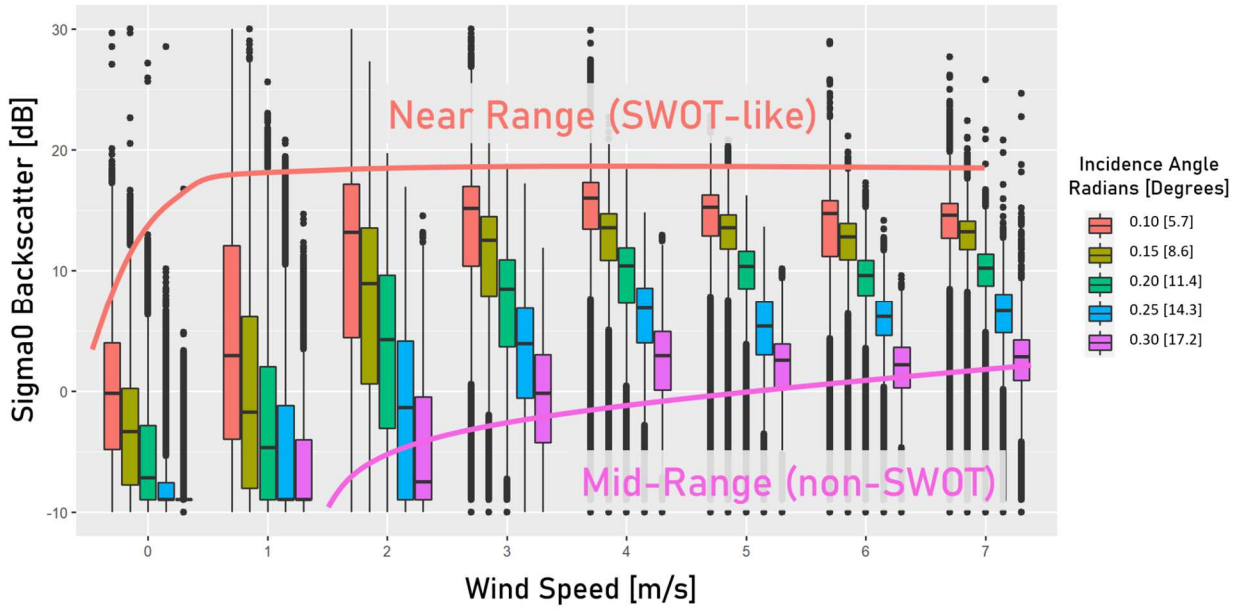

Figure 20. *Comparison of AirSWOT Ka-band backscatter with wind speed (0-7m/s) over ~11,000 small inland water bodies in western Canada and Alaska. Backscatter consistently increases with increasing wind speeds across all incidence angles. Wind speeds 3 m/s or higher for incidence angles between 3-8.6 degrees achieve the minimum ideal value to consistently separate water from land or other wet surfaces(>10 dB). The first incidence angle category (0.05-0.1 radians, 2.8-5.7 degrees) is most comparable to SWOT due to similar viewing geometry. This second category shows consistently high backscatter, 15 dB, for wind speeds greater than 3m/s.*

To obtain backscatter values consistently 10-20 dB, are greater than 3 m/s, wind speeds much ideally reach 3 m/s or higher, suggesting that Ka-band SAR images will not yield useful WSE retrievals when winds are below 3 m/s. This recommendation is further corroborated by comparing wind speed with AirSWOT interferometric coherence (Figure 21). For accurate estimation of water surface elevation from AirSWOT or SWOT data, coherence over water bodies should be high (ideally ~0.75-1). Our comparison of wind speeds with AirSWOT coherence demonstrates consistently high coherence, greater than 0.75, for incidence angles 0.05-0.3 radians (2.9-17.2 degrees) when wind speeds are 3 m/s or greater.

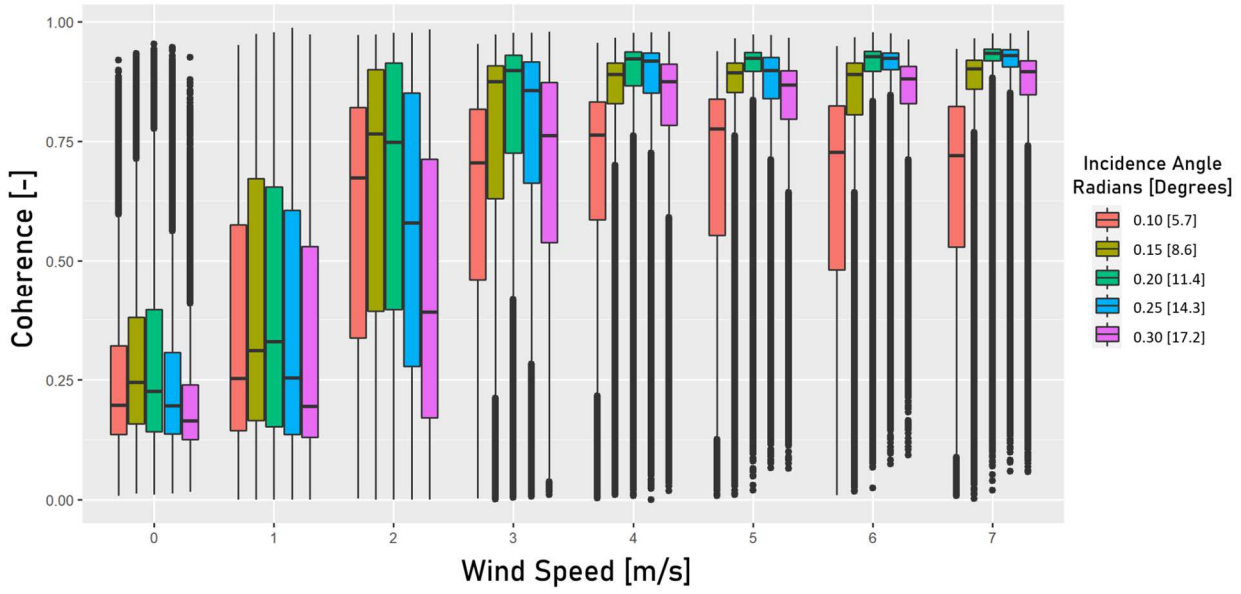

Figure 21. *Comparison of AirSWOT Ka-band coherence with wind speed (0-7m/s) over ~11,000 small inland water bodies in western Canada and Alaska. Coherence consistently increases with increasing wind speeds across all incidence angles. Wind speeds 3 m/s or higher for incidence angles between 2.9-17.2 degrees achieve the minimum ideal value for producing high-quality AirSWOT elevations (>0.75). The first incidence angle category (0.05-0.1 radians, 2.8-5.7 degrees), while most comparable to SWOT due to similar viewing geometry, does not have the highest coherence due to the AirSWOT antenna pointing having been focused near 12.9 degrees. Due to the antenna pointing, the highest coherence is identified in the third category (0.15-0.2 radians, 8.6-11.4 degrees), with coherence values exceeding 0.85 for wind speeds greater than 3m/s. Wind speeds of 3-7 m/s are much more likely to produce highly coherent data, which is important for reducing horizontal and vertical errors in the computed elevation product.*

4.4.3 Compare AirSWOT Ka-band SAR backscatter and InSAR coherence with wind direction

Upon conducting the wind direction analysis, we find an insufficient number of samples spanning a necessary diversity of wind directions and speeds to compare with the AirSWOT radar observations, shown in Figure 22. More specifically, we find abundant high wind speed observations for only a small subset of wind directions (210-320 degrees), and low wind speeds

dominated by another subset of wind directions (30-150). A clear relationship is found between wind direction and wind speed, which can only be explained by a seasonal effect (stronger winds from the southwest). Due to this relatively narrow range of wind direction/speed combinations, together with the fixed azimuthal headings of the long 2017 AirSWOT flight lines acquired over a relatively short period of time, we are unable to assess the influence of wind direction on either backscatter or interferometric coherence from the 2017 ABoVE AirSWOT data collection.

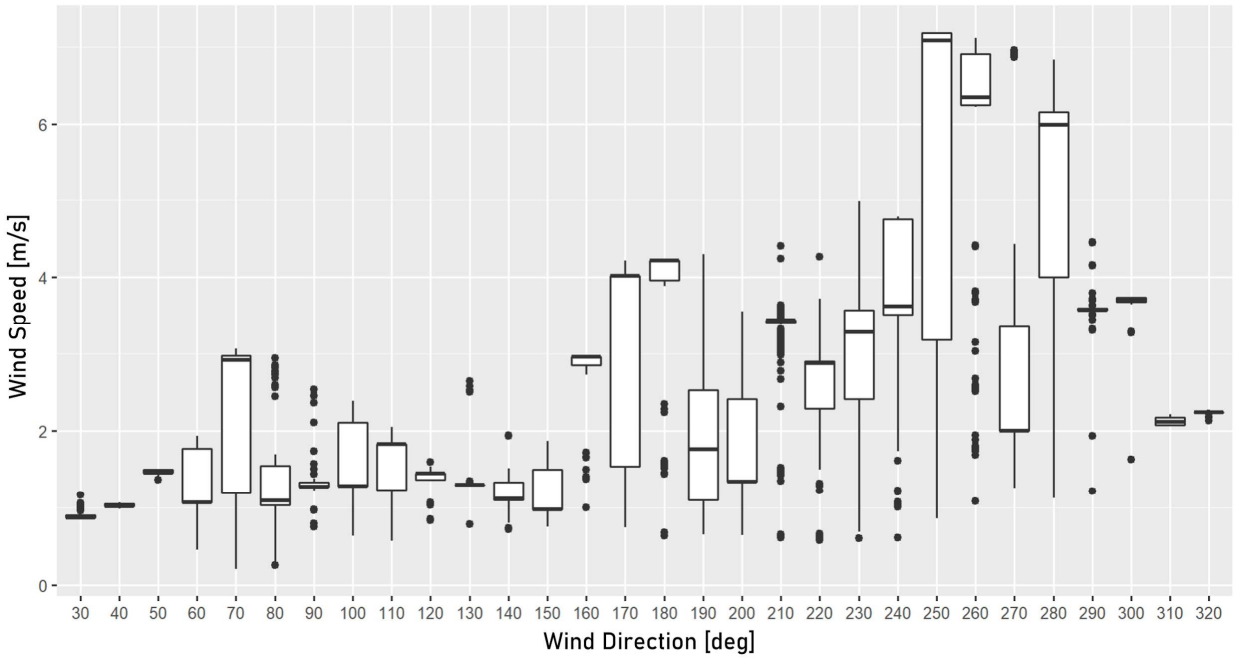

Figure 22. *An incomplete distribution of wind directions and speeds occurred during the NASA ABoVE AirSWOT flight campaigns (July 08 -August 17, 2017). During these flight acquisitions, high wind speeds occurred at wind directions 210-320 degrees, while directions 30-150 degrees experienced lower wind speeds. Wind directions between 320 and 30 degrees (winds from the north) rarely occurred during the AirSWOT flight acquisitions. A statistical assessment of the influence of wind direction on the AirSWOT Ka-band backscatter and coherence is not possible due to this insufficient diversity of wind direction/wind speed combinations during the flight campaigns.*

4.5. Discussion and Conclusion

The 2017 AirSWOT flight experiment provides a rare trove of Ka-band backscatter and interferometric coherence imagery (Fayne et al. 2019; 2020), as well as simultaneous near-infrared camera imagery and open-water classifications (Kyzivat et al. 2018; 2019), over 11,072 inland water bodies across Alaska and western Canada. By comparing AirSWOT Ka-band radar returns from these water bodies with a resampled ERA-5 reanalysis wind speed and direction product, we identify robust correlations among wind speed, backscatter, and coherence. These correlations are generally consistent across different incidence angle ranges, albeit with lower backscatter and coherence at larger (i.e. more oblique) incidence angles. Due to the under-sampling of different wind direction/wind speed combinations during the 2017 AirSWOT flight campaign, we are unable to provide a comparable analysis of wind direction.

Our analysis of the 2017 AirSWOT Ka-band data suggests low accuracy water surface elevations are likely under low wind conditions (<2 m/s). Referencing best practices for high accuracy Ka-band InSAR retrievals of water surface elevation (i.e. >5 dB backscatter and >0.8 coherence, Fayne et al. 2020]), we conclude that wind speeds of 0-3 m/s wind produce unacceptably low backscatter (<0 dB) and coherence (~0.25) across all incidence angles. Wind speeds of ~3 m/s and higher produce high values of SAR backscatter (>10 dB) and interferometric coherence (>0.8) optimal for water surface elevation retrieval.

Our study characterizes Ka-band radar returns from small inland water bodies (350 m^2 - 155 km^2), which are critically important to the SWOT satellite mission's success. SWOT will use wide-swath Ka-band interferometry with 10-70 m spatial resolution to estimate areas and surface elevations of millions of inland water bodies as small as 250m x 250m (0.0625 km^2). Previous studies using GPM and AltiKa data focused on much larger water bodies or ocean surfaces, with

emphasis on estimating wave heights and shapes for much higher wind speeds (up to 20 m/s) [Peral et al., 2015; Nougier et al., 2016; Rodriguez et al., 2018]. Nonetheless, our results agree with a high-resolution (600m x 36m) scatterometry study over the Gulf of Mexico, which determined that wind speeds of >2-3 m/s are necessary to retrieve meaningful radar returns [Wineteer et al., 2020]. Similarly, a bridge-mounted Ka-band system identified very strong backscatter (20 dB) from a river surface at wind speeds >2-3 m/s [Fjortoft et al., 2014]. This study lends further support to the notion that wind speeds of ~3 m/s or more may be necessary for the successful retrieval of water surface elevations over small inland water bodies from SWOT.

Previous scatterometry studies focused on large water bodies and open oceans having background surface wave roughness higher than the roughness seen from smaller water bodies, asserting minimum speeds of 2 m/s [Nougier et al., 2016; Rodriguez et al., 2018; Wineteer et al., 2020]. However, this study points to slightly higher wind speeds (i.e., at least 3 m/s) for successful water surface elevation retrieval over small inland water bodies. The 1 m/s difference between these studies may be explained by the absence of internal turbulence or wave trains on small lakes, unlike the open ocean. Wind shadowing from surrounding topographic relief and frictional resistance from surrounding vegetation also dampen wind speeds over small inland water bodies, requiring a higher atmospheric wind speed to achieve comparable water surface roughening. Future studies on radar backscattering should incorporate high-resolution (sub-kilometer) DEM and land-cover-based wind speed modeling, to account for fine-scale phenomena induced by localized topographic and frictional resistance factors. Other limitations of our analysis include a dearth of observational data reflecting multiple wind directions relative to the fight heading.

Regardless of these limitations, we conclude that AirSWOT Ka-band InSAR data are sensitive to wind speeds, producing higher quality backscatter and InSAR coherence data when

wind speeds reach and exceed 3 m/s. Unlike scatterometry studies, the goal of this research is not to produce new GMFs, but to assess Ka-band wind sensitivities as related to AirSWOT and SWOT water surface elevation retrieval accuracies. Future research on surface scattering from radars not designed for scatterometry will create opportunities for high-resolution wind monitoring, enabling greater advancements in the study of water-air interactions and the water cycle, for example, investigations of limnology and evaporation. Further, studies of wind-induced sources of error and uncertainty will aid in data screening protocols and quality assessment for AirSWOT and SWOT Ka-band water surface elevation retrievals.

Chapter 5

5.1 Conclusion

To gain an empirical understanding of the utility of near-nadir Ka-band for mapping surface changes, particularly concerning water and wet surfaces, Chapter 2 of this dissertation demonstrated the utility for mapping water surface inundation and elevation using KaSPAR InSAR data collected on the AirSWOT platform by investigating sources of- and quantifying absolute errors in water surface elevation (WSE) estimate. As part of the NASA Arctic Boreal and Vulnerability Experiment (ABoVE), AirSWOT data demonstrated absolute height errors and biases which exceed SWOT requirements. The experimental InSAR technology used in AirSWOT KaSPAR suggests that theoretical expectations for near-nadir Ka-band do not align with field observations. While there are significant differences between the experimental AirSWOT airborne platform and the SWOT satellite, if these same effects are assumed for the satellite mission, errors observed in AirSWOT may be present in SWOT. If required, knowledge of such sources of error can help guide algorithm development in support of the SWOT mission.

Preliminary assessments of the AirSWOT Ka-band InSAR data revealed difficulties in classifying water surfaces, particularly when water is in proximity to other wet surfaces. A survey of radar scattering literature for water surfaces, in turn, indicated a dearth of knowledge surrounding near-nadir Ka-band scattering for heterogeneous regions containing water and land, in comparison to homogeneous surfaces such as oceans. Chapter 3 identifies the magnitudes of the differences and similarities for backscattering values in the comparison of water and 14 land cover types to assess misclassification prevalence due to similar surface texture and moisture regimes.

Chapter 3 identifies Ka-band sensitivity to canopy structure, particularly of sparse vegetation, enabling unique assessments of vegetation type. In comparing wet surface sensitivity, it was also revealed that Ka-band backscatter could observe shallow wet surfaces such as wetlands and ponding due to rainfall or seasonal permafrost thaw. Chapter 4 focuses on the open water region only and demonstrates that AirSWOT KaSPAR data have similar wind speed sensitivity to conventional scatterometers. This finding is particularly unique as the field of scatterometry, and the study of wind speed scattering relationships have traditionally studied only large water bodies such as oceans and seas.

6. References

[1] W. Alpers, B. Zhang, A. Mouche, K. Zeng, and P. W. Chan, "Rain footprints on C-band synthetic aperture radar images of the ocean - Revisited," *Remote Sensing of Environment*, vol. 187, pp. 169–185, Dec. 2016, doi: 10.1016/j.rse.2016.10.015.

[2] D. E. Alsdorf and D. P. Lettenmaier, "Tracking Fresh Water from Space," *Science*, vol. 301, no. 5639, pp. 1491–1494, Sep. 2003, doi: 10.1126/science.1089802.

[3] D. E. Alsdorf, E. Rodríguez, and D. P. Lettenmaier, "Measuring surface water from space," *Reviews of Geophysics*, vol. 45, no. 2, 2007, doi: 10.1029/2006RG000197.

[4] E. H. Altenau *et al.*, "AirSWOT measurements of river water surface elevation and slope: Tanana River, AK," *Geophysical Research Letters*, vol. 44, no. 1, pp. 181–189, 2017, doi: 10.1002/2016GL071577.

[5] M. Amani *et al.*, "Canadian Wetland Inventory using Google Earth Engine: The First Map and Preliminary Results," *Remote Sensing*, vol. 11, no. 7, p. 842, Jan. 2019, doi: 10.3390/rs11070842.

[6] D. Atlas, "Footprints of storms on the sea: A view from spaceborne synthetic aperture radar," *Journal of Geophysical Research: Oceans*, vol. 99, no. C4, pp. 7961–7969, 1994, doi: 10.1029/94JC00250.

[7] E. P. W. Attema and F. T. Ulaby, "Vegetation modeled as a water cloud," *Radio Science*, vol. 13, no. 2, pp. 357–364, 1978, doi: 10.1029/RS013i002p00357.

[8] N. Baghdadi, M. Bernier, R. Gauthier, and I. Neeson, "Evaluation of C-band SAR data for wetlands mapping," *International Journal of Remote Sensing*, vol. 22, no. 1, pp. 71–88, Jan. 2001, doi: 10.1080/014311601750038857.

[9]

N. Baghdadi, H. Bazzi, M. El Hajj, and M. Zribi, “Detection of Frozen Soil Using Sentinel-1 SAR Data,” *Remote Sensing*, vol. 10, no. 8, Art. no. 8, Aug. 2018, doi: 10.3390/rs10081182.

[10] D. E. Barrick, “Relationship between slope probability density function and the physical optics integral in rough surface scattering,” *Proceedings of the IEEE*, vol. 56, no. 10, pp. 1728–1729, Oct. 1968, doi: 10.1109/PROC.1968.6718.

[11] J. B. Blair, D. L. Rabine, and M. A. Hofton, “The Laser Vegetation Imaging Sensor: a medium-altitude, digitisation-only, airborne laser altimeter for mapping vegetation and topography,” *ISPRS Journal of Photogrammetry and Remote Sensing*, vol. 54, no. 2–3, pp. 115–122, Jul. 1999, doi: 10.1016/S0924-2716(99)00002-7.

[12] B. Brisco *et al.*, “Evaluation of C-Band SAR for Identification of Flooded Vegetation in Emergency Response Products,” *Canadian Journal of Remote Sensing*, vol. 45, no. 1, pp. 73–87, Jan. 2019, doi: 10.1080/07038992.2019.1612236.

[13] M. F. Chen and A. K. Fung, “A numerical study of the regions of validity of the Kirchhoff and small-perturbation rough surface scattering models,” *Radio Science*, vol. 23, no. 2, pp. 163–170, 1988, doi: 10.1029/RS023i002p00163.

[14] M. Choker *et al.*, “Evaluation of the Oh, Dubois and IEM Backscatter Models Using a Large Dataset of SAR Data and Experimental Soil Measurements,” *Water*, vol. 9, no. 1, Art. no. 1, Jan. 2017, doi: 10.3390/w9010038.

[15] S. W. Cooley, L. C. Smith, J. C. Ryan, L. H. Pitcher, and T. M. Pavelsky, “Arctic-Boreal Lake Dynamics Revealed Using CubeSat Imagery,” *Geophysical Research Letters*, vol. 46, no. 4, pp. 2111–2120, 2019, doi: 10.1029/2018GL081584.

[16] J.-F. Crétaux *et al.*, “FLOOD MAPPING INFERRED FROM REMOTE SENSING DATA,” no. 1, p. 13, 2011.

[17] I. G. Cumming and J. J. van Zyl, “Feature Utility In Polarimetric Radar Image Classification,” in *12th Canadian Symposium on Remote Sensing Geoscience and Remote Sensing Symposium,* Jul. 1989, vol. 3, pp. 1841–1846. doi: 10.1109/IGARSS.1989.576569.

[18]
M. Denbina, M. Simard, E. Rodriguez, X. Wu, A. Chen, and T. Pavelsky, “Mapping Water Surface Elevation and Slope in the Mississippi River Delta Using the AirSWOT Ka-Band Interferometric Synthetic Aperture Radar,” *Remote Sensing*, vol. 11, no. 23, Art. no. 23, Jan. 2019, doi: 10.3390/rs11232739.

[19]
P. C. DuBois, J. J. van Zyl, and T. Engman, “Measuring soil moisture with imaging radars,” *IEEE Trans. Geosci. Remote Sens*, no. 33, pp. 915–926, 1995.

[20]
M. Durand, L.-L. Fu, D. P. Lettenmaier, D. E. Alsdorf, E. Rodriguez, and D. Esteban-Fernandez, “The Surface Water and Ocean Topography Mission: Observing Terrestrial Surface Water and Oceanic Submesoscale Eddies,” *Proceedings of the IEEE*, vol. 98, no. 5, pp. 766–779, May 2010, doi: 10.1109/JPROC.2010.2043031.

[21]
S. Durden and J. Vesecky, “A physical radar cross-section model for a wind-driven sea with swell,” *IEEE Journal of Oceanic Engineering*, vol. 10, no. 4, pp. 445–451, Oct. 1985, doi: 10.1109/JOE.1985.1145133.

[22]
E. Peral and D. Esteban-Fernandez, “Swot Mission Performance and Error Budget,” in *IGARSS 2018 - 2018 IEEE International Geoscience and Remote Sensing Symposium*, Jul. 2018, pp. 8625–8628. doi: 10.1109/IGARSS.2018.8517385.

[23]
D. Esteban-Fernandez, L.-L. Fu, E. Rodriguez, S. Brown, and R. Hodges, “Ka-band SAR interferometry studies for the SWOT mission,” in *2010 IEEE International Geoscience and Remote Sensing Symposium*, Jul. 2010, pp. 4401–4402. doi: 10.1109/IGARSS.2010.5652302.

[24]
J. V. Fayne, L. C. Smith, L. H. Pitcher, and T. M. Pavelsky, “ABoVE: AirSWOT Ka-band Radar over Surface Waters of Alaska and Canada, 2017,” *ORNL DAAC*, Mar. 2019, doi: https://doi.org/10.3334/ORNLDAAC/1646.

[25]
J. V. Fayne *et al.*, “Airborne observations of arctic-boreal water surface elevations from AirSWOT Ka-Band InSAR and LVIS LiDAR,” *Environ. Res. Lett.*, vol. 15, no. 10, p. 105005, Oct. 2020, doi: 10.1088/1748-9326/abadcc.

[26]

J. V. Fayne and L. C. Smith, “Characterization of Near-Nadir Ka-Band Scattering from Wet Surfaces,” in *2021 IEEE International Geoscience and Remote Sensing Symposium IGARSS*, Jul. 2021, pp. 6132–6135. doi: 10.1109/IGARSS47720.2021.9553413.

[27]

R. Fjørtoft *et al.*, “KaRIn - the Ka-band radar interferometer on SWOT: Measurement principle, processing and data specificities,” in *2010 IEEE International Geoscience and Remote Sensing Symposium*, Jul. 2010, pp. 4823–4826. doi: 10.1109/IGARSS.2010.5650601.

[28]

R. Fjørtoft *et al.*, “KaRIn on SWOT: Characteristics of Near-Nadir Ka-Band Interferometric SAR Imagery,” *IEEE Transactions on Geoscience and Remote Sensing*, vol. 52, no. 4, pp. 2172–2185, Apr. 2014, doi: 10.1109/TGRS.2013.2258402.

[29]

F. Frappart *et al.*, “Radar altimetry backscattering signatures at Ka, Ku, C, and S bands over West Africa,” *Physics and Chemistry of the Earth, Parts A/B/C*, vol. 83–84, pp. 96–110, Jan. 2015, doi: 10.1016/j.pce.2015.05.001.

[30]

F. Frappart *et al.*, “Backscattering signatures at Ka, Ku, C and S bands from low resolution radar altimetry over land,” *Advances in Space Research*, Jul. 2020, doi: 10.1016/j.asr.2020.06.043.

[31]

R. P. de M. Frasson, G. J.-P. Schumann, A. J. Kettner, G. R. Brakenridge, and W. F. Krajewski, “Will the Surface Water and Ocean Topography (SWOT) Satellite Mission Observe Floods?,” *Geophysical Research Letters*, vol. 46, no. 17–18, pp. 10435–10445, 2019, doi: 10.1029/2019GL084686.

[32]

J.- Giovanangeli, L. F. Bliven, and O. L. Calve, “A wind-wave tank study of the azimuthal response of a Ka-band scatterometer,” *IEEE Transactions on Geoscience and Remote Sensing*, vol. 29, no. 1, pp. 143–148, Jan. 1991, doi: 10.1109/36.103304.

[33]

C. R. Grant and B. S. Yaplee, “Back Scattering from Water and Land at Centimeter and Millimeter Wavelengths,” *Proceedings of the IRE*, vol. 45, no. 7, pp. 976–982, Jul. 1957, doi: 10.1109/JRPROC.1957.278508.

[34]

T. Hagfors, “Relationship of geometric optics and autocorrelation approaches to the analysis of lunar and planetary radar,” *Journal of Geophysical Research (1896-1977)*, vol. 71, no. 2, pp. 379–383, 1966, doi: 10.1029/JZ071i002p00379.

[35]
M. T. Hallikainen, F. T. Ulaby, M. C. Dobson, M. A. El-rayes, and L. Wu, “Microwave Dielectric Behavior of Wet Soil-Part 1: Empirical Models and Experimental Observations,” *IEEE Transactions on Geoscience and Remote Sensing*, vol. GE-23, no. 1, pp. 25–34, Jan. 1985, doi: 10.1109/TGRS.1985.289497.

[36]
L. L. Hess, J. M. Melack, S. Filoso, and Yong Wang, “Delineation of inundated area and vegetation along the Amazon floodplain with the SIR-C synthetic aperture radar,” *IEEE Transactions on Geoscience and Remote Sensing*, vol. 33, no. 4, pp. 896–904, Jul. 1995, doi: 10.1109/36.406675.

[37]
L. L. Hess, J. M. Melack, E. M. L. M. Novo, C. C. F. Barbosa, and M. Gastil, “Dual-season mapping of wetland inundation and vegetation for the central Amazon basin,” *Remote Sensing of Environment*, vol. 87, no. 4, pp. 404–428, Nov. 2003, doi: 10.1016/j.rse.2003.04.001.

[38]
E. W. Hoen and H. A. Zebker, “Topography-driven variations in backscatter strength and depth observed over the Greenland Ice Sheet with InSAR,” in *IGARSS 2000. IEEE 2000 International Geoscience and Remote Sensing Symposium. Taking the Pulse of the Planet: The Role of Remote Sensing in Managing the Environment. Proceedings (Cat. No.00CH37120)*, Jul. 2000, vol. 2, pp. 470–472 vol.2. doi: 10.1109/IGARSS.2000.861599.

[39]
J. A. Holzer and C. C. Sung, “Scattering of electromagnetic waves from a rough surface. II,” *Journal of Applied Physics*, vol. 49, no. 3, pp. 1002–1011, Mar. 1978, doi: 10.1063/1.325037.

[40]
J. A. Holzer and C. C. Sung, “Scattering of electromagnetic waves from a rough surface. II,” *Journal of Applied Physics*, vol. 49, no. 3, pp. 1002–1011, Mar. 1978, doi: 10.1063/1.325037.

[41]
T. Jackson, “Effects of Soil Properties on Microwave Dielectric Constants,” *Transportation Research Record*, 1987, Accessed: Aug. 03, 2021. [Online]. Available:

https://www.semanticscholar.org/paper/EFFECTS-OF-SOIL-PROPERTIES-ON-MICROWAVE-DIELECTRIC-Jackson/72e785e95f4b7313004eb993cf9da30908a3a21b

[42] W. Jones, L. Schroeder, and J. Mitchell, "Aircraft measurements of the microwave scattering signature of the ocean," *IEEE Journal of Oceanic Engineering*, vol. 2, no. 1, pp. 52–61, Jan. 1977, doi: 10.1109/JOE.1977.1145330.

[43] E. S. Kasischke, J. M. Melack, and M. Craig Dobson, "The use of imaging radars for ecological applications—A review," *Remote Sensing of Environment*, vol. 59, no. 2, pp. 141–156, Feb. 1997, doi: 10.1016/S0034-4257(96)00148-4.

[44] P. Kumar, R. Singh, H. Singh, T. Chand, and N. Bala, "Assessment of soil carbon dioxide efflux and its controlling factors in moist temperate forest of West Himalayas," *CURRENT SCIENCE*, vol. 119, no. 4, p. 9, 2020.

[45] E. D. Kyzivat *et al.*, "A High-Resolution Airborne Color-Infrared Camera Water Mask for the NASA ABoVE Campaign," *Remote Sensing*, vol. 11, no. 18, Art. no. 18, Jan. 2019, doi: 10.3390/rs11182163.

[46] B. Lehner and P. Döll, "Development and validation of a global database of lakes, reservoirs and wetlands," *Journal of Hydrology*, vol. 296, no. 1, pp. 1–22, Aug. 2004, doi: 10.1016/j.jhydrol.2004.03.028.

[47] T.-H. Liao, M. Simard, M. Denbina, and M. P. Lamb, "Monitoring Water Level Change and Seasonal Vegetation Change in the Coastal Wetlands of Louisiana Using L-Band Time-Series," *Remote Sensing*, vol. 12, no. 15, Art. no. 15, Jan. 2020, doi: 10.3390/rs12152351.

[48] N. Ma *et al.*, "Evaporation variability of Nam Co Lake in the Tibetan Plateau and its role in recent rapid lake expansion," *JOURNAL OF HYDROLOGY*, vol. 537. ELSEVIER, RADARWEG 29, 1043 NX AMSTERDAM, NETHERLANDS, pp. 27–35, Jun. 2016. doi: 10.1016/j.jhydrol.2016.03.030.

[49] B. L. Méhauté, "Gravity–capillary rings generated by water drops," *Journal of Fluid Mechanics*, vol. 197, pp. 415–427, Dec. 1988, doi: 10.1017/S0022112088003301.

[50]

V. L. Mironov and Y. I. Lukin, “Temperature Dependable Microwave Dielectric Model for Frozen Soils,” *PIERS Online*, vol. 5, no. 5, pp. 406–410, 2009, doi: 10.2529/PIERS090220040026.

[51] F. Mohammadimanesh, B. Salehi, M. Mahdianpari, B. Brisco, and M. Motagh, “Multi-temporal, multi-frequency, and multi-polarization coherence and SAR backscatter analysis of wetlands,” *ISPRS Journal of Photogrammetry and Remote Sensing*, vol. 142, pp. 78–93, Aug. 2018, doi: 10.1016/j.isprsjprs.2018.05.009.

[52] D. Moller, E. Rodriguez, J. Carswell, and D. Esteban-Fernandez, “AirSWOT- A Calibration/Validation Platform for the SWOT Mission,” presented at the IGARSS 2010, 2010.

[53] R. Moore, Y. Yu, A. Fung, D. Kaneko, G. Dome, and R. Werp, “Preliminary study of rain effects on radar scattering from water surfaces,” *IEEE Journal of Oceanic Engineering*, vol. 4, no. 1, pp. 31–32, Jan. 1979, doi: 10.1109/JOE.1979.1145408.

[54] F. Nouguier, A. Mouche, N. Rascle, B. Chapron, and D. Vandemark, “Analysis of Dual-Frequency Ocean Backscatter Measurements at Ku- and Ka-Bands Using Near-Nadir Incidence GPM Radar Data,” *IEEE Geoscience and Remote Sensing Letters*, vol. 13, no. 9, pp. 1310–1314, Sep. 2016, doi: 10.1109/LGRS.2016.2583198.

[55] U. D. of C. N. N. E. S. D. and I. S. O. of S. and P. Operations, “NOAA’s Office of Satellite and Product Operations.” https://www.ospo.noaa.gov/Products/land/smops/ (accessed Jan. 25, 2021).

[56] E. Peral, E. Rodríguez, and D. Esteban-Fernández, “Impact of Surface Waves on SWOT’s Projected Ocean Accuracy,” *Remote Sensing*, vol. 7, no. 11, Art. no. 11, Nov. 2015, doi: 10.3390/rs71114509.

[57] L. H. Pitcher *et al.*, “AirSWOT InSAR Mapping of Surface Water Elevations and Hydraulic Gradients Across the Yukon Flats Basin, Alaska,” *Water Resources Research*, vol. 55, no. 2, pp. 937–953, 2019, doi: 10.1029/2018WR023274.

[58]

Y. Reuveni, Y. Bock, X. Tong, and A. W. Moore, "Calibrating interferometric synthetic aperture radar (InSAR) images with regional GPS network atmosphere models," *Geophys J Int*, vol. 202, no. 3, pp. 2106–2119, Sep. 2015, doi: 10.1093/gji/ggv253.

[59]

E. Rodriguez, D. E. Fernandez, E. Peral, C. W. Chen, J.-W. D. Bleser, and B. Williams, "Wide-Swath Altimetry: A Review," in *Satellite Altimetry over Oceans and Land Surfaces*, CRC Press, 2017.

[60]

E. Rodriguez and J. M. Martin, "Theory and Design of Interferometric Synthetic Aperture Radars", [Online]. Available: https://ieeexplore.ieee.org/iel1/2209/3716/00136293.pdf

[61]

E. Rodríguez *et al.*, "Estimating Ocean Vector Winds and Currents Using a Ka-Band Pencil-Beam Doppler Scatterometer," *Remote Sensing*, vol. 10, no. 4, Art. no. 4, Apr. 2018, doi: 10.3390/rs10040576.

[62]

P. A. Rosen *et al.*, "Synthetic aperture radar interferometry," *Proceedings of the IEEE*, vol. 88, no. 3, pp. 333–382, Mar. 2000, doi: 10.1109/5.838084.

[63]

M. Santoro, J. I. H. Askne, U. Wegmuller, and C. L. Werner, "Observations, Modeling, and Applications of ERS-ENVISAT Coherence Over Land Surfaces," *IEEE Transactions on Geoscience and Remote Sensing*, vol. 45, no. 8, pp. 2600–2611, Aug. 2007, doi: 10.1109/TGRS.2007.897420.

[64]

M. Santoro, A. Shvidenko, I. McCallum, J. Askne, and C. Schmullius, "Properties of ERS-1/2 coherence in the Siberian boreal forest and implications for stem volume retrieval," *Remote Sensing of Environment*, vol. 106, no. 2, pp. 154–172, Jan. 2007, doi: 10.1016/j.rse.2006.08.004.

[65]

C. Schlager, G. Kirchengast, J. Fuchsberger, A. Kann, and H. Truhetz, "A spatial evaluation of high-resolution wind fields from empirical and dynamical modeling in hilly and mountainous terrain," *Geoscientific Model Development*, vol. 12, no. 7, pp. 2855–2873, Jul. 2019, doi: https://doi.org/10.5194/gmd-12-2855-2019.

[66]

C. Schlager, G. Kirchengast, and J. Fuchsberger, "Generation of High-Resolution Wind Fields from the WegenerNet Dense Meteorological Station Network in Southeastern

Austria," *Wea. Forecasting*, vol. 32, no. 4, pp. 1301–1319, Apr. 2017, doi: 10.1175/WAF-D-16-0169.1.

[67]
L. C. Schroeder *et al.*, "The relationship between wind vector and normalized radar cross section used to derive SEASAT-A satellite scatterometer winds," *Journal of Geophysical Research: Oceans*, vol. 87, no. C5, pp. 3318–3336, 1982, doi: 10.1029/JC087iC05p03318.

[68]
G. Schumann, P. D. Bates, M. S. Horritt, P. Matgen, and F. Pappenberger, "Progress in integration of remote sensing–derived flood extent and stage data and hydraulic models," *Reviews of Geophysics*, vol. 47, no. 4, 2009, doi: 10.1029/2008RG000274.

[69]
N. Short, A.-M. LeBlanc, W. Sladen, G. Oldenborger, V. Mathon-Dufour, and B. Brisco, "RADARSAT-2 D-InSAR for ground displacement in permafrost terrain, validation from Iqaluit Airport, Baffin Island, Canada," *REMOTE SENSING OF ENVIRONMENT*, vol. 141. ELSEVIER SCIENCE INC, STE 800, 230 PARK AVE, NEW YORK, NY 10169 USA, pp. 40–51, Feb. 05, 2014. doi: 10.1016/j.rse.2013.10.016.

[70]
L. C. Smith, "Satellite remote sensing of river inundation area, stage, and discharge: a review," *Hydrological Processes*, vol. 11, no. 10, pp. 1427–1439, 1997, doi: 10.1002/(SICI)1099-1085(199708)11:10<1427::AID-HYP473>3.0.CO;2-S.

[71]
L. Smith, J. Fayne, and E. Kzivat, "Preliminary Ka-band returns from 2017 NASA ABoVE AirSWOT Flight Campaigns," 2018. [Online]. Available: https://spark.adobe.com/page/QSAh6yJWRaL1S

[72]
L. Smith, H. Yesou, C. Huber, and H. Giraud, "Expected Capability on Phenomenology Issues," presented at the SWOT Science Team Meeting : Splinter meeting in hydrology, Jan. 2014. Accessed: Jun. 25, 2021. [Online]. Available: https://swot.jpl.nasa.gov/system/documents/files/3375_3375_jan14_sdt3_25_hydro.pdf

[73]
S. Tuozzolo *et al.*, "Estimating River Discharge With Swath Altimetry: A Proof of Concept Using AirSWOT Observations," *Geophysical Research Letters*, vol. 46, no. 3, pp. 1459–1466, 2019, doi: 10.1029/2018GL080771.

[74]

F. T. Ulaby and W. Herschel Stiles, “Microwave response of snow,” *Advances in Space Research*, vol. 1, no. 10, pp. 131–149, Jan. 1981, doi: 10.1016/0273-1177(81)90389-6.

[75]
J. J. van Zyl, “Unsupervised classification of scattering behavior using radar polarimetry data,” *IEEE Transactions on Geoscience and Remote Sensing*, vol. 27, no. 1, pp. 36–45, Jan. 1989, doi: 10.1109/36.20273.

[76]
T. VANHYLCK, “WATER LEVEL FLUCTUATION IN EVAPOTRANSPIROMETERS,” *WATER RESOURCES RESEARCH*, vol. 4, no. 4. AMER GEOPHYSICAL UNION, 2000 FLORIDA AVE NW, WASHINGTON, DC 20009, pp. 761-, 1968. doi: 10.1029/WR004i004p00761.

[77]
W. P. Waite and H. C. MacDonald, “‘Vegetation Penetration’ with K-Band Imaging Radars,” *IEEE Transactions on Geoscience Electronics*, vol. 9, no. 3, pp. 147–155, Jul. 1971, doi: 10.1109/TGE.1971.271487.

[78]
Wan, Zhengming, Hook, Simon, and Hulley, Glynn, “MOD11A1 MODIS/Terra Land Surface Temperature/Emissivity Daily L3 Global 1km SIN Grid V006.” NASA EOSDIS Land Processes DAAC, 2015. doi: 10.5067/MODIS/MOD11A1.006.

[79]
J. A. WANG, D. SULLA-MENASHE, C. E. WOODCOCK, O. SONNENTAG, R. F. KEELING, and M. A. FRIEDL, “ABoVE: Landsat-derived Annual Dominant Land Cover Across ABoVE Core Domain, 1984-2014,” p. 15817.400714 MB, 2019, doi: 10.3334/ORNLDAAC/1691.

[80]
A. Wineteer *et al.*, “Measuring Winds and Currents with Ka-Band Doppler Scatterometry: An Airborne Implementation and Progress towards a Spaceborne Mission,” *Remote Sensing*, vol. 12, no. 6, Art. no. 6, Jan. 2020, doi: 10.3390/rs12061021.

[81]
T. Wu, B. Qin, A. Huang, Y. Sheng, S. Feng, and C. Casenave, “Reconsideration of wind stress, wind waves, and turbulence in simulating wind-driven currents of shallow lakes in the Wave and Current Coupled Model (WCCM) version 1.0,” *Geoscientific Model Development*, vol. 15, no. 2, pp. 745–769, Jan. 2022, doi: 10.5194/gmd-15-745-2022.

[82]

X. Wu, S. Hensley, E. Rodriguez, D. Moller, R. Muellerschoen, and T. Michel, “Near nadir Ka-band sar interferometry: SWOT airborne experiment,” in *2011 IEEE International Geoscience and Remote Sensing Symposium*, Jul. 2011, pp. 2681–2684. doi: 10.1109/IGARSS.2011.6049755.

[83]

K. Xiao *et al.*, “Evaporation from a temperate closed-basin lake and its impact on present, past, and future water level,” *JOURNAL OF HYDROLOGY*, vol. 561. ELSEVIER, RADARWEG 29, 1043 NX AMSTERDAM, NETHERLANDS, pp. 59–75, Jun. 2018. doi: 10.1016/j.jhydrol.2018.03.059.

[84]

D. Yamazaki *et al.*, “A high-accuracy map of global terrain elevations,” *Geophysical Research Letters*, vol. 44, no. 11, pp. 5844–5853, 2017, doi: 10.1002/2017GL072874.

[85]

C. Yu, Z. Li, N. T. Penna, and P. Crippa, “Generic Atmospheric Correction Model for Interferometric Synthetic Aperture Radar Observations,” *Journal of Geophysical Research: Solid Earth*, vol. 123, no. 10, pp. 9202–9222, 2018, doi: 10.1029/2017JB015305.

[86]

S. H. Yueh *et al.*, “L-Band Passive and Active Microwave Geophysical Model Functions of Ocean Surface Winds and Applications to Aquarius Retrieval,” *IEEE Transactions on Geoscience and Remote Sensing*, vol. 51, no. 9, pp. 4619–4632, Sep. 2013, doi: 10.1109/TGRS.2013.2266915.

[87]

H. A. Zebker and J. Villasenor, “Decorrelation in interferometric radar echoes,” *IEEE Transactions on Geoscience and Remote Sensing*, vol. 30, no. 5, pp. 950–959, Sep. 1992, doi: 10.1109/36.175330.

[88]

L. Zhang, J. Shi, Z. Zhang, and K. Zhao, “The estimation of dielectric constant of frozen soil-water mixture at microwave bands,” in *IGARSS 2003. 2003 IEEE International Geoscience and Remote Sensing Symposium. Proceedings (IEEE Cat. No.03CH37477)*, Jul. 2003, vol. 4, pp. 2903–2905 vol.4. doi: 10.1109/IGARSS.2003.1294626.

[89]

“AirSwot : A Calibration/Validation Platform For The SWOT Mission - [PPT Powerpoint],” *vdocuments.site*. https://vdocuments.site/airswot-a-calibrationvalidation-platform-for-the-swot-mission.html (accessed Aug. 21, 2020).

[90]

"AirSWOT | Mission," *NASA SWOT*. https://swot.jpl.nasa.gov/mission/airswot (accessed Nov. 04, 2020).

[91] "ERA5 hourly data on single levels from 1979 to present." https://cds.climate.copernicus.eu/cdsapp#!/dataset/reanalysis-era5-single-levels?tab=overview (accessed May 09, 2022).

[92] "Global land surface atmospheric variables from 1755 to 2020 from comprehensive in-situ observations." https://cds.climate.copernicus.eu/cdsapp#!/dataset/insitu-observations-surface-land?tab=overview (accessed May 09, 2022).

[93] "Historical Environmental Monitoring Data," *Wood Buffalo Environmental Association*. https://wbea.org/historical-monitoring-data/ (accessed May 09, 2022).